MEASURING GLOBAL SPIN ALIGNMENT OF VECTOR MESONS AT STAR

by

C.W. Robertson

A Dissertation

Submitted to the Faculty of Purdue University

In Partial Fulfillment of the Requirements for the degree of

Doctor of Philosophy

Department of Physics and Astronomy

West Lafayette, Indiana

May 2025

THE PURDUE UNIVERSITY GRADUATE SCHOOL
STATEMENT OF COMMITTEE APPROVAL

Dr. Fuqiang Wang, Chair

Department of Physics and Astronomy

Dr. Wei Xie

Department of Physics and Astronomy

Dr. Paul Duffel

Department of Physics and Astronomy

Dr. Luis Martin Kruczenski

Department of Physics and Astronomy

Approved by:

Dr. Gabor Csathy

ACKNOWLEDGMENTS

I would like to thank my mother and father who instilled in me a love of learning and supported me throughout this process.

I would also like to thank the thesis committee who helped me develop as a scientist at Purdue University. Prof. Fuqiang Wang was always positive and determined, and he helped me to continue on the project in the pursuit of science. Prof. Wei Xie organized our groups weekly meetings and gave useful guidance along the way. Prof. Martin Kruczenski and Prof. Paul Duffel taught interesting and inspiring courses in theoretical physics that were essential for my foundation as a researcher.

TABLE OF CONTENTS

LIST OF TABLES

LIST OF FIGURES

LIST OF SYMBOLS

$\sqrt{s_{NN}}$	kinemic energy per nucleon
ϕ	azimuthal angle of particles
η	pseudorapidity of particles
y	rapidity of particles
p_T	transverse momentum of particles
Ψ_{RP}	azimuthal direction of reaction plane
Ψ_n	n^{th}-order event plane, in this study Ψ_1 and Ψ_2 are used
θ^*	Polar angle of a daughter kaon in the $\phi-$meson rest frame
ϕ^*	Azimuthal angle of a daughter kaon in the $\phi-$meson rest frame
v_2	Elliptic azimuthal flow
a_2	Difference in reconstruction efficiency between $\phi-$meson decays parallel and perpendicular to $\phi-$meson momentum
ρ	$\phi-$meson spin density matrix
ρ_{00}	00^{th} element $\phi-$meson spin density matrix
$\Delta\rho\{\theta*\}$	ρ_{00} - $\frac{1}{3}$ using θ^*
$\Delta\rho\{\phi*\}$	ρ_{00} - $\frac{1}{3}$ using ϕ^*
$\langle\cos^2\theta^*\rangle$	Mean cosine θ^* squared
m_{inv}	invariant mass
$K^{\pm}$	Kaon with charge $\pm$ 1
A	Breit-Wigner Amplitude
Γ	Breit-Wigner width
m_0	Breit-Wigner mass parameter
$r(m)$	Signal to Background ratio as a function of mass

ABBREVIATIONS

dca	distance of closest approach
EP	event plane
gdca	distance of closest approach for global tracks
LHC	Large Hadron Collider
nHitsFit	the number of hits used to fit a track
nHitsMax	upper limit of nHitsFit
PID	Particle Identification
QA	Quality Assurance
QCD	Quantum Chromodynamics
QGP	quark gluon plasma
RP	reaction plane
RefMult	reference multiplicity
TOF	Time of Flight detector
TofMatch	reference number of particles with TPC and TOF matched
TPC	Time Projection Chamber
VPD	Vertex Position Detector

ABSTRACT

Non-central heavy-ion collisions are expected to produce a large orbital angular momentum (OAM). This OAM can polarize the deconfined quarks and gluons in the Quark-Gluon Plasma (QGP) created in these collisions, which would affect the spin states of hadrons produced from the QGP medium, such as the $\phi(1020)$ vector meson. The STAR experiment at the Relativistic Heavy Ion Collider (RHIC) reported in *Nature 614 (2023) 244* a significant global spin alignment of ϕ mesons in Au+Au collisions from the Beam Energy Scan I (BES I) program, with significant beam energy dependence. The data cannot be explained by conventional physics mechanisms and requires a new phenomenological mechanism that couples the ϕ meson to fluctuating color fields of strangeness and antistrangeness ($s\bar{s}$) quarks.

Global spin alignment is quantified by the 00^{th} coefficient of the spin density matrix, ρ_{00}. It is typically measured, as is in the STAR publication, by the reconstructed ϕ meson yield as a function of the polar angle (θ^*) between a daughter kaon in the parent's rest frame and the OAM direction in the lab frame. The ϕ meson yield is reconstructed by opposite-sign kaon pair invariant mass (m_{inv}) after subtracting the combinatorial kaon pair background and correcting for detector acceptance and efficiency.

We present an alternative approach to extract ρ_{00} by utilizing the $\langle\cos^2\theta^*\rangle$ as a function of m_{inv} instead of analyzing the ϕ meson yields in $\cos\theta^*$ bins. This method only uses the overall signal to background ratio of the ϕ-meson and may be more robust against the few-percent variations in the yield vs. $\cos\theta^*$ that the reported ϕ-meson spin alignment signals indicate. We also present an alternative, data-driven approach to detector acceptance and efficiency corrections. This approach generates ϕ mesons using published kinematic spectra, decays them into kaons, and estimates the "true" $\langle\cos^2\theta^*\rangle$ vs. m_{inv} of the combinatorial background without detector effects. We then statistically identify the ϕ-decay kaons in data, scale all measured kaons to the decay kaon kinematics to get the background $\langle\cos^2\theta^*\rangle$ vs. m_{inv} in data. Since the later is affected by all detector effects, the difference of the two in the ϕ mass region is the overall correction for these detector effects, assuming the detector effect on the real ϕ-meson is the same as the detector effect seen by these "combinatorial"

or "pseudo" ϕ-meson. This thesis reports the findings from this new approach and a brief MC Closure test of this method.

This work identified an error in the published STAR data in *Nature 614 (2023) 244*. The STAR Collaboration is preparing an erratum for the *Nature* publication. The results in this thesis also indicate that the ϕ-meson spin alignment may not be strongly energy dependent. This could have profound physics implications, raising questions regarding its possible underlying mechanisms.

1. INTRODUCTION

1.1 The Standard Model

The standard model is the framework for explaining particle physics data, and much of our universe. The theory consists of a Lagrangian including the electromagnetic, weak, and strong interactions and their associated matter particles.

The particles in the standard model are listed in Fig. 1.1, excluding anti-particles. The matter particles (fermions) are the fundamental bound states of the theory while the gauge and scalar bosons describe interactions between the fermions. Each gauge boson refers to its own gauge group and gauge symmetry, for example the photon in Quantum Electrodynamics (QED) refers to the gauge group U(1), where U(N) is the Unitary group in dimension N. QED, without the weak interaction, is the prototypical theory to understand all other interactions because it is conceptually the closest to the classical theory of electromagnetism, and one of the most successful.

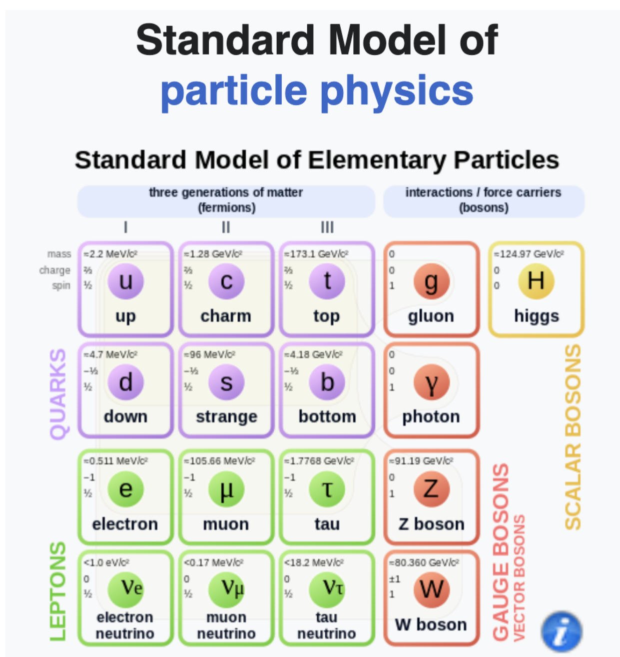

Figure 1.1. Wikipedia table of standard model particles [1]. Quarks and gluons make up the description of the strong interaction. Leptons and the other gauge bosons are the elements of electroweak theory. The Higgs boson gives the W and Z bosons mass through the Higgs Mechanism.

Including the weak interaction, QED describes leptons (e, μ, τ), their associated neutrinos (ν_e, ν_μ, ν_τ) interacting through the exchange of gauge bosons (γ, Z, W). Curiously, the W and Z bosons have a mass, and this is due to the Higgs Boson, H, or Higgs Mechanism, which has been experimentally detected at the LHC [2, 3]. The gauge group for the electroweak theory is SU(2) (Special Unitary Group of dimension 2), and the group is non-Abelian, contrary to pure QED which has gauge group U(1) (Unitary Group of dimension 1) and is Abelian.

Quantum Chromodynamcis (QCD) describes the strong interaction with gauge bosons, gluons (g) and fundamental fermions, the quarks, (u, d, c, s, t, b, making 6 flavors). The gluon is massless in QCD with gauge group SU(3) which is non-Abelian. In QCD, protons and neutrons are made of u and d quarks, c, t, and b quarks are called heavy flavours, and s is the strangeness quark.

1.2 Quantum Chromodynamics (QCD)

Nuclear physics is the study of the strong interaction, described by QCD, which binds quarks and gluons inside protons and neutrons. This feature is called "confinement" and means that at low energy or low momentum the quarks and gluons are confined into hadrons. At low energy the coupling between quarks and gluons becomes nearly infinite, and they behave as "solid" protons and neutrons [4, 5]. Related to this, the strong interaction is non-perturbative, and has no dimensionless parameter with which to expand in powers of, like the fine structure constant, α in QED.

Quantum Chromodynamics gets its name from "color." Since the gauge group is SU(3), each matrix in the group is a unitary 3×3 matrix with $Det = 1$ (or equivalently traceless, Hermitian). Each of these dimensions represents one "color," red, blue, or green. The idea being that a bound state is "colorless" and is either made up of red, green, and blue (baryon) or a color and its anti-color partner (meson), or any combination (exotic hadron). There are 8 traceless 3×3 Hermitian matrices in the group SU(3), called the Gell-Mann matrices, which represent the 8 gluon colors. Unlike QED, the gluon also carries the charge of the theory, color.

1.3 Heavy Ion Collisions and Vector Meson Spin Alignment

Relativistic heavy ion collisions create a hot and dense medium where quarks and gluons are deconfined over an extended volume comparable to the size of heavy nuclei [6, 7, 8]. Such a state of matter, called quark-gluon plasma (QGP), is believed to permeate the early universe after the Big Bang for a period of 10 μsec, at which the primordial matter hadronized into particles like protons and neutrons we know today. Studies of the QGP created in heavy ion collisions promise to reveal fundamental properties of quantum chromodynamics, the theory known to govern the interactions of quarks and gluons.

In non-central heavy ion collisions, a large orbital angular momentum (OAM) is present [9, 10]. The vorticity field generated by the large OAM in the created quark-gluon plasma (QGP) can polarize the spin-1/2 quarks [9, 11, 12, 13]. These polarization are inherited by final-state hadrons via hadronization, the effect of which can be measured by parity-violating weak decays of hyperons and by parity-conserving strong decays of vector mesons [9]. A finite global spin polarization of the Λ-hyperon has been indeed observed, on the order of 1%, suggesting the presence of an ultra-strong vortical field in the QGP [14]. A finite global spin alignment of the ϕ-meson has also been recently reported by the STAR experiment [15], as seen in Fig. 1.2. Spin alignment of vector mesons are a result of spin-spin correlations, which could be naively estimated to be on the order of the square of spin polarization. The reported ϕ-meson spin alignment is, however, also on the order of 1%, much larger than the expected value of 10^{-4} from the square of the Λ-hyperon spin polarization. This prompted the suggestion of strong color field fluctuations as a plausible novel physics mechanism for the large spin alignment [13, 16]. Incidentally, a negative ϕ-meson spin alignment is measured by the ALICE experiment [17], albeit at a much higher beam energy and at a slightly lower transverse momentum than measured by STAR.

An example cartoon of ϕ-meson spin alignment in heavy ion collisions is shown in Fig.1.3. The global spin alignment is measured by the angular distribution of a daughter kaon from the $\phi \to K^+K^-$ decay [15],

$$\frac{dN}{d\cos\theta^*} \propto (1-\rho_{00}) + (3\rho_{00}-1)\cos^2\theta^* \,, \tag{1.1}$$

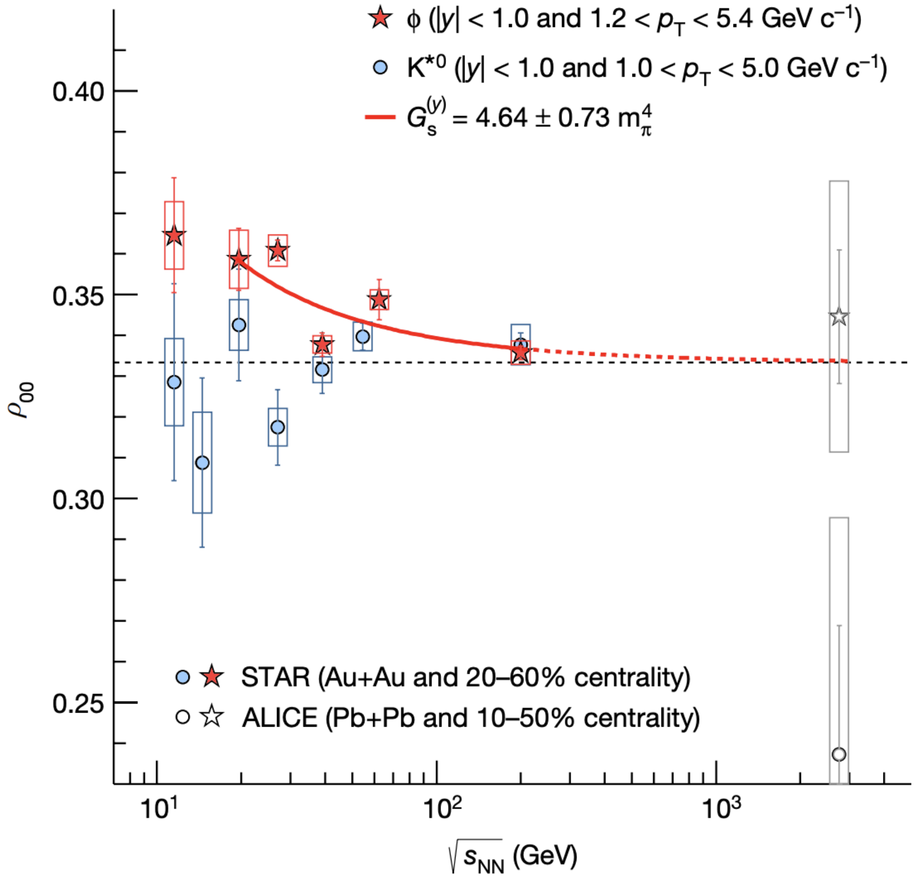

Figure 1.2. STAR BES-I ϕ-meson spin alignment measurement from Ref. [15] showing significant global spin alignment of ϕ-meson vs. beam energy in red. The beam energy dependence is significant, and the data is fit by the red curve. The physical motivation of the curve is a new mechanism related to the strange color field fluctuations. Measurement at 200 GeV is essentially zero, and a χ^2 analysis of the fit gives a p-value of $\sim$ 1% taking the total uncertainty of a data point as the quadrature sum of statistical and systematic uncertainties.

where θ^* is the polar angle of the kaon's momentum vector in the ϕ-meson rest frame with respect to the global OAM in the lab frame. The parameter ρ_{00} is the 00$^{\text{th}}$ coefficient of the spin density matrix. A uniform angular distribution gives $\rho_{00} = 1/3$. Deviation of ρ_{00} from 1/3 indicates a finite spin alignment.

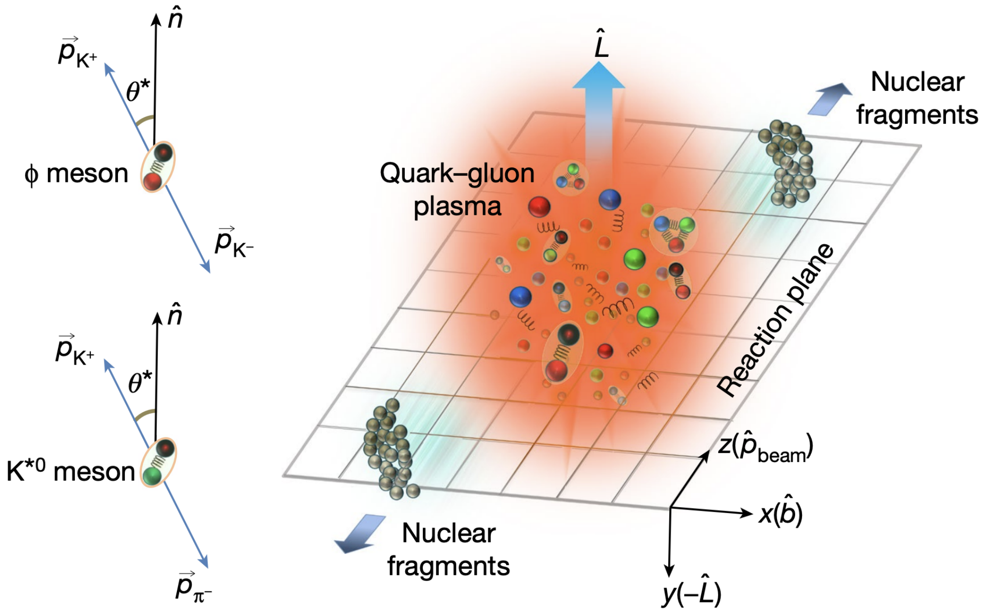

Figure 1.3. Schematic cartoon of spin alignment in heavy-ion collisions for ϕ-meson and K^{*0} showing θ^*, angle between the daughter momentum p_k and the OAM ($\hat{n}$), in the vector meson rest frame. From Ref. [15].

1.4 Scope of This Thesis

Conventionally, ϕ-meson yield is measured in bins of $\cos\theta^*$, corrected by ϕ-meson reconstruction efficiency and detector acceptance. These detector effects can be obtained from a *Monte Carlo* (MC) technique referred to as "embedding", where generated ϕ-mesons are "embedded" into real data. The detector response is simulated and applied to the ϕ-meson decay kaons, then some of the decay kaons that are reconstructed by data reduction software. Correction for detector effects are applied correspondingly in $\cos\theta^*$ bins.

Equivalently, the analysis can also be carried out by calculating the average $\langle\cos^2\theta^*\rangle$ as a function of the invariant mass ($m_{\rm inv}$) of K^+K^- pairs, corrected by the ϕ-meson efficiency and acceptance, to be converted into ρ_{00} via Eq. 1.1. This is called the invariant mass method. These two methods would give identical ρ_{00} results if everything was perfect and are good cross-checks in reality because of different systematic uncertainties involved. In this analysis, we use the invariant mass method.

The embedding technique is ideally expected to model the single- and two-particle effects of the detector by simulating detector hit and hit-merging information from MC tracks. In reality there is some uncertainty in how well the embedding simulation can capture all the subtle detector effects, particularly regarding two-particle effects. It would be desirable to have a data-driven way to correct for detector effects, which has in principle all the single- and multi-particle detector effects built in by real data. This analysis describes a general data-driven method to obtain detector corrections and discusses its advantages as well as assumptions.

2. EXPERIMENTAL APPARATUS

2.1 Relativistic Heavy Ion Collider (RHIC)

The Relativistic Heavy Ion Collider (RHIC) at Brookhaven National Laboratory (BNL) uses two 2.5 mile circumference rings of superconducting magnetics to accelerate heavy ions such as Au, Ru, Zr, and O to nearly the speed of light and collide them. Heavy-ions are used because they contain many protons and neutrons so the energy density built up in their collisions and the probability to create a QGP are higher. Colliding a variety of ions also allows for measurements to be compared between different systems. Essentially, collisions using different ions ask questions like: is QGP formed in small-system collisions like p+p, d+Au, and O+O collisions, and if so, how does this QGP compare to that formed in Au+Au collisions? The mandatory particle physics photo of the collider in Fig. 2.1 shows an aerial view of RHIC, the ion sources, and boosters used to get particles ready for collisions.

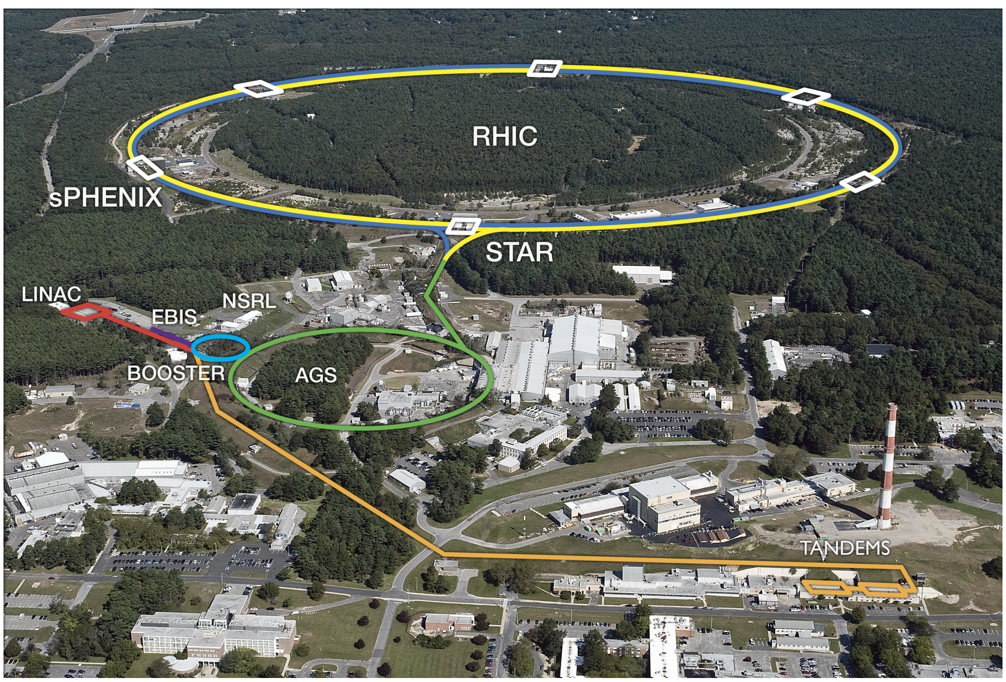

Figure 2.1. Aerial view of the Relativistic Heavy Ion Collider (RHIC) at Brookhaven National Lab [18]. STAR (Solenoidal Tracker at RHIC) is located at on intersection of the two blue and yellow rings. Other accelerators such as LINAC and AGS are used as part of the injection and acceleration pipeline into RHIC.

At one intersection of the two rings is the Solenoidal Tracker at RHIC (STAR) which consists of an array of detectors to observe and reconstruct particle collisions. Figure 2.2 shows an overview of the STAR detector and various sub detectors. The main detector at STAR is the Time Projection Chamber (TPC) which is used to reconstruct particle tracks (particle momenta) from heavy ion collisions.

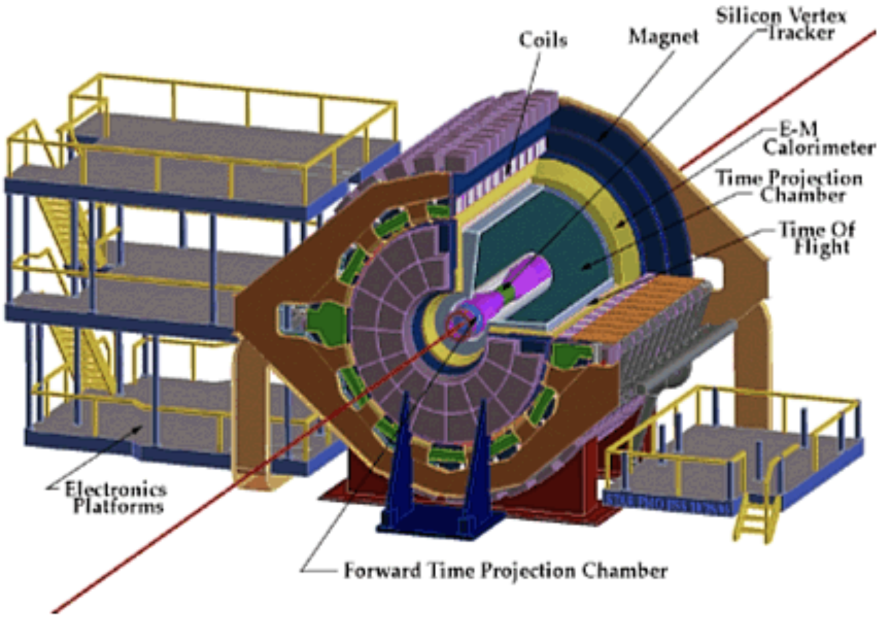

Figure 2.2. Overview of the STAR detector subsystems such as the Time Projection Chamber (TPC) and Time of Flight detector(TOF). TPC and TOF are the main detectors used in this analysis to reconstruct particle tracks from Au+Au Collisions. TPC is primarily used to reconstruct the momentum of each track, and TOF is used to identify the particle species of a track. In this analysis, we use TPC and TOF to identify charged kaons. Taken from the Brookhaven website. [19]

2.2 Time Projection Chamber (TPC)

The TPC is a solenoid and consists of a 0.5 T Magnetic field parallel to the beam direction which causes particles formed in the collision to follow curved trajectories [20]. The TPC is filled with gas such that particles ionize the gas and this emission is used to reconstruct particle tracks. The TPC is also used to measure the energy loss of charged particles as they pass through the medium vs track momentum. $\frac{dE}{d\hat{x}}$ vs p is used for particle identification as a given particle at a given momentum will have a characteristic energy loss $\frac{dE}{d\hat{x}}$ with some finite resolution.

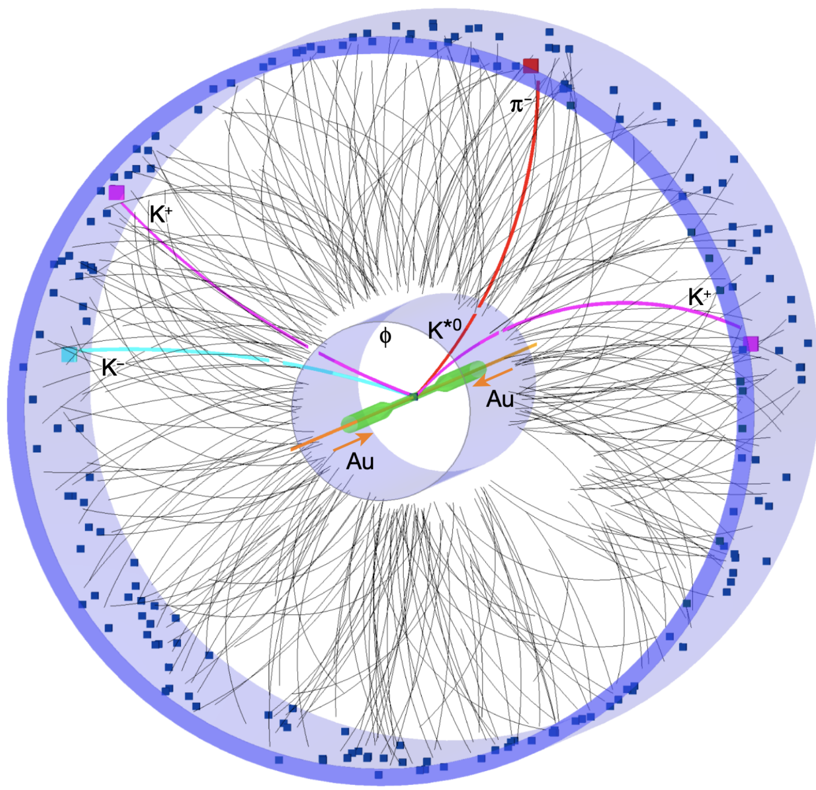

Figure 2.3. The region between the two blue cylinders is the TPC which measures ionization tracks and reconstructs particle kinematics. TOF is the outer most cylinder which is used for particle identification of each track. Green inner cylinder is the beam pipe. K^+K^- tracks from a ϕ meson decay are shown in purple in a Au+Au+ collision from [15]

2.3 Vertex Position Detector (VPD) and Time of Flight (TOF)

While TPC $\frac{dE}{d\hat{x}}$ can be used to identify charged kaons, we can get better particle identification using VPD and TOF. These two detectors are used together to determine the z-axis vertex position of the collision and the time of flight for each track, which can be used to measure the particle's mass.

A schematic of VPD is shown in Fig 2.4. The collision vertex position, along the z-axis, is reconstructed in heavy ion collisions by measuring Bremsstrahlung radiation from very forward (along the beam line) photons in the positive and negative z directions. For a given collision, the photons will arrive at each detector at slightly different times and this time difference can be used to determine the z-position of the primary vertex. The average of these two times is the event start time for Time of Flight (TOF). The stop time for TOF is the time at which the track hits the TOF cylinder outside the TPC as Illustrated in Fig. 2.4 [21].

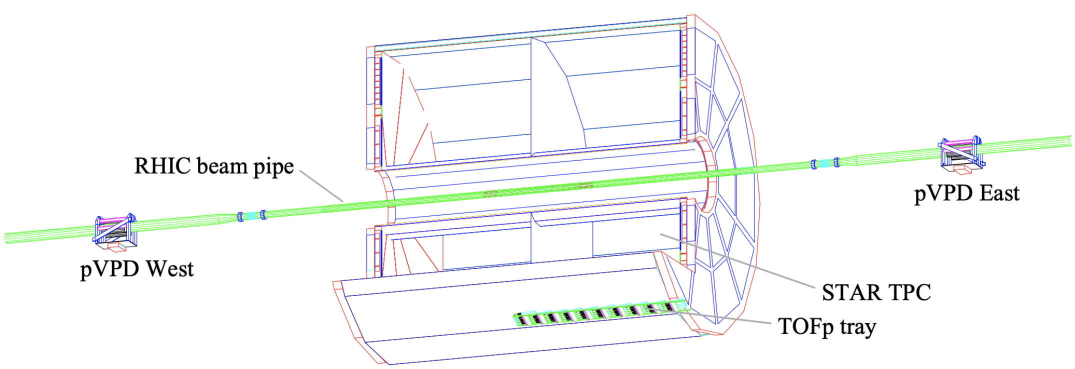

Figure 2.4. Schematic of VPD (also referred to as pVPD) and TOF. pVPD East and West determine the z position of the collsion and act as the start detector for TOF. TOF surrounds the TPC and acts as a stop detector to determine the time of flight and therefore the mass of charged particle tracks. Figure from [21].

3. DATA SET AND REDUCTION

3.1 Event Selection

For this study, we use Au+Au collision events at $\sqrt{s_{NN}}$ = 11.5–200 GeV with minimum bias (MB) triggers from Run 10, 11, 14, and 18. The approximate numbers of events and z-vertex cuts for each are listed in Table 3.1.

Table 3.1. Event statistics

Run	$\sqrt{s_{\mathrm{NN}}}$ (GeV)	Approx. number of events	$\lvert z_{\mathrm{vtx}}\rvert$ range (cm)
10	11.5	6.6e6	50
11	19.6	2.4e7	70
18	27	4.0e8	70
10	19	9.6e7	40
10	62.4	1.6e7	40
11	200	3.6e8	30
14	200	8.6e8	30

The primary vertex is reconstructed with TPC and we cut on $r_{\mathrm{vtx}} < 2$ cm for all beam energies. We also require $z_{\mathrm{vtx,diff}} = |z_{\mathrm{vtx,TPC}} - z_{\mathrm{vtx,VPD}}| < 6$ cm for all events. For particle identification (PID), we also cut on nToF matched points to be larger than > 3. These cuts are also listed in Table 3.2.

Table 3.2. Event-level cuts for all runs

$r_{\mathrm{vtx}} < 2$ cm
$z_{\mathrm{vtx,diff}} = \lvert z_{\mathrm{vtx,TPC}} - z_{\mathrm{vtx,VPD}}\rvert < 6$ cm
nToF matched > 3

3.2 Track Selection

Track cuts for all charged particles are listed in Table 3.3.

For K^+ and K^- particle identification (PID), we use both ToF and TPC, and we always require a track to pass cuts for both ToF and TPC. These cuts are listed in Table 3.4.

Table 3.3. Track Cuts

nHitsFit > 15
nHitsRatio > 0.51
$\|\eta\| < 1$
dca < 2 (cm)
$0.1 < p_\perp < 10$ (GeV/c)

Table 3.4. Kaon particle identification (PID) cuts

$0.16 < m^2_{\mathrm{TOF}} < 0.36$
$\|n\sigma_k\| < 2.5$

Additionally, the cuts for charged tracks used to reconstruct the event plane (EP) are listed in Table 3.5. We exclude all identified kaons from the EP reconstruction.

Table 3.5. Track cuts for EP reconstruction

nHitsFit > 15
nHitsRatio > 0.51
dca < 3 (cm)
$\|\eta\| < 1$ Full event EP, $-1 < \eta < -0.05$ East EP, $0.05 < \eta < 1$ West EP
$0.15 < p_\perp < 2$ (GeV/c)
$p < 10$ (GeV/c)

3.3 Event Plane Reconstruction

The event plane of any order ψ_n is defined in Eq. 3.1 in terms of a "flow vector" $\overrightarrow{Q_n}$, whose x and y components are written out as

$$(Q_{x,n}, Q_{y,n}) = \sum_{\mathrm{i}} (w_{\mathrm{i}} \cos n\phi_{\mathrm{i}}, w_{\mathrm{i}} \sin n\phi_{\mathrm{i}}) \,. \tag{3.1}$$

The sum in Eq. 3.1 is over all particles used for EP reconstruction with some track weight w_{i}. In this analysis, we use the conventional weight $w_{\mathrm{i}} = p_\perp$. The EP for each order n is calculated by Eq. 3.2,

$$\psi_n = \frac{1}{n}\left[\tan^{-1}\left(\frac{Q_{y,n}}{Q_{x,n}}\right)\right] \,. \tag{3.2}$$

In this analysis, we use ψ_2. In order to mitigate short-range correlations, we use two subevents East and West, with a η gap of 0.1; $\psi_{2,\mathrm{East}}$ is calculated using tracks from $-1 < \eta < -0.05$, and $\psi_{2,\mathrm{West}}$ from $0.05 < \eta < 1$.

The reconstructed EP angle is often nonuniform due to the detector effects. The angle of the EP is flattened by the conventional recentering and shifting procedure [22]. Here I will remove the East/West subscript because the procedures are the same for the two subevent EP's.

Recentering is a track-level correction that recenters the event average to $(Q_{x,n}, Q_{y,n}) = (0,0)$ by accumulating the event and track average of all $q_{n,\mathrm{i}}$'s, where $q_{n,\mathrm{i}} = (w_\mathrm{i} \cos n\phi_\mathrm{i}, w_\mathrm{i} \sin n\phi_\mathrm{i})$ is one particle's contribution to $\overrightarrow{Q}_n$. The event and track average of all $q_{n,\mathrm{i}}$'s is denoted by $\langle q_n \rangle$, no particle subscript. These $\langle q_n \rangle$'s are accumulated for each centrality. In each event, the recentered flow vector is given by

$$\overrightarrow{Q}_{n,rc} = \sum_{\mathrm{i}} (q_{n,\mathrm{i}} - \langle q_n \rangle) \,, \tag{3.3}$$

and the recentered event plane is calculated by

$$\psi_{n,rc} = \frac{1}{n} \left[\tan^{-1} \left(\frac{Q_{y,n,rc}}{Q_{x,n,rc}} \right) \right] \,. \tag{3.4}$$

After recentering, the event plane is "flattened" or "shifted", and this can be done in iterations for each event by calculating a $\psi_{n,\mathrm{shft}}$ from Eq. 3.5. The number of iterations we used is 20; i.e. $\mathrm{i}_{max} = 20$ in Eq. 5. The final, flat event plane is $\psi_{n,\mathrm{corr}} = \psi_{n,\mathrm{rc}} + \psi_{n,\mathrm{shft}}$.

$$n\psi_{n,\mathrm{shft}} = \sum_{\mathrm{i}}^{\mathrm{i}_{max}} \frac{2}{\mathrm{i}} \left(-\langle \sin \mathrm{i} n\psi_n \rangle \cos \mathrm{i} n\psi_n + \sin \mathrm{i} n\psi_n \langle \cos \mathrm{i} n\psi_n \rangle \right) \,. \tag{3.5}$$

4. DATA ANALYSIS

4.1 Analysis Methods

4.1.1 The Conventional Yield Method

The ϕ-meson ρ_{00} can be extracted from Eq. 1.1 by analyzing the ϕ-meson yield vs. $|\cos\theta^*|$, as was done by STAR [15] and ALICE [17]. The basic procedure is to fill the invariant mass ($m_{\rm inv}$) histograms of same-event opposite-sign (OS) kaon pairs (K^+K^-) that pass the PID cuts. The mixed-event K^+K^- pair $m_{\rm inv}$ histograms are also filled for background subtraction. These histograms are filled for each centrality bin, a few pair transverse momentum ($p_{\perp,\rm pair}$) bins to cover the range $1.2 < p_{\perp,\rm pair} < 5.4$ GeV/c, and 7 bins in $|\cos\theta^*|$ of equal width within $0 < |\cos\theta^*| < 1$. Here again, $\cos\theta^*$ is the dot-product of the momentum of a daughter kaon, in the parent rest frame, with $\hat{n} = \left(\cos(\psi_2 - \frac{\pi}{2}), \sin(\psi_2 - \frac{\pi}{2}), 0\right)$ where the ψ_2 is that of the opposite sub-event of the kaon pair pseudorapidity $\eta_{\rm pair}$. For example, if $\eta_{\rm pair} < 0$, then we use the west ψ_2 and vice versa. Additionally, only kaon pairs with rapidity $|y_{\rm pair}| < 1$ are used in the analysis. The rapidity is calculated by $y_{\rm pair} = \frac{1}{2}\ln\frac{E+P_z}{E-P_z}$ using the kaon pair 4-vector.

To extract the ϕ-meson yield, in a particular $|\cos\theta^*|$ bin, the mixed-event pair $m_{\rm inv}$ histogram is normalized to the real-event histogram at some low or high $m_{\rm inv}$ range (example: $m_{\rm inv} = [0.99, 1.0]$ GeV/c^2 or [1.04,1.05] GeV/c^2 or the sum), and then subtracted from the real-event histogram. At this point, the ϕ-meson yield can be extracted by fitting with a signal function and residual background. For this analysis, the signal function used is Breit-Wigner,

$$f_{\text{Breit-Wigner}}(m_{\rm inv}) = \frac{A\Gamma}{(m_{\rm inv} - m_0)^2 + (\frac{\Gamma}{2})^2}\,, \tag{4.1}$$

where m_0, A, and Γ are free parameters. A is the area or "yield parameter" (i.e., $A = \int f_{\text{Breit-Wigner}} dm_{\rm inv}$), and Γ is the peak width and may also be referred to as τ. After mixed-event subtraction, we can fit the remaining with $f_{\text{Breit-Wigner}}$ plus a residual background ($f_{\rm bkg}$, often taken as a polynomial function of certain order). We use the first-order polynomial for $f_{\rm bkg}$ (other functional forms can be used for systematic uncertainty assessment). We can subtract this residual background and refit with pure signal of $f_{\text{Breit-Wigner}}$. Sometimes, this is done to compare with other groups. However, there is essentially no difference in the signal parameters obtained from fitting $f_{\text{Breit-Wigner}} + f_{\text{bkg}}$ and from fitting with pure $f_{\text{Breit-Wigner}}$ after subtraction of the fitted f_{bkg}.

To extract ρ_{00} via the yield method, we get the yield parameters, A's, in 7 equal-width $|\cos\theta^*|$ bins in a desired centrality and $p_\perp$ range. We then fit these yields with Eq. 1.1; the center of each $|\cos\theta^*|$ bin is used as the $|\cos\theta^*|$ value in fit. We are not concerned with the overall scale of the yields; only the variation across the $|\cos\theta^*|$ bins affects ρ_{00}.

The yield method is a conventional method to extract ρ_{00} from the ϕ-meson data [17, 15]. There are reasons to have other methods to extract ρ_{00}: the finite $|\cos\theta^*|$ bin width can cause some systematics, and the fit using Eq. 1.1 is sensitive to the systematics of the yields in individual $|\cos\theta^*|$ bins. There can be considerable systematics from the yield extraction and background subtraction. An example of ρ_{00} extracted from the yield method in Au+Au collisions at $\sqrt{s_{\text{NN}}} = 200$ GeV from Run 14, with some evaluations of systematic uncertainties, is shown in Fig. 4.1. Note, only a subset of systematic uncertainty sources are plotted; other sources, e.g., residual background functions, are not included.

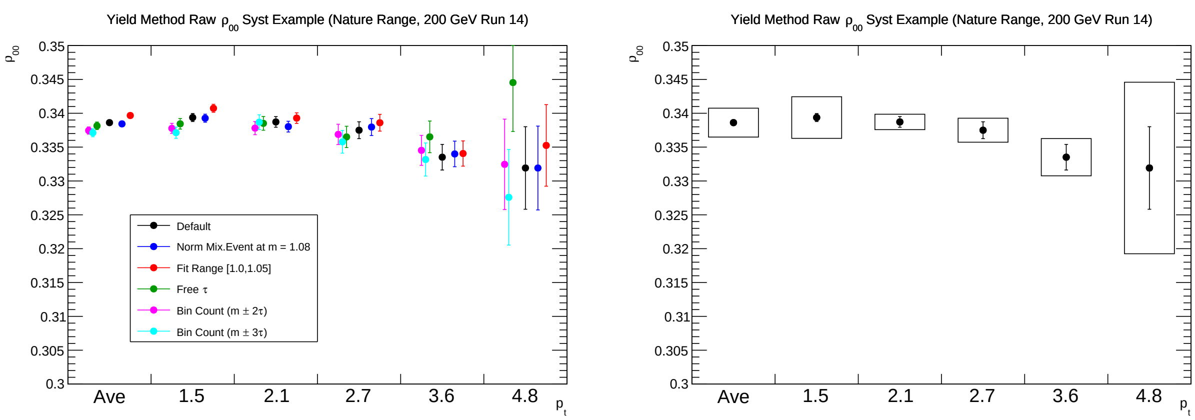

Figure 4.1. Example systematics for yield method ρ_{00} extraction in 20-60% centrality Au+Au collisions at $\sqrt{s_{\text{NN}}} = 200$ GeV from Run 14. The left panel shows evaluations of some systematic uncertainty sources by the Barlow procedure, and the right panel shows the extracted ρ_{00} with the evaluated systematic uncertainties. This is our data presented by Xin Dong (Chair of the Spin Alignment Task Force) at the Oct. 2024 STAR Collaboration Meeting for comparison with other groups.

4.1.2 The $\Delta\rho\{\theta^*\}$ Invariant Mass Method

Alternatively, we can profile the $\langle\cos^2\theta^*\rangle$ vs. kaon pair $m_{\rm inv}$ for real-event OS K^+K^- pairs–this is the "invariant mass method". This method removes the coarse $\cos\theta^*$ binning from the yield method and does not rely on precise extraction of ϕ-meson yield in each $|\cos^2\theta^*|$ bin. The invariant mass method is not new; it has been used previously in, e.g., anisotropic flow analysis of resonances [23]. We are simply applying the same idea to analyze vector meson spin alignment.

The invariant mass method procedure follows. To extract ρ_{00} or equivalently $\Delta\rho\{\theta^*\} \equiv \rho_{00}-1/3$, we fit the real-event OS pair mass histogram (inclusive over $\cos\theta^*$) with Breit-Wigner + Poly to obtain the signal to background ratio, $r(m_{\rm inv}) = N_{\rm sig}/N_{\rm bkg}$. An example fit is shown in the left panel of Fig. 4.2. As default, we use a second-order polynomial for the background and fit to the range of $m_{\rm inv} = [1.0, 1.04]$ GeV/c^2. For assessment of systematic uncertainty, we include two fit range variations, $[1.0, 1.05]$ and $[1.0, 1.06]$ GeV/c^2, and a third-order polynomial for the background function.

The profile of $\langle\cos^2\theta^*\rangle$ vs. $m_{\rm inv}$ can be readily converted into a profile of $\Delta\rho\{\theta^*\}$ vs. $m_{\rm inv}$ using Eq. 1.1 because

$$\Delta\rho\{\theta^*\} \equiv \rho_{00} - \frac{1}{3} = \frac{2}{5}\left(\left\langle\cos^2\theta^*\right\rangle - \frac{1}{3}\right) . \tag{4.2}$$

The $\Delta\rho\{\theta^*\}$ can then be extracted by fitting the profile of $\Delta\rho\{\theta^*\}(m_{\rm inv})$ vs. $m_{\rm inv}$ to

$$\Delta\rho\{\theta^*\}(m_{\rm inv}) = \frac{f^{\cos}_{\rm bkg}(m_{\rm inv}) + r(m_{\rm inv})\Delta\rho\{\theta^*\}}{1 + r(m_{\rm inv})} , \tag{4.3}$$

where $f^{\cos}_{\rm bkg}(m_{\rm inv})$ is the background shape of the $\Delta\rho\{\theta^*\}(m_{\rm inv})$ vs. $m_{\rm inv}$ and is unknown *a priori*. Note that the $\Delta\rho\{\theta^*\}$ in the numerator of the r.h.s. of Eq. 4.3 is simply a constant free parameter that we extract from the fit. For this analysis, we use a linear function,

$$f^{\cos}_{\rm bkg}(m_{\rm inv}) = p_1(m_{\rm inv}) + p_0 \tag{4.4}$$

Note the form of Eq. 4.3 is used to extract $\Delta\rho\{\theta^*\}$, $\Delta\rho\{\phi^*\}$, v_2, and a_2 by fitting the corresponding profile vs. m_{inv}; these will be discussed later in this thesis.

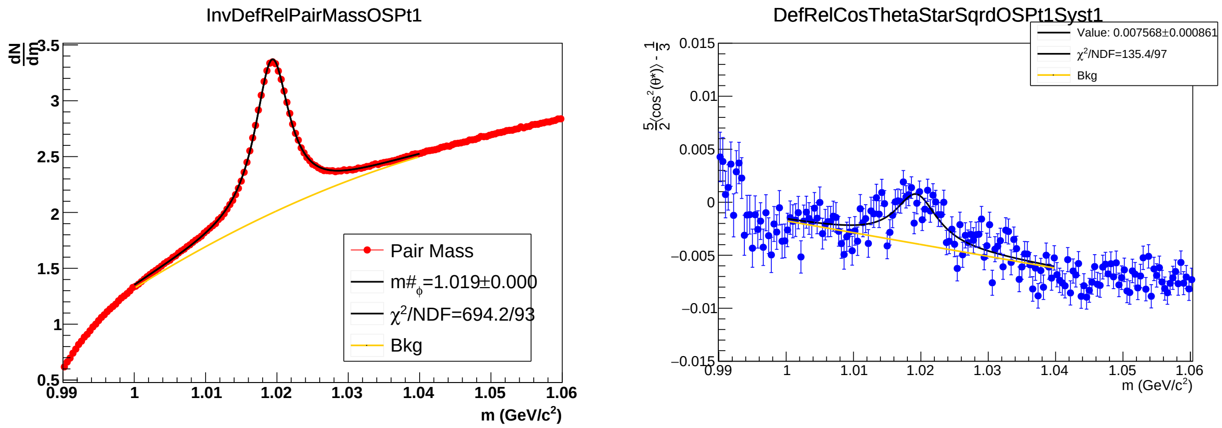

Figure 4.2. (Left) Same-event K^+K^- m_{inv} histogram within pair transverse momentum $1.2 < p_{\perp,\text{pair}} < 1.8$ GeV/c^2 and Breit-Wigner + Poly2 fit in 20-60% centrality Au+Au collisions at $\sqrt{s_{\text{NN}}} = 200$ GeV from Run 14. (Right) Corresponding $\langle\cos^2\theta^*\rangle$ vs. m_{inv} and fit by Eqs. 4.3 and 4.4. Here the y-axis has been converted to fit for $\Delta\rho\{\theta^*\}$ directly.

The invariant mass method and the yield method would yield the same ρ_{00} in a perfect world. In reality they differ because of different ways of dealing with backgrounds (effectively, different assumptions) and some other sources of systematics. For the invariant mass there is systematic uncertainty from the form of $f^{\cos}_{\text{bkg}}$, whereas those in the yield method come from the uncertainties in the background forms f_{bkg} of all individual $\cos\theta^*$ bins. The invariant mass method depends on the signal-to-noise ratio $r(m_{\text{inv}})$ which can be more robust than the yields in individual $\cos\theta^*$ bins. If the background f_{bkg} in each $\cos\theta^*$ is precisely known and the $f^{\cos}_{\text{bkg}}$ is precisely known, then both methods should give the same result.

4.1.3 The $\Delta\rho\{\phi^*\}$ Invariant Mass Method

Dr. Sergei Voloshin [24] proposed to use ϕ^*, the projection of θ^* onto the transverse plane, to measure ρ_{00} or equivalently,

$$\Delta\rho\{\phi^*\} \equiv \rho_{00} - \frac{1}{3} = -\frac{4}{3}\left\langle\cos 2(\phi^* - \psi_{RP})\right\rangle \,, \tag{4.5}$$

where ψ_{RP} is the reaction plane angle (in this analysis the opposite subevent ψ_2 is used). Although the EP resolution effect is stronger for ϕ^* than for θ^*, the detector effects may be simpler and easier to deal with in the $\Delta\rho\{\phi^*\}$ measurement.

The $\Delta\rho\{\phi^*\}$ method ideally gives the same final result as the $\Delta\rho\{\theta^*\}$ method; however, the ϕ^* method has a different kinematic dependence, since ϕ^* is an azimuthal angle and θ^* is a polar/3D angle. The detector and resolution correction methods for ϕ^* and θ^* are also different. For the ϕ^* analysis we use the invariant mass method similar to Eq. 4.3 but we profile $\langle\cos 2(\phi^* - \psi_{RP})\rangle$ instead; that is, replace $\langle\cos^2\theta^*\rangle \rightarrow \langle\cos 2(\phi^* - \psi_{RP})\rangle$. The $\langle\cos 2(\phi^* - \psi_{RP})\rangle$ vs. m_{inv} can then be converted to $\Delta\rho\{\phi^*\}$ vs. mass through Eq. 4.5, or equivalently the fit parameter can be converted. An example of signal extraction of the ϕ^* method is shown in Fig. 4.3.

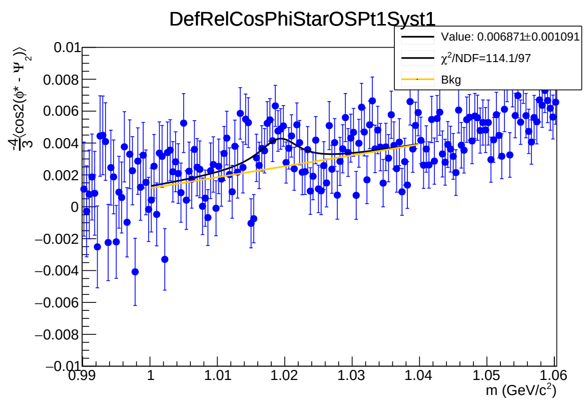

Figure 4.3. Example of $\Delta\rho\{\phi^*\}$ vs. kaon pair invariant mass within pair transverse momentum $1.2 < p_{\perp,\text{pair}} < 1.8$ GeV/c in 20-60% centrality Au+Au collisions at $\sqrt{s_{\text{NN}}} = 200$ GeV from Run 14. The signal to noise ratio is obtained from Fig. 4.2 left panel.

4.1.4 The $\Delta\rho\{\phi^*\}$ in "Helicity Frame"

The $\Delta\rho\{\phi^*\}$ observable can be readily modified into

$$\Delta\rho_p\{\phi^*\} = -\frac{4}{3}\langle\cos 2(\phi^* - \phi_p)\rangle \tag{4.6}$$

by replacing the EP angle in Eq. 4.5 by the azimuthal angle of ϕ-meson in the lab frame. We used the subscript 'p' to stand for the parent (ϕ-meson) transverse momentum direction. This would be the spin alignment with the quantization axis defined to be the vector meson transverse momentum direction. *Note, this is different from the 3D momentum direction as the quantization axis, which is often called helicity-frame spin alignment; however, we will hereinafter refer to it simply as "helicity-frame."* In other words, the helicity-frame spin alignment can also be measured by the polar angle θ^* with respect to the lab-frame ϕ-meson (transverse) momentum direction; however, we do not use it in this analysis.

We will write a subscript p (as in Eq. 4.6) to indicate it is the (transverse) helicity-frame spin alignment $\Delta\rho$. Likewise, $\Delta\rho_z$ would indicate local spin alignment with respect to the beam direction as the quantization axis. With this convention, $\Delta\rho_L$ would be the global spin alignment with respect to the total orbital angular momentum, but we will omit this subscript where it is clear from the context.

4.2 Corrections for Detector Effects

In heavy-ion collisions, individual ϕ-meson decays to K^+K^- pairs are not directly observed. The final-state particle tracks are reconstructed and "identified" as kaons with a good level of confidence. Invariant masses of those pairs of kaons identified by opposite sign are calculated and offer discrimination for ϕ mesons. A distinctive ϕ-meson peak is usually observable atop a background pedestal, which is composed of combinatorial kaon pairs and pairs with misidentified particles. Kaon pairs from ϕ-meson decays are thus statistically identified by fitting the kaon pair mass distribution by, for example, a Breit-Wigner or Gaussian function to extract the ϕ-meson yield.

Detector imperfections and finite acceptance (tracks with $|\eta| > 1$ are not "measured") will cause the detector to miss some true ϕ-meson decays. These effects can affect the ϕ-meson yield as functions of $|\cos\theta^*|$, although the effect on the yield itself is relatively small. The effects on $\Delta\rho$ are not trivial because the signal of $\Delta\rho$ is very small ($\sim 1\%$), i.e. a variation of only a few percent in the yield over the span of $|\cos\theta^*|$ from 0 to 1. We need to know the detection accuracy of the ϕ-meson decay kaon pairs to a sub-percent level over the angle span.

Typically, corrections for detector inefficiencies are made with the ϕ-meson $(p_\perp, \eta, \phi - \Psi_{EP})$ dependent efficiency from embedding in the yield method to extract the raw $\Delta\rho\{\theta^*\}$. Here ψ_{EP} is the reconstructed event plane and the efficiency can have some dependence on ψ_{EP} because of the varying occupancies. Often, only the $p_\perp$-dependent efficiency is used, assuming the η dependence is uniform and the $\phi - \Psi_{EP}$ dependence is usually small [15].

The procedure in the *Nature* publication [15] is somewhat different, where the product of single kaon efficiencies is applied instead of the ϕ-meson efficiency. The single kaon efficiencies may not account for two-particle effects of the detector, while the ϕ-meson efficiency does in principle. It was claimed that two-particle effects are small [15].

In the embedding efficiency calculation, the kaons are restricted within $|\eta| < 1$ and also some $p_\perp$ range. Decay kaons that are outside this range cannot be recovered by the efficiency correction. This acceptance effect is corrected in [15] by pure Pythia simulation, where the ϕ-meson $p_\perp$ distribution is weighted to match data measurement in heavy-ion collisions, by comparing the $\cos\theta^*$ distributions with and without the $|\eta| < 1$ cut on the decay kaons.

Embedding corrections have been used and successful in measurements on single-particle level, such as particle spectra and yields. Once the analysis cut distributions are checked out between embedding and data, the corrections extracted from embedding are fairly reliable. This is easy to do on single-particle level, however, it is not clear whether embedding can adequately describe two-particle level distributions. Particularly, in the case of spin alignment, $\Delta\rho\{\theta^*\}$, θ^* is a 3D or polar angle in the ϕ-meson rest frame, involving boost from the laboratory frame where the tracks are measured and characterized. The boost is in turn determined by the measured track parameters. The relationship between θ^* and the measured kaon track is very complicated and it is opaque how imperfections in tracking and acceptance propagate to the θ^* measurements. Since the $\Delta\rho\{\theta^*\}$ signal is very small, at most about 1%, it is unclear if the standard embedding can be trusted on that level for 3D kinematics.

4.2.1 Data-Driven Corrections for $\Delta\rho\{\theta^*\}$

Because of possible issues of embedding in describing two-particle detection accuracy, we want to use data-driven ways to correct the raw $\Delta\rho\{\theta^*\}$ measurements. Data-driven correction methods, if successful, are always better and thus preferred than any simulation methods because data effects are by definition included in real data.

The central question is: What are the detector effects on kaon pairs from the same ϕ-meson decays? Specifically, for our case, what is the change in $\Delta\rho\{\theta^*\}$ of the real ϕ-meson decay K^+K^- pair due to detector effects? Obviously, we cannot use those real decay kaon pairs because the real $\Delta\rho\{\theta^*\}$ is unknown–this is the exact physics signal we are trying to measure after those detector correction. We need to use kaon pairs that are not from real signal but otherwise equal to those real signal kaons. *The idea is to analyze the $\Delta\rho\{\theta^*\}$ of combinatorial pairs of kaons from ϕ-meson decays measured in our detector, and compare the result to that before the kaons suffer any detector effects.* The former can be obtained from real data, with one complication: the ϕ-meson identification is statistical because of combinatorial background, so we cannot uniquely say which kaon is from ϕ-meson decay and which is not. To circumvent this, we use all identified kaons and scale them to match the decay kaon kinematics in $(p_\perp, \eta, \phi)$ which is measured statistically. This procedure is referred to as *"data scaling"* and described in Section 4.2.1. The latter can be obtained by MC sampling using published ϕ-meson data, referred to as *"data folding"* and described in Section 4.2.1.

ϕ-Meson Decay Kaons In Data (Data Scaling)

To identify decay kaons in data we first go through all OS (opposite sign) kaon pairs in an event. We fill a kaon pair m_{inv} histogram for these real-event OS pairs and another m_{inv} histogram for "Rotated Pairs" where K^- is rotated by π in azimuth. Rotated pairs are used to estimate the background in the real-event OS pair histogram. For each real and rotated kaon pair, we fill *single* particle 3D histograms of $(p_\perp, \eta, \phi - \psi_2)$ for K^+ and K^-, separately. Additionally, we do the same for all single kaons, without forming pairs of K^+ and K^- (i.e., looping over all kaons in the single-particle loop, not within the pair double loop). The reason we want the single kaons is because we will want to weight all measured kaons to match the decay kaon kinematics since the decay kaons are not identified exclusively, but only statistically. This way we can use all measured kaons in data to mimic the ϕ-decay kaons in terms of the exact kinematic distributions. In total we obtain:

- 3-D $(p_{\perp}, \eta, \phi - \psi_2)$ histograms for K^+ and K^- from real-event OS pairs,
- 3-D $(p_{\perp}, \eta, \phi - \psi_2)$ histograms for K^+ and K^- from rotated OS pairs, and
- 3-D $(p_{\perp}, \eta, \phi - \psi_2)$ histograms for all single K^+ and K^-.

This is done for each centrality bin for a given $p_{\perp}$ range of interest, say $1.2 < p_{\perp,\text{pair}} < 5.4$

From this point, we would like to obtain the decay kaon kinematics and take $\frac{\text{decay kaon}}{\text{all kaon}}$ as weight, and then apply this weight to all kaons in data. Individual decay kaons are not identified in data, we can only statistically identify decay kaon pairs. We do not know if a specific kaon is a ϕ-decay daughter kaon or a primordial kaon. For illustration, we can think of the 1-D η distributions. The η projection of the real pair 3-D $(p_{\perp}, \eta, \phi - \psi_2)$ histogram minus the η projection of the rotated pair 3D histogram is approximately the decay kaon η distribution. The rotated pair histograms just have to be normalized from the comparison of the real pair mass histogram and the rotated pair mass histogram as seen in Fig. 4.4. We fit the real, OS pair histogram with Breit-Wigner + Poly3 on $[1.0, 1.04]$ GeV/c as a demonstration. The normalization is really done by bin counting (ROOT ``IntegralAndError'' function) of the real and rotated pair histograms in the range $[1.03, 1.04]$ GeV/c. Then, we take the ratio $\frac{\text{Real Entries}}{\text{Rot. Entries}}$ and scale the rotated pair histogram by this ratio.

We get this ratio in each centrality bin and each pair $p_{\perp,\text{pair}}$ bin and scale each of the 3-D rotated pair kaon kinematic histograms by their respective factor. The next step is to perform (Real − Normalized Rot.) for all the 3D histograms, to isolate the ϕ-meson decay kaon kinematics in data. See an example in Fig. 4.5. Other pair $p_{\perp,\text{pair}}$ bins and kinematic projections to other variables (η, ϕ) can be seen in the appendix, Figs. C.1–C.3 for 200 GeV Run 14 Au+Au data.

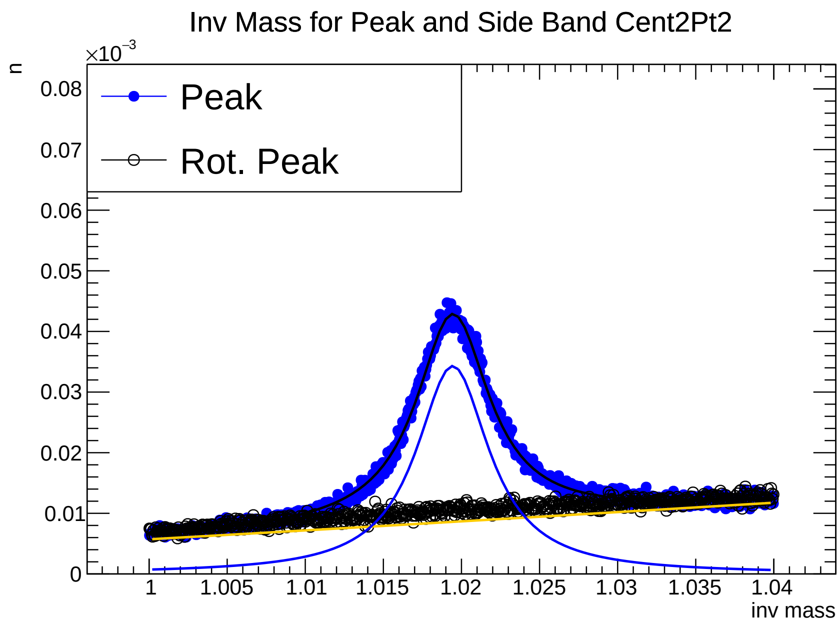

Figure 4.4. Example of Real OS kaon pair (blue) and Rotated OS kaon pair (black) m_{inv} distributions with pair transverse momentum $1.8 < p_{\perp,\text{pair}} < 2.4$ GeV/c in 60-70% centrality Au+Au collisions at $\sqrt{s_{\text{NN}}} = 200$ GeV from Run 14.

After proper normalization, we sum the real minus rotated pair 3-D histograms over pair $p_{\perp,\text{pair}}$ bins (normalization is done for each pair $p_{\perp,\text{pair}}$ bin) and divide it by the all kaon 3-D $(p_\perp, \eta, \phi - \psi_2)$ histogram; for K^+ and K^-, respectively. The result is a weight histogram for K^+ and K^- in each centrality bin that depends on the kaon's $(p_\perp, \eta, \phi - \psi_2)$. To apply this weight in data, we take each kaon, find its corresponding kinematic bin in the weight histogram, read the bin content, and assign the bin content as a weight. In this way, we are using real data kaons and mimicking them as ϕ decay kaons in terms of the full kinematics. Lastly, we loop all the measured K^+ and K^- in each event and fill the rotational and mixed event pair $\langle\cos^2(\theta^*)\rangle$ as a function of m_{inv} with these weights applied at the track level. Here, ψ_2 is determined by the subevent opposite to the pair η as done in real data analysis.

As a QA check, we fill a 3-D histogram of all single K^+ and K^- with these weights applied to see the effect of the kinematic weighting. Figure 4.6 shows the effect of the weights on the single-kaon $p_\perp$ histogram (all histograms are arbitrarily normalized to just compare the shapes).The black histograms are all kaons, and the blue histograms are after weighting.

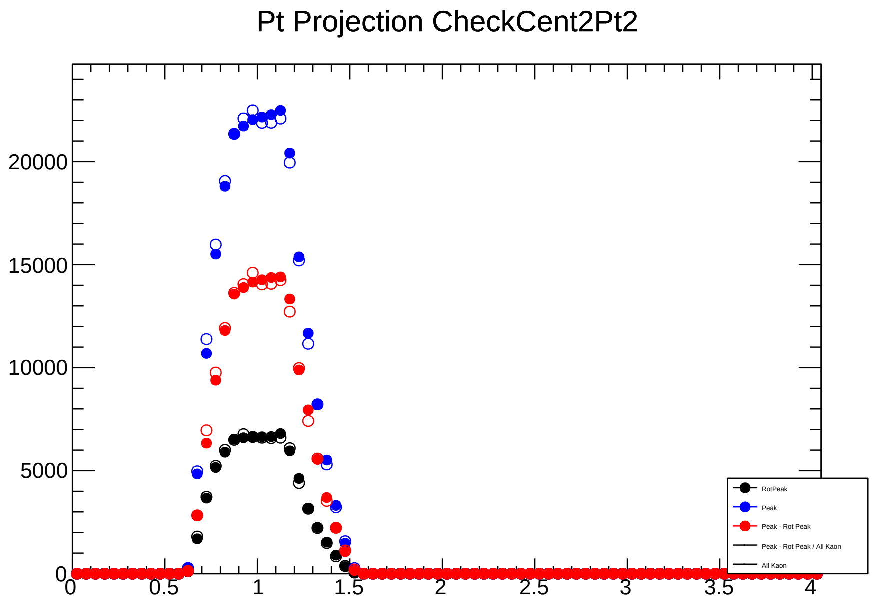

Figure 4.5. Example of $p_{\perp}$ projection of 3-D histograms for Peak (blue), Rot. Peak (black), and Peak − normalized Rot. Peak (red) for 60-70% centrality Au+Au collisions at $\sqrt{s_{\rm NN}} = 200$ GeV from Run 14. The "Peak" and "Rot. Peak" mean the $m_{\rm inv}$ range of [1.015,1.025]. The pair transverse momentum range is $1.8 < p_{\perp,\rm pair} < 2.4$ GeV/c. 1-D Examples of the kaon weight histograms can be seen in the Appendix Fig. C.4.

Figure 4.6 also shows other $p_{\perp}$ distributions. The green stars are the input ϕ-meson spectrum from published data, and the red stars are the reconstructed ϕ-meson spectrum from the raw ϕ-meson yield in a particular $p_{\perp}$ bin. The shape are in good agreement; the slightly harder spectrum for the red stars is presumably because of the $p_{\perp}$-dependent efficiency. The green circles are the spectrum of ϕ-decay kaons using published ϕ-meson data. It is slightly softer than the reconstructed ϕ-decay kaon spectrum (covered by the blue points). In light of the aforementioned $p_{\perp}$-dependent efficiency, the agreement is good. This means that our data reconstruction of the ϕ-decay kaons is doing a good job. The brown and gray circles show the intermediate $p_{\perp}$ spectra of measured kaons and rotated kaons from pairs falling within the ϕ-meson $m_{\rm inv}$ peak region of [1.015,1.025] GeV/c^2. They are softer than the inclusive kaons because of the $m_{\rm inv}$ requirement. The difference between these two spectra is the reconstructed ϕ-decay kaon spectrum hidden behind the blue circles. The fact that the reconstructed kaon spectrum is in reasoanble agreement with the published ϕ-decay kaon spectrum means that the rotated kaons pairs are correctly reflecting the combinatorial background underneath the ϕ-meson peak.

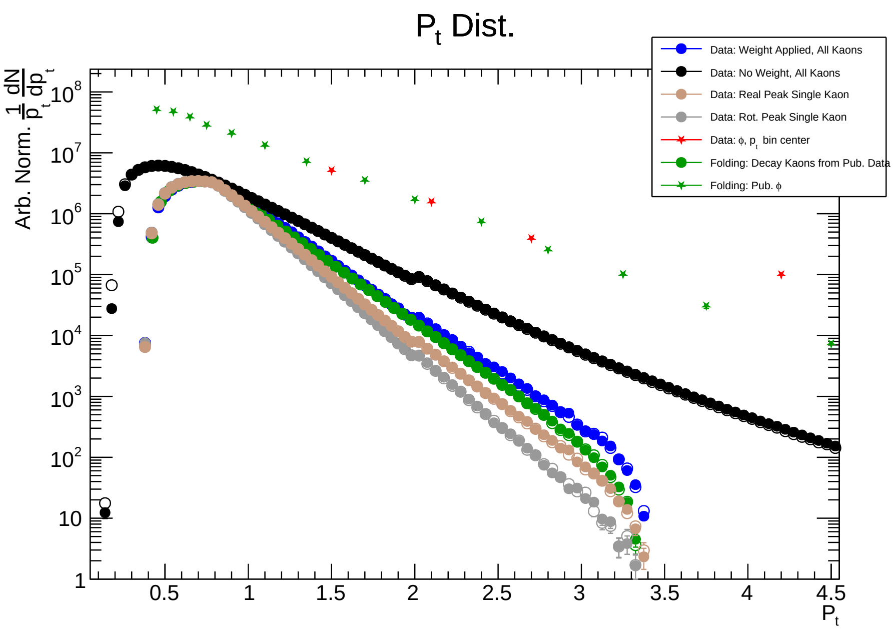

Figure 4.6. The various $p_\perp$ spectra (arbitrarily normalized to just compare the shapes) in 20-60% centrality Au+Au collisons at $\sqrt{s_{\mathrm{NN}}} = 200$ GeV from Run 11. Green stars are the published ϕ-meson $p_\perp$ averaged to 20-60% centrality. Red stars are the ϕ-meson yields in each $p_\perp$ bin, placed at the bin center $p_\perp$ (hence the disagreement at $p_\perp = 4.2$); then divided by $p_\perp$ (also the bin center) to be $\frac{1}{p_\perp}\frac{dN}{dp_\perp}$. Gray and orange/tan points are the $p_\perp$ spectra of the Rot. Peak (side band pairs) single kaons and Peak pairs single kaons, respectively. (Ignore bump at $p_\perp = 2$, due to changing bin width in Run 11.) The black histograms show all single K^+ (filled) and K^- (open). The weighted kaon distributions are in blue, which are, by definition, the decay kaon distributions reconstructed from real data. The distributions of decay kaons from simulation of published ϕ-meson data (see *"data folding"* in Section 4.2.1) are in green. The blue histogram is seen to agree with the green one well; the small difference between the two is presumably the effect of the $p_\perp$-dependent efficiency.

At this point, we have identified the decay kaon kinematics in data, scaled the measured single kaon kinematics to match the decay kaons, and formed rotated kaon pairs and mixed-event kaon pairs scaled to the decay kaon pairs. Figure 4.7 shows the $\Delta\rho\{\theta^*\}$ (obtained from $\langle\cos^2(\theta^*)\rangle$) as a function of m_{inv} for the rotated kaon pairs and the mixed-event kaon pairs in filled and open blue points, respectively. For reference, the calculated $\Delta\rho\{\theta^*\}$ from

K^--rotated and mixed-event pairs from measured kaons without applying any weights are shown in filled and open black points, respectively. Clearly, kaon kinematics affect the obtained $\Delta\rho\{\theta^*\}$, softer kaons–ϕ-meson decay kaons are softer than the primordial kaons (see Fig.4.6)–having smaller values of $\Delta\rho\{\theta^*\}$. The mixed-event kaon pair $\Delta\rho\{\theta^*\}$ is smaller than the rotated kaon pair $\Delta\rho\{\theta^*\}$. This is because $\Delta\rho\{\theta^*\}$ depends on the EP resolution; the mixed-event pairs can be considered to have zero EP resolution.

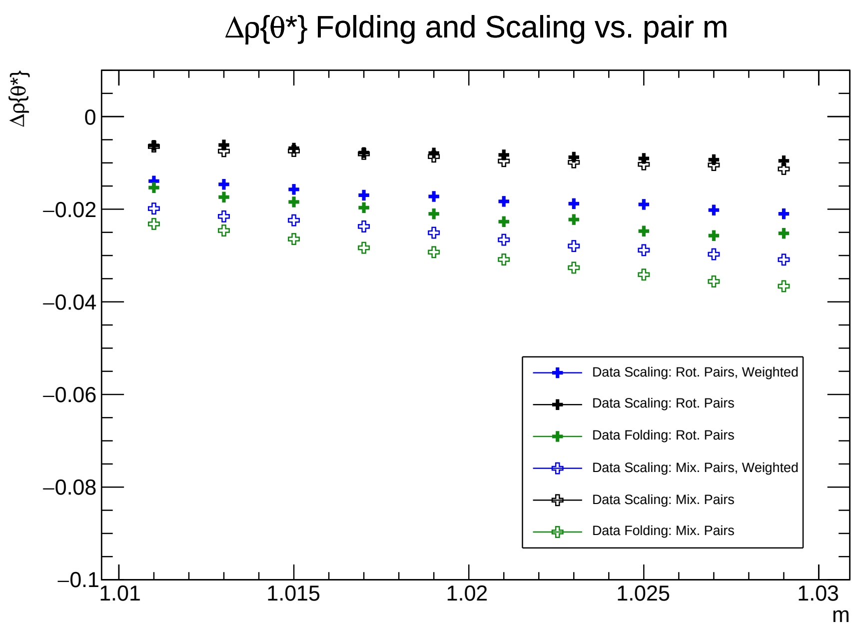

Figure 4.7. Example of combinatorial $\Delta\rho\{\theta^*\}$ vs. kaon pair invariant mass. All kaons in data without weighting (black), kaons weighted to have ϕ-meson decay kinematics (blue), kaons from decays of ϕ-mesons taken from published data without detector effects (green). Filled markers are pairs formed from rotation and open markers are pairs from mixed events.

ϕ-Meson Decay Kaons Without Detector Effects (Data Folding)

In the previous subsection, we have obtained the $\Delta\rho\{\theta^*\}$ of combinatorial pairs of kaons from real data, with kinematics identical to the ϕ-meson decay kaons, after all detector effects. To know the effects of imperfect detectors and finite acceptance, we need to know the $\Delta\rho\{\theta^*\}$ of these kaon pairs before any detector effects. We can then compare the two values of $\Delta\rho\{\theta^*\}$, with and without detector effects, to derive a correction. To get ϕ-meson decay kaons without detector effects, we generate and decay ϕ-mesons according to published data and calculate the $\Delta\rho\{\theta^*\}$ vs. m_{inv}.

Generally, we need the ϕ-meson $p_\perp$ spectrum (and dN/dy multiplicity), and $v_2(p_\perp)$ in each centrality. The relevant published ϕ are:

- 200 GeV ϕ-meson $p_\perp$ spectra and $v_2(p_\perp)$ [25, 26]
- 200 GeV ϕ-meson dN/dy multiplicity as a function of centrality [27]
- 200 GeV charged hadron $v_2(\text{cent}, p_\perp)$ [28]
- 62.4 GeV ϕ-meson transverse mass $m_\perp$ spectra [27]
- 39, 27, 19.6, and 11.5 GeV ϕ-meson $p_\perp$ spectra [29]
- 62.4, 39, 27, 19.6, and 11.5 GeV ϕ-meson v_2 [30]

At a particular energy and centrality bin, we fit the ϕ-meson $p_\perp$ spectrum in each centrality bin by 4.7

$$f(p_\perp) = \frac{d^2N}{p_\perp dp_\perp} = a\left(1 + \frac{\sqrt{p_\perp^2 + m_0^2} - m_0}{c}\right)^d \tag{4.7}$$

where parameter m_0 is the ϕ-meson mass and a,c, and d are free parameters, we fit the range [1.0,6.0] in ϕ-meson $p_\perp$. If we are missing ϕ-meson $p_\perp$ spectrum in a given centrality bin, we use the one from a wider bin; see details of this procedure in Table 4.1 for 200 GeV and Table 4.2 for 27 GeV. The $p_\perp$ spectra fits to 200 GeV data can be seen in Fig. 4.8. The fits to other data can be found in Appendix, Figs. B.1-B.5. The fit parameters for all available energies and centralities are tabulated in Tables B.2-B.7. The fit function, multiplied by $p_\perp$, is used for the purposes of generating $p_\perp$ of ϕ-meson. In this study we only generate ϕ-meson within $1.2 < p_\perp < 5.4$ GeV/c.

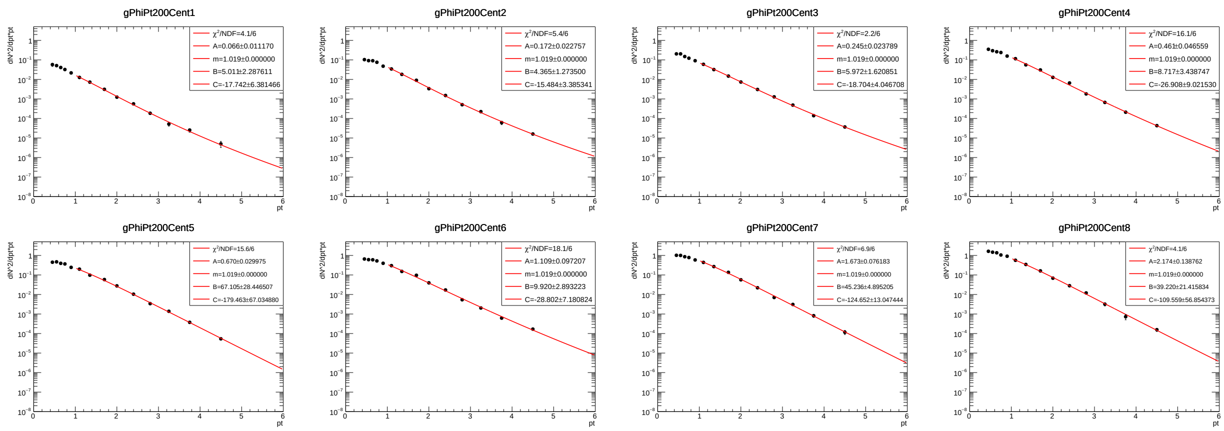

Figure 4.8. Fits of published ϕ-meson $p_\perp$ spectra using Eq. 4.7 in each centrality of Au+Au collisions at 200 GeV. These are the 8 ϕ-meson $p_\perp$ spectra listed in the middle column of Table 4.1.

We need the ϕ-meson v_2 for our toy-model data folding simulation. The ϕ-meson v_2 measurements have large uncertainties and are not well measured at most energies. At a given energy we typically only have ϕ-meson $v_2(p_\perp)$ in a wide centrality bin. Even at 200 GeV where the ϕ-meson v_2 is best measured, the uncertainties are relatively large. We thus resort to the v_2 measurement of charged hadrons at 200 GeV which is most extensively measured, see Fig. 4.9. We assume the v_2 $p_\perp$-dependencies of the ϕ-meson at all energies are as same as that of the charged hadrons at 200 GeV. This is reasonable because it has been empirically observed that hadron $v_2(p_\perp)$ in relativistic heavy ion collisions follow the so-called NCQ (Number of Consituent Quarks) scaling, possibly rooted in quark coalescence in forming hadrons, and the NCQ scaling is nearly independent of collision energy. We further assume that the centrality dependence of the ϕ-meson v_2 is as same as charged hadron v_2. This is reasonable because the centrality dependence of v_2 is mainly determined by the collision geometry, and it is also independent of the collision energy. Once we have the parameterization of the charged hadron $v_2(\text{cent}, p_\perp)$ at 200 GeV, we scale it to the measured ϕ-meson v_2 at a given energy to be treated as the ϕ-meson $v_2(\text{cent}, p_\perp)$, now with fine centrality and pt binning. For example, suppose the ϕ-meson $v_2(p_\perp)$ is measured only in a wide centrality bin 10-40% at a given energy: we average the parameterizations of the charged hadron $v_2(p_\perp)$ at 200 GeV over the centrality range of 10-40%, weighted by pion multiplicities at 200 GeV, see Fig. 4.10; we then take the ratio of the measured ϕ-meson $v_2(p_\perp)$ over the averaged parameterization and fit it with a constant, see Fig. 4.11; and finally we scale the parameterized charged hadron $v_2(p_\perp)$ in each narrow centrality bin within 10-40% by this fit constant, and treat the resultant parameterization as the ϕ-meson $v_2(\text{cent}, p_\perp)$ at the given energy.

We list in Table 4.1 for 200 GeV and Table 4.2 for 27 GeV to be specific how the ϕ-meson $v_2(p_\perp)$ was parameterized and how the wide centrality bin $p_\perp$ spectra are used. The tables for the other energies can be seen in Appendix B Table B.8 - B.9.

Table 4.1. Details of ϕ-meson $p_\perp$ spectra measurements and how the ϕ-meson $v_2(p_\perp)$ are parameterized in Au+Au collisions at 200 GeV, used in our Data Folding procedure. Here, "scaled Hadron" always means Hadron $v_2(\text{cent}, p_\perp)$ at 200 GeV scaled to that of ϕ-meson at a given energy. To get the scaling number in 10-40% we average the charged hadrons over 10-40% weighted by pion multiplicity at 200 GeV. Since we do not have ϕ-meson v_2 measurements in 0-10% centralities, we use the same scaling factor for 10-40% centrality.

StRefMultCorr Centrality in DATA	ϕ-meson $p_\perp$ spectra in data folding	ϕ-meson v_2 in data folding
00-05%	empty	scaled Hadron 00-05% to Pub. 10-40% ϕ
05-10%	Pub. 0-10	scaled Hadron 05-10% to Pub. 10-40% ϕ
10-20%	same	scaled Hadron 10-20% to Pub. 10-40% ϕ
20-30%	same	scaled Hadron 20-30% to Pub. 10-40% ϕ
30-40%	same	scaled Hadron 30-40% to Pub. 10-40% ϕ
40-50%	same	scaled Hadron 40-50% to Pub. 40-80% ϕ
50-60%	same	scaled Hadron 50-60% to Pub. 40-80% ϕ
60-70%	same	scaled Hadron 60-70% to Pub. 40-80% ϕ
70-80%	same	scaled Hadron 70-80% to Pub. 40-80% ϕ

More specifically, the outline of the parameterization of ϕ-meson $v_2(p_\perp)$ is as follows:

1) Fit Published charged hadron $v_2(p_\perp, \text{cent})$ at 200 GeV with a parameterization, f_{had}. The forms of f_{had} are Eq. 4.8, Eq. 4.10, and Eq. 4.9 below.

2) Average f_{had}'s over centrality to be in the same centrality range as published ϕ-meson $v_2(p_\perp)$ at a given energy.

Table 4.2. Details of ϕ-meson $p_\perp$ spectra measurements and how the ϕ-meson $v_2(p_\perp)$ are parameterized in Au+Au collisions at 27 GeV, used in our Data Folding procedure. Here we repeat the 40-60% and 60-80% published ϕ-meson $p_\perp$ spectra to fill in the finer centrality bins. For ϕ-meson v_2, we only have MB published data, so all charged hadron 200 GeV $v_2(\mathrm{cent}, p_\perp)$ are averaged and scaled to the published data.

StRefMultCorr Centrality in DATA	ϕ-meson $p_\perp$ spectra in data folding	ϕ-meson v_2 in data folding
00-05%	empty	scaled Hadron 00-05% to Pub. 00-80% ϕ
05-10%	0-10 %	scaled Hadron 05-10% to Pub. 00-80% ϕ
10-20%	same	scaled Hadron 10-20% to Pub. 00-80% ϕ
20-30%	same	scaled Hadron 20-30% to Pub. 00-80% ϕ
30-40%	same	scaled Hadron 30-40% to Pub. 00-80% ϕ
40-50%	40-60%	scaled Hadron 40-50% to Pub. 00-80% ϕ
50-60%	40-60%	scaled Hadron 50-60% to Pub. 00-80% ϕ
60-70%	60-80%	scaled Hadron 60-70% to Pub. 00-80% ϕ
70-80%	60-80%	scaled Hadron 70-80% to Pub. 00-80% ϕ

3) Take the ratios of the measured ϕ-meson $v_2(p_\perp)$ at a given energy and centrality range to the average fit function from step 2), example in Fig. 4.10. Fit the ratios with a constant, see Fig. 4.11.

4) Multiply the fitted function from step 1) by this fit constant. Treat the scaled $v_2(p_\perp, \mathrm{cent})$ as the ϕ-meson $v_2(p_\perp, \mathrm{cent})$.

We currently use three v_2 parameterizations:

- An Gu's NCQ scaling function [31],

$$f\left(\frac{KE_\perp}{n_q}\right) = \frac{KE_\perp}{n_q}\left(p_0 + p_1\frac{KE_\perp}{n_q}\right)\mathrm{e}^{-p_2\frac{KE_\perp}{n_q}}\,. \tag{4.8}$$

- Xin Dong's NCQ scaling function [32],

$$f\left(\frac{KE_\perp}{n_q}\right) = \frac{p_0}{1+\exp\left(-\frac{\frac{KE_\perp}{n_q}-p_1}{p_2}\right)} - p_3\,. \tag{4.9}$$

In this thesis we have sometimes referred to it as Jie's parameterization [33] which adapted the original formula in [32].

- Linear function in $p_\perp$,

$$f(p_\perp) = p_0 \times v_2 \tag{4.10}$$

We use multiple parameterizations of $v_2(p_\perp)$ because we do not know the true ϕ-meson $v_2(p_\perp)$ precisely. Typically, ϕ-meson data are published in only one centrality range, and the statistical errors are large such that the data can accommodate several $v_2(p_\perp)$ parameterizations in a given centrality range. For NCQ scaling, sometimes the transverse kinetic energy $KE_\perp$ is used as a variable instead of $p_\perp$,

$$KE_\perp = m_\perp - m_0\,, \tag{4.11}$$

where $m_\perp = \sqrt{p_\perp^2 + m_0^2}$ is the transverse mass. This is because it is empirically found that the NCQ scaling is better in $KE_\perp$ than in $p_\perp$.

Each parameterization v_2 will slightly change the decay kaon kinematics and, therefore, the $\langle\cos^2\theta^*\rangle$ vs. m_{inv} from data folding. On the other hand, $\langle\cos^2\theta^*\rangle$ from real data (data scaling) is fixed and the correction factor obtained from the difference between data folding and data scaling will be different. This makes a kind of "apparent" v_2 dependence in our data-driven correction procedure. We treat it as a systematic uncertainty in our correction due to the uncertainty in our knowledge of ϕ-meson $v_2(p_\perp)$. However, this does not necessarily mean that the correction must depend on $v_2(p_\perp)$. It is possible that the correction may not depend on v_2; for example, if the ϕ-meson $v_2(p_\perp)$ in the data is precisely known and therefore can be used in our folding, then the correction would be precisely known in terms of the given v_2. So, the uncertainty about the correction we refer to here is really because there is uncertainty on how well we know the true ϕ-meson v_2 in the data. This is really a source of systematic uncertainty in the correction because we do not know the precise ϕ-meson v_2 in data, to be used as input in data folding.

With the v_2 parameterization and $p_\perp$ spectra, we generate ϕ-meson with flat $|\eta| < 1.0$ and require each ϕ-meson rapidity to be $|y| < 1$. The ϕ-meson mass is fixed to be $m_0 =$

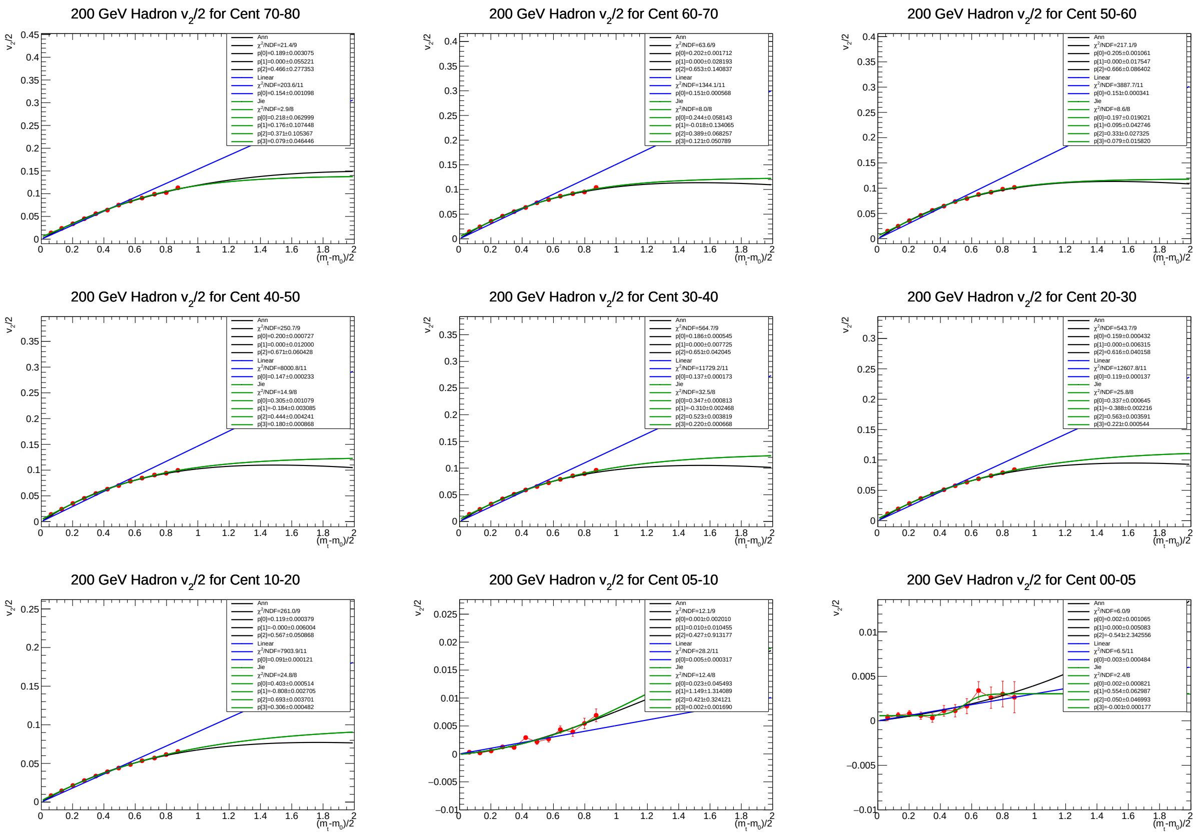

Figure 4.9. Fits to the published charged hadron $\frac{1}{2}v_2\left(\frac{1}{2}(m_\perp - m_0)\right)$ vs. $\frac{1}{2}(m_\perp - m_0)$ in each centrality bin in Au+Au collisions at 200 GeV. Three functional forms are used for fits, Eq. 4.8, 4.9, and Eq. 4.10. These are used to estimate the ϕ-meson v_2 centrality dependence, as we cannot get the ϕ-meson v_2 in different $p_\perp$ and centrality bins for all beam energies.

1.019 GeV/c^2 for now (previously we used a Breit-Wigner mass distribution with width $\tau = 0.005$ GeV/c^2). Although using fixed ϕ mass or Breit-Wigner mass does not really have any affect on the result, using a fixed mass m_0 makes $m_\perp - m_0$ slightly easier to evaluate.

In addition to ϕ-meson, there are some event generation details. Each event is assigned a centrality bin from 00-80% to be consistent with the centrality definition in data; these bins are generated from a uniform distribution. The ϕ-meson multiplicity depends on the centrality and is taken from a Poisson distribution with mean $3 \times \frac{dN}{dy}$ at 200 GeV. These multiplicity values are tabulated in Table B.1 in Appendix B **??**. The multiplicity is only

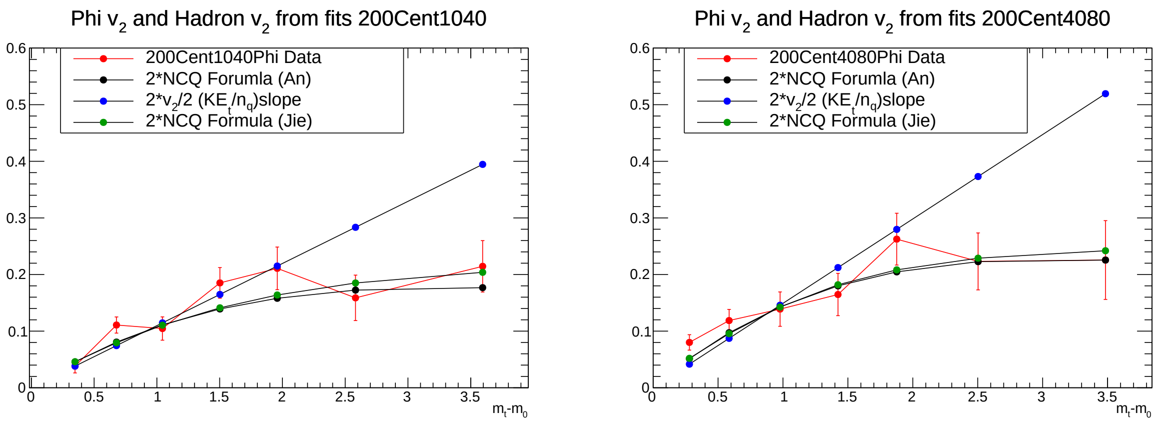

Figure 4.10. Published ϕ-meson v_2 as a function of $m_\perp - m_0$ in red for 10-40% (left) and 40-80% (right) centralities in Au+Au collisions at 200 GeV. The pion multiplicity weighted average $\langle v_2 \rangle$ of charged hadrons from the corresponding narrow centrality bins are shown using the three v_2 parameterizations: Linear (blue), Eq. 4.8 (black), and Eq. 4.9. This is how we compare the charged hadron v_2 parameterizations with the published ϕ-meson v_2 since we have limited measurements of the ϕ-meson v_2. We plot $2 * v_2$ slope is in $m_\perp - m_0$ space for demonstration, for the Data Folding a $v_2 \times p_\perp$ slope is used, as a slope in $p_\perp$ is more physical than a slope in $m_\perp - m_0$.

relevant for overall normalization and combinatorial statistics, but not important for the numerical value of the extracted $\Delta\rho$ correction.

For each event we generate a reaction plane (or more precisely, participant plane) angle from a flat azimuthal distribution [0,2π], for the purpose of generating the ϕ-meson azimuthal angle with v_2. For the analysis of the decay pairs, we use EP's from two subevents (East and West). To account for the finite EP resolution we generate a Δ_{EP} for each subevent EP and add it to the generated reaction plane angle. This Δ_{EP} is generated from a Gaussian centered at zero with $\sigma = \sqrt{-\frac{\log R}{2}}$ where R is the subevent ψ_2 resolution from data in each centrality at each energy.

After all event details and ϕ-meson kinematics are generated, we decay each ϕ-meson into a K^+K^- pair where the kaon mass is set to be $m_0 = 0.495$ GeV/c^2. The polar angle (θ^*) is generated from the $\frac{dN}{d\cos\theta^*}$ distribution according to Eq. 1.1, and the azimuthal angle of the decay is generated from a flat distribution $[0, 2\pi]$.

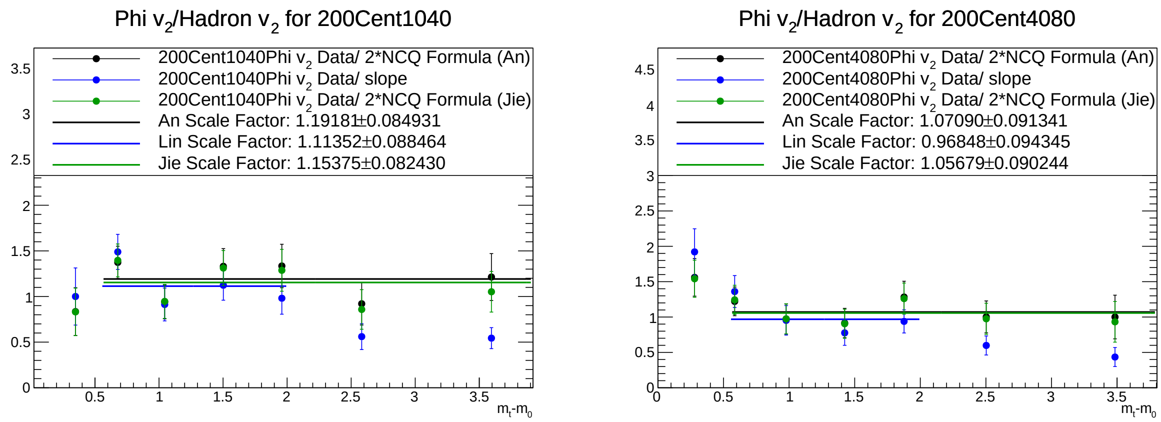

Figure 4.11. Ratios of published ϕ-meson v_2 over charged hadron v_2 from Fig. 4.10, fitted with a constant. These constant scaling factors make the average charged hadron v_2 equal to the ϕ-meson v_2 and allow us to get an approximate centrality dependence for the ϕ-meson v_2, since we do not have many centrality differential measurements for the ϕ-meson v_2. Scaling factors for the other energies/runs can be seen in the Appendix, in Fig.A.2.

To form the $\Delta\rho\{\theta^*\}$ vs. kaon pair m_{inv}, we keep all decay kaons (no kinematic cuts on individual decay tracks). We then calculate the $\langle\cos^2(\theta^*)\rangle$ and pair mass for each combinatorial OS Rotated pair (any K^+K^- pair with the K^- ratoted by π in azimuth) in the same event and cut on the pair $1.2 < p_{\perp,\mathrm{pair}} < 5.4$ and $|y_{\mathrm{pair}}| < 1$ as in data. To calculate the $\langle\cos^2(\theta^*)\rangle$ of a given pair we first determine the subevent ψ_2 to be used based on the pair η (opposite-η subevent is used). The subevent EP is smeared by its resolution as aforementioned. We then calculate $\hat{n} = (\cos(\psi_{2,\mathrm{sub}} - \frac{\pi}{2}), \sin(\psi_{2,\mathrm{sub}} - \frac{\pi}{2}), 0)$, which is the direction in the transverse plan perpendicular to the subevent EP (i.e. the direction of orbital angular momentum modulo the EP resolution). The $\cos\theta^*$ value is then calculated from $p^*_{3k} \cdot \hat{n}$ where p^*_{3k} is the normalized 3-momentum of daughter kaon in the parent rest frame (3-vector momentum is just the spatial components of the kaon 4-vector momentum). To get p^*_{4k}, we form the kaon pair 4-vector and calculate the pair β vector and apply $-\beta$ to a daughter kaon's 4-vector.

We follow the same procedure above for mixed events as well. In the case of mixed event each event is mixed with one other event in the same centrality bin. For mixed event pairs, the event plane of the "current" event is used; basically there is an EP mismatch between mixed events as in data.

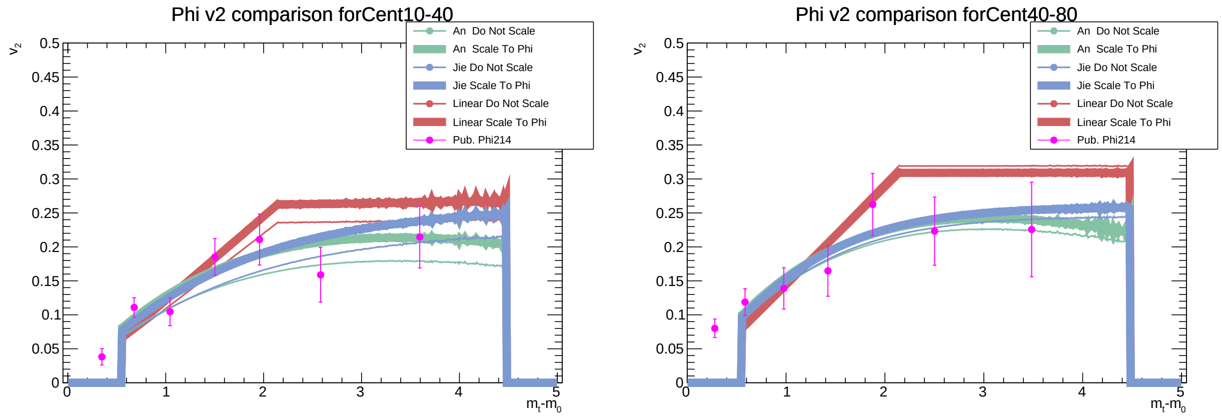

Figure 4.12. The three v_2 parameterizations of the published charged hadron v_2 data in Au+Au collisions at 200 GeV, averaged for the two centrality ranges available for the ϕ-meson v_2 measurements, compared with the published ϕ-meson data. Thicker curves are scaled to the published ϕ data, and the thinner curves are before scaling to published ϕ data. Plots for the other energies can be seen in Appendix A. Fig A.1.

In summary, this data folding allows us to get the decay kaon $\Delta\rho\{\theta^*\}$ vs. kaon pair invariant mass without any detector or finite acceptance affects. The finite EP resolution is accounted for by using the resolution from data. The difference between the $\Delta\rho\{\theta^*\}$ in this section and the previous section is the effects of imperfect detector and finite acceptance.

Corrections and Systematic Uncertainties

The difference between the kaons generated in the previous two sections are the effects of detector efficiency and finite acceptance on the ϕ-meson decay kaons. *We calculate the $\Delta\rho$ values of all those combinatorial kaon pairs and obtain their difference.* We assume this difference is the detector effort on the $\Delta\rho$ of the real ϕ-mesons because the detector should not know whether a K^+K^- pair is from a real ϕ-meson decay or not, given all the kinematics match. Therefore, the difference is our correction for the ϕ-meson $\Delta\rho\{\theta^*\}$. Figure 4.13 is an example for $1.2 < p_{\perp,\mathrm{pair}} < 5.4$ GeV/c for 20-60% centrality Au+Au collisions at $\sqrt{s_{\mathrm{NN}}} = 200$ GeV.

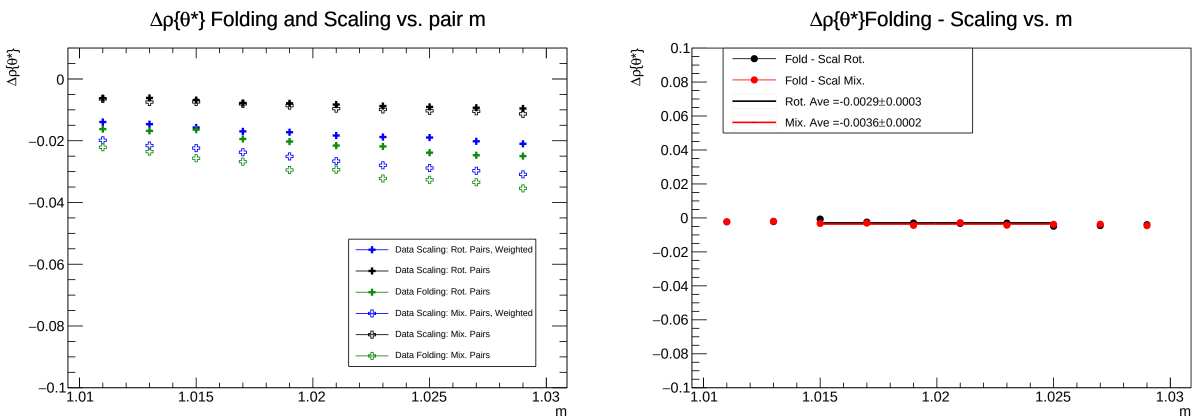

Figure 4.13. Example correction of ϕ-meson $\Delta\rho\{\theta^*\}$ in $1.2 < p_{\perp,\text{pair}} < 5.4$ GeV/c for 20-60% centrality Au+Au collisions at $\sqrt{s_{\text{NN}}} = 200$ GeV from Run 14. (Left) $\Delta\rho\{\theta^*\}$ vs. m_{inv} from the data scaling (blue) and data folding (green). (Right) The difference between folding and scaling for rotated pairs (black) and mixed-event pairs (red). This plot is the correction vs. m_{inv}; we fit the ϕ-meson mass peak region ($1.015 < m_{\text{inv}} < 1.025$ GeV/c^2) to get the correction at the ϕ-meson mass. Plots for other energies and runs collected in Appendix A Fig. A.5 -A.10.

In the following, we look at these differences (and the resulting corrections) for the ϕ-meson at different beam energies, $p_\perp$, and centrality, and summarize the associated systematic uncertainties.

We take the correction from rotated pairs using "Jie" v_2 parameterization Eq. 4.9 as our default. The main source of systematics on our data-driven corrections is the ϕ-meson v_2 uncertainty. Originally, we also considered the difference between rotated and mixed events as an estimate of the systematic uncertainty on the correction. However, this is not ideal as discussed in the MC Closure check of the data-driven correction in section 4.2.5. Mixed events have additional issues due to the EP mismatch between two events. So, we assign a flat 0.001 as estimate of the systematic uncertainty from the non-closure in addition to varying the ϕ-meson v_2 parameterization. We use the RMS of the two other v_2 parameterizations (both using rotated pairs) for the systematic uncertainty. The total 1σ systematic uncertainty is the quadratic sum of the two.

Figure 4.14 shows the systematic uncertainty assessment for detector effect correction for 200 GeV Run 14 data; those for other energies are in Appendix A; Figs. A.3 and A.4.

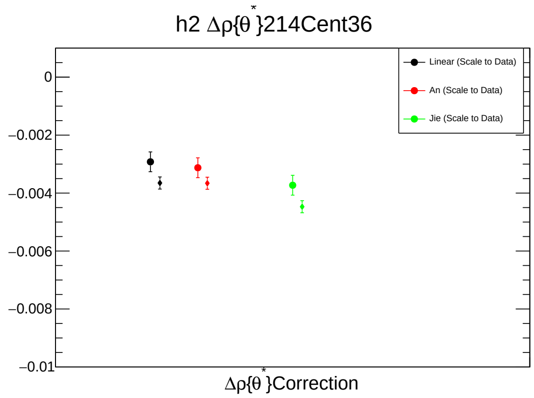

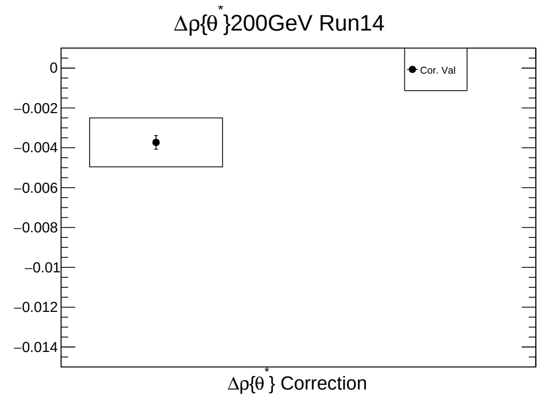

Figure 4.14. Systematics of the data-driven ϕ-meson $\Delta\rho$ correction for $1.2 < p_{\perp,\mathrm{pair}} < 5.4$ GeV/c in 20-60% centrality Au+Au collisions at 200 GeV from Run 14. (Left) $\Delta\rho\{\theta^*\}$ corrections from rotated (circle) and mixed-event (diamonds) pairs for different v_2 parameterizations. (Right) Barlow Systematic uncertainties from the variations in the left panel. The "Jie" "Rotated" correction is taken as the default, and the the RMS of the "Rotated" corrections using the two other v_2 parameterizations are taken as two source of systematic uncertainty summed in quadrature with a flat uncertainty of 0.001 from the non-MC Closure. Plots for the other runs/energies are in Appendix A, Fig. A.3 and A.4.

Figure 4.15 shows the resulting $\Delta\rho\{\theta^*\}$ correction and systematics at each beam energy in $1.2 < p_\perp < 5.4$ and Centrality 20-60%.

4.2.2 Data-Driven Corrections for $\Delta\rho\{\phi^*\}$

Voloshin Correction Formalism

The azimuthal angle, ϕ^*, is the projection of θ^* onto the transverse plane and can also be used to measure ρ_{00} or $\Delta\rho$ as proposed by Voloshin as in Eq. 4.5 [24]. The main advantage of the "$\Delta\rho\{\phi^*\}$ method" or "ϕ^* method" is that the detector corrections for this method can be analytically computed from data measurements, when the data is fully corrected for detector effects. The $\Delta\rho\{\phi^*\}$ correction differs from both methods of correcting the $\Delta\rho\{\theta^*\}$; embedding and our data-driven correction method. As argued by Voloshin, the main concern with $\Delta\rho\{\theta^*\}$ and the "standard" correction from embedding is that the efficiency and acceptance "entangles/couples" the spin alignment ($\Delta\rho\{\theta^*\}$) and flow (v_2).

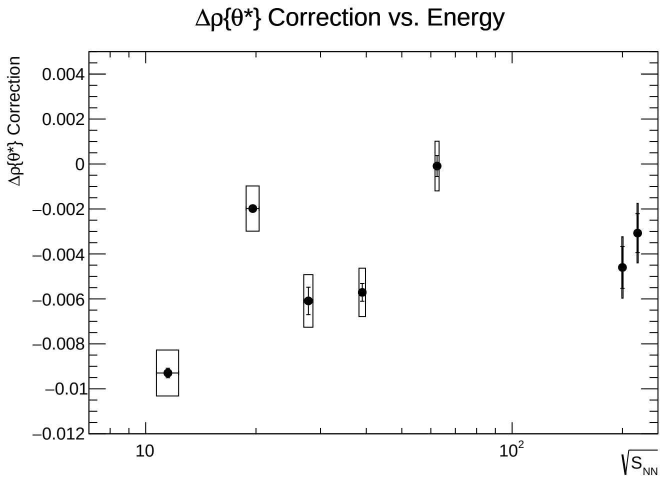

Figure 4.15. The $\Delta\rho\{\theta^*\}$ correction vs. collision energy for ϕ-meson $1.2 < p_{\perp,\mathrm{pair}} < 5.4$ GeV/c (the Run 11 and Run 14 points at 200 GeV are offset for clarity). Default correction values are taken from Rotated pairs with "Jie" v_2 parameterization Eq. 4.9. Systematic uncertainties from the RMS of the two other v_2 parameterizations and an additional 0.001 from the non-closure in MC checks. (Eq. 4.8 and 4.10).

Following Voloshin [24], the $\Delta\rho\{\phi^*\}$ in Eq. 4.5 is affected by detector effects and finite acceptance in a relatively simple way,

$$\Delta\rho\{\phi^*\}^{\mathrm{dir}} = \Delta\rho\{\phi^*\} - \frac{4}{3}a_2 v_2\,, \tag{4.12a}$$

$$a_2^{\mathrm{dir}} = a_2 - \frac{3}{4}v_2\Delta\rho\{\phi^*\}\,, \tag{4.12b}$$

$$v_2^{\mathrm{dir}} = v_2 - \frac{3}{4}a_2\Delta\rho\{\phi^*\}\,, \tag{4.12c}$$

where $\Delta\rho\{\phi^*\}^{\mathrm{dir}}$ is "directly observed" in experiments with detector effects and $\Delta\rho\{\phi^*\}$ is after correction for detector effects. In these equations, v_2 is the flow of the ϕ meson, $v_2 = \langle\cos 2(\phi - \psi_2)\rangle$, and a_2 captures the detector effects and is defined as

$$a_2 = \langle\cos 2(\phi^* - \phi)\rangle\,. \tag{4.13}$$

In Eqs. 4.12 the "true" v_2 and a_2 are used rather than the "dir", and the corrections for v_2 and a_2 in terms of the "dir" quantities depend on $\Delta\rho\{\phi^*\}$. Since the $\Delta\rho\{\phi^*\}$ signal is small (about 1%), the effects are negligible: $v_2 \approx v_2^{\mathrm{dir}}$ and $a_2 \approx a_2^{\mathrm{dir}}$.

Figure 4.16 shows the results for v_2 and a_2 as functions of beam energy in 20-60% centrality Au+Au collisions for ϕ-meson $1.2 < p_\perp < 5.4$ GeV/c. The a_2 and v_2 are relatively energy independent.

The quantity $-\frac{4}{3}a_2v_2$ would be the detector effect to be subtracted from the measured $\Delta\rho\{\phi^*\}^{\mathrm{dir}}$ according to Eq. 4.12a if the a_2 contains no physics. However, the a_2 in Eq. 4.13 is

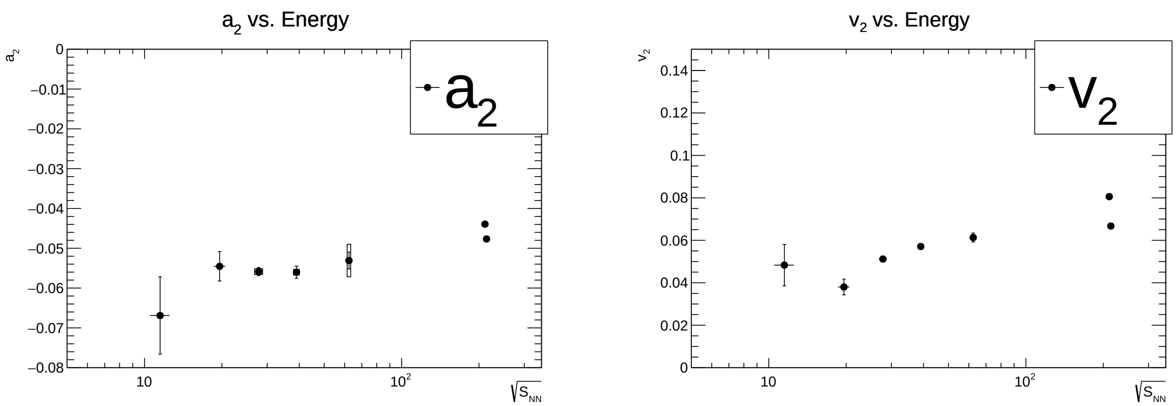

Figure 4.16. (left) a_2 (right) v_2 as functions of beam energy in 20-60% centrality Au+Au collisions for ϕ-meson $1.2 < p_\perp < 5.4$ GeV/c. Run 11 and Run 14 at 200 GeV are offset along the x axis for clarity.

effectively the helicity-frame spin alignment of Eq. 4.6. So, detector effect a_2 and any possible helicity-frame spin alignment cannot be distinguished. In other words, one cannot take a_2 directly calculated from data according to Eq. 4.13 and treat it as detector effect correction for $\Delta\rho\{\phi^*\}$ measurement because such a a_2 could contain possible physics (helicity-frame spin alignment).

Therefore, one needs to obtain the detector effect of a_2 by other means, for example, using embedding, or data-driven approach which we describe in the next subsection.

Data-Driven Correction for a_2

The a_2 is impacted by detector effects and was originally thought to only contain detector effects for the $\Delta\rho\{\phi^*\}$ method. However, as discussed above, the a_2 may also contain physics, and one such physics is helicity frame spin alignment. Therefore, we would like to get the detector effect a_2 in addition to the raw a_2 (and the difference would be a measure of the helicity frame spin alignment, modulo a multiplicative factor of $-4/3$). To get the $a_{2,\mathrm{det}}$ we will use the same method as $\Delta\rho\{\theta^*\}$ and compare the Data Folding a_2 vs. m_{inv} and the Data Scaling a_2 vs. m_{inv}. This correction method works for both $\Delta\rho\{\theta^*\}$ and a_2 (effectively $\Delta\rho\{\phi^*\}$) as the Data Folding and Data Scaling do not have $\Delta\rho\{\theta^*\}$ or $\Delta\rho\{\phi^*\}$ signal. The difference (data scaling $-$ data folding) at the ϕ-meson mass would be the detector effect $a_{2,\mathrm{det}}$. The simulation and weighting details for the Data Folding and Data Scaling are the same as for $\Delta\rho\{\theta^*\}$; only the quantity of interest is different. Figure 4.17 gives an example of the Data Folding and Data Scaling for the $\langle\cos 2\,(\phi^* - \phi)\rangle$ (or equivalently the a_2) vs. m_{inv}.

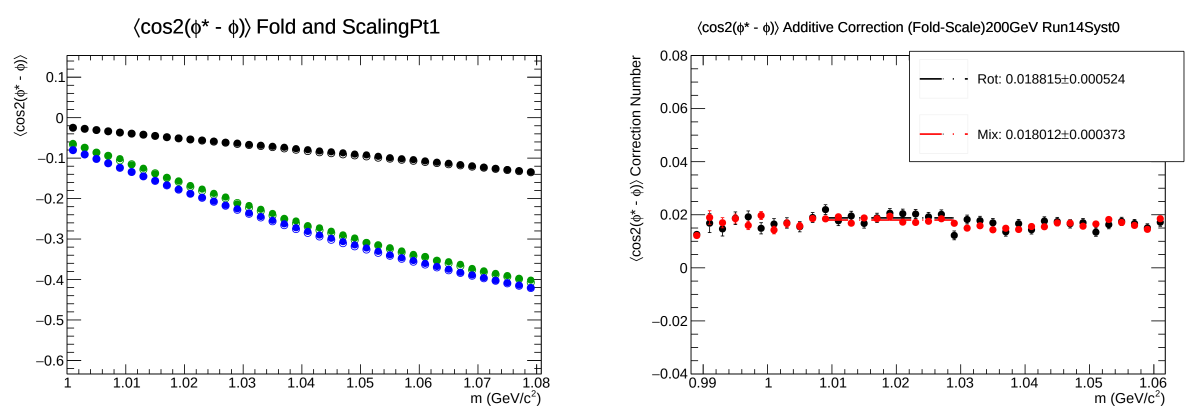

Figure 4.17. (Left) Combinatorial kaon pair $\langle\cos 2\,(\phi^* - \phi)\rangle$ vs. mass for all Rot./Mix pairs (black), weighted Rot./Mix kaon pairs (blue), and Rot./Mix pairs from Data Folding (green). (Right) (data folding $-$ data scaling) for the a_2 vs. mass, (i.e. Green minus Blue from the left panel). The value at the ϕ-meson is correction for a_2. Data are from 20-60% centrality Au+Au collisions at 200 GeV for $1.2 < p_{\perp,\mathrm{pair}} < 5.4$ GeV/c. In this plot, we also cut on the comb. ϕ-meson $p_\perp$ to be in the same $p_\perp$ range as the real ϕ-meson. This should have a negligible effect on the result, but is somewhat inconsistent with our Data Folding and Data Scaling procedure.

The a_2 correction from our data-driven method has similar systematics to $\Delta\rho\{\theta^*\}$ correction. For example, there is a small variation in the extracted $a_{2,\mathrm{det}}$ due to the uncertainty in the true ϕ-meson v_2. Figure 4.18 shows an example of the systematics for the $a_{2,\mathrm{cor}}$ vs. $p_\perp$ for 20-60% centrality Au+Au collisions at 200 GeV from Run 14. The a_2 correction is similar between Rotated and Mixed pairs which may be due to the fact that in Eq. 4.13 there is no explicit event plane dependence. The event plane mismatch is the main difference between rotated and mixed events. The a_2 corrections for other energies can be seen in the Appendix in Fig. 5.5.

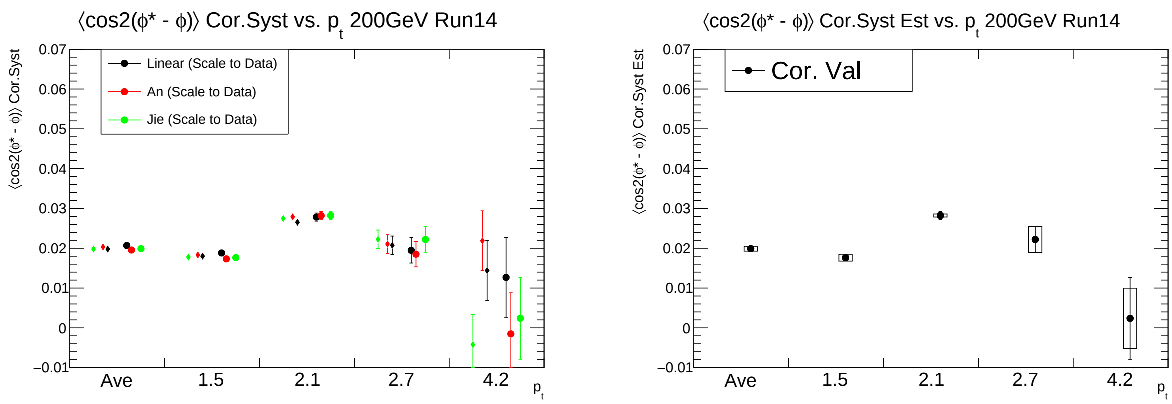

Figure 4.18. (Left) Example systematic variations for the $a_{2,\mathrm{cor}}$ vs. $p_\perp$, similar to Fig. 4.14. (Right) Barlow Systematic uncertainty in $a_{2,\mathrm{cor}}$ vs. $p_\perp$. The is calculated by data-driven method from (data folding − data scaling) of the quantity $\langle\cos 2(\phi^* - \phi)\rangle$. Data are from 20-60% centrality Au+Au collisions at 200 GeV for $1.2 < p_{\perp,\mathrm{pair}} < 5.4$ GeV/c. In this plot, we also cut on the comb. ϕ-meson $p_{\perp,\mathrm{pair}}$ to be in the same $p_{\perp,\mathrm{pair}}$ range as the real ϕ-meson. This should have a negligible effect on the result, but is somewhat inconsistent with our Data Folding and Data Scaling procedure, which ideally would have no cut on the comb. $p_{\perp,\mathrm{pair}}$.

Note that in the above narrative we have used $a_{2,\mathrm{det}}$ which is the detector a_2 and is (data scaling − data folding). The $a_{2,\mathrm{cor}}$ is the correction for a_2 due to detector effects, which is (data folding − data scaling), or $a_{2,\mathrm{cor}} \equiv a_{2,\mathrm{det}}$. In Fig. 4.19, we collect the raw $a_{2,\mathrm{raw}}$, $a_{2,\mathrm{det}}$, and $a_{2,\mathrm{raw}} - a_{2,\mathrm{det}}$ and scale all by $-4/3$ to convert into $\Delta\rho\{\phi^*\}$. As seen in Fig. 4.19, the detector $a_{2,\mathrm{det}}$ seems to monotonically increase with beam energy from 11.5 GeV to 200 GeV. The difference $-\frac{4}{3}(a_{2,\mathrm{raw}} - a_{2,\mathrm{det}})$ (red points in Fig. 4.19) is supposed to be the helicity-frame spin alignment measurement before EP resolution correction. The results suggest that there is indeed significant helicity-frame spin alignment of the ϕ-meson.

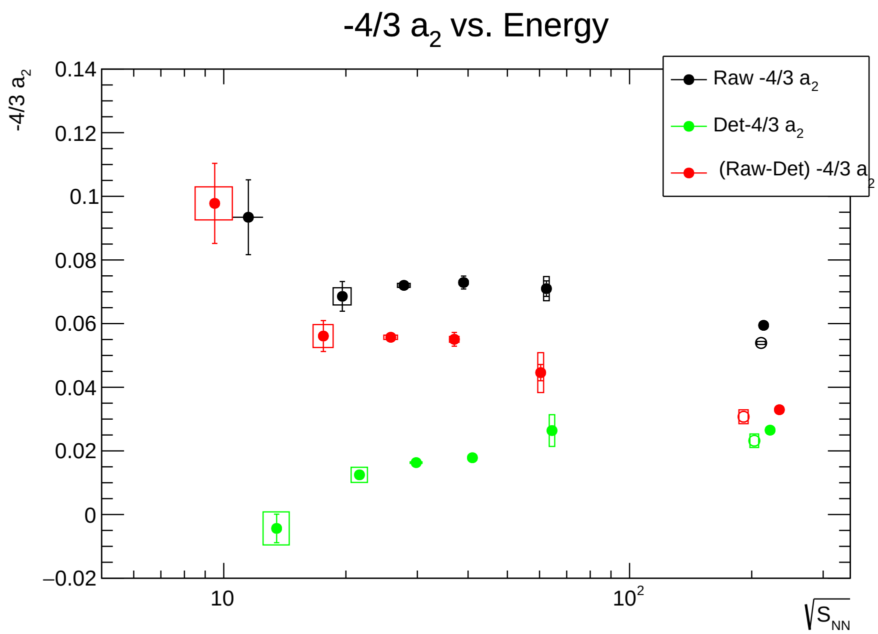

Figure 4.19. Raw a_2 (black), Detector a_2 (green), and (Raw − Detector) a_2 (red) vs. beam energy. All a_2 are scaled by $-4/3$. Data are 20-60% centrality Au+Au collisions, for $1.2 < p_{\perp,\text{pair}} < 5.4$ GeV/c. In this plot, we also cut on the comb. ϕ-meson $p_{\perp,\text{pair}}$ to be in the same $p_{\perp,\text{pair}}$ range as the real ϕ-meson. This should have a negligible effect on the result, but is somewhat inconsistent with our Data Folding and Data Scaling procedure, which ideally would have no cut on the comb. $p_{\perp,\text{pair}}$. Additionally, there is an additional $\sim 1\%$ uncertainty (not plotted) from the poor MC closure for a_2 as show in Section 4.2.5.

4.2.3 Discussion on Data-Driven Corrections

For correction, we want to know the detector effect on the ϕ-meson decay K^+K^- pairs. In our data-driven method, we take the combinatorial K^+K^- pairs (rotating one by π in azimuth or by mixed events) from ϕ-meson decays both in data-folding and in real data within the ϕ-meson mass region. Since the ϕ-mesons in real data are identified statistically, we use all measured kaons to mimic the decay koans by applying a 3-D weight in kaon $(p_\perp, \eta, \phi - \psi_2)$. Let us call those combinatorial K^+K^- pairs pseudo-ϕ-mesons. The pseudo-ϕ-mesons will not have the identical kinematics of the real ϕ-mesons but smeared, i.e. the pseudo-ϕ-meson kinematics will be distributed about the real ϕ-meson kinematics. We do not apply kinematic cuts on those pseudo-ϕ-mesonsor "combinatorial" ϕ-meson. However, the correction one needs is for those rest-frame $\phi \to K^+K^-$ pairs boosted by the real ϕ-meson kinematics, and the data-driven correction we obtain are for the rest-frame pseudo-$\phi \to K^+K^-$ pairs boosted by kinematics smeared about the real ϕ-meson kinematics. The assumption of the data-driven method is that the kinematics smearing averages out and these two corrections are equal. Nevertheless, this needs to be checked out.

4.2.4 Checks of Data-Driven Corrections

We have done various checks of the Data-Driven Corrections for $\Delta\rho\{\theta^*\}$ and a_2. These checks are described in this section.

Check of Different Kaon Sample in Data Folding

In this section we check how well the Data Scaling (see Sec. 4.2.1) works in a toy model with known background and ϕ-meson decay kaons. We want to see if the weighted, all kaon, combinatorial $\Delta\rho\{\theta^*\}$ vs. m_{inv} is the same as the ϕ-meson decay kaon combinatorial $\Delta\rho\{\theta^*\}$ vs. m_{inv}. This check is primarily to gauge whether the correction depends on the origin of the kaons used to form combinatorial pairs.

In *data folding*, we generate and decay ϕ-mesons, and use combinatorial pairs of those decay kaons either by the rotation or the mixed-event technique. In *data scaling*, we scale all the measured kaons to match the ϕ-meson decay kaon kinematics. Majority of those measured kaons are not from ϕ-meson decays. The question arises whether the different origins of the kaons would cause any issue or not.

To check this question, we take the Data Folding simulation for 200 GeV with Run 14 EP Resolution and add background kaons. The background kaons are generated with a Boltzmann $p_\perp$ distribution with a Blast-Wave Boost of centrality 40-50% [34]. The background kaon $v_2 = 0.12\times p_\perp$, cutoff at $p_\perp = 2$ GeV/c, and the background kaons are generated with flat η. The background kaon multiplicity $(K^+ + K^-)$ per event is generated from a Poisson distribution with an average value of 3×18.72, also approximate from [34]. This is sufficient for this check.

After including background kaons, we follow the Data Scaling procedure as outlined in Sec 4.2.1. In the first iteration, we get the 3D histograms of decay kaon kinematics for K^+ and K^- and divide by the 3D kinematic histograms of all kaons (decay + background), for each centrality. In the second iteration, we apply this single kaon weight to all kaons and compare with a simulation of only ϕ-meson decay kaons. For this check we tag each track as coming from background or ϕ-meson decay. The results of this check can be seen in Fig. 4.20. Here the left plot shows that the weighted kaon $p_\perp$ histogram agrees with the $p_\perp$ histogram of the pure ϕ-meson decay kaons, as expected. In the right plot of Fig. 4.20, we check the difference between the combinatorial $\Delta\rho\{\theta^*\}$ of pure ϕ-meson decay kaons and that of the weighted kaons and the difference is consistent with zero. Data Scaling does capture the ϕ-meson decay kaon kinematics and gives the same combinatorial $\Delta\rho\{\theta^*\}$ as pure ϕ-meson decay case. *Thus, the conclusion is that the $\Delta\rho\{\theta^*\}$ correction does not depend on the kaon sample used for combinatorial pairs.*

In addition to this check, we can perform the same check but instead of tagging each kaon as coming from a ϕ-meson decay or background, we statistically identify kaons as in data analysis (see Data Scaling in Section 4.2.1). We do this by going through all kaon pairs in an event and forming Peak Pairs and Rot. Peak pairs. Decay kaon kinematics are then identified from (Peak Pairs $-$ properly normalized Rot. Pairs), divided by all kaons, and applied in the section iteration as a weight to all single kaons. The results of this check can be seen in Fig. 4.21. The $\Delta\rho\{\theta^*\}$ between the two kaon groups agree well, and the difference between the two groups is consistent with zero.

Input ρ_{00} Dependence of Corrections

In this section we look at the effect of input non-zero ϕ-meson $\Delta\rho$ on the $\Delta\rho\{\theta^*\}$ and a_2 correction. The ϕ-meson $\Delta\rho\{\theta^*\}$ correction should not depend on input physics of ϕ-meson ρ_{00}; the correction should be independent of the physics signal. On the other hand, a_2 is affected by the input ρ_{00} as they are coupled variables.

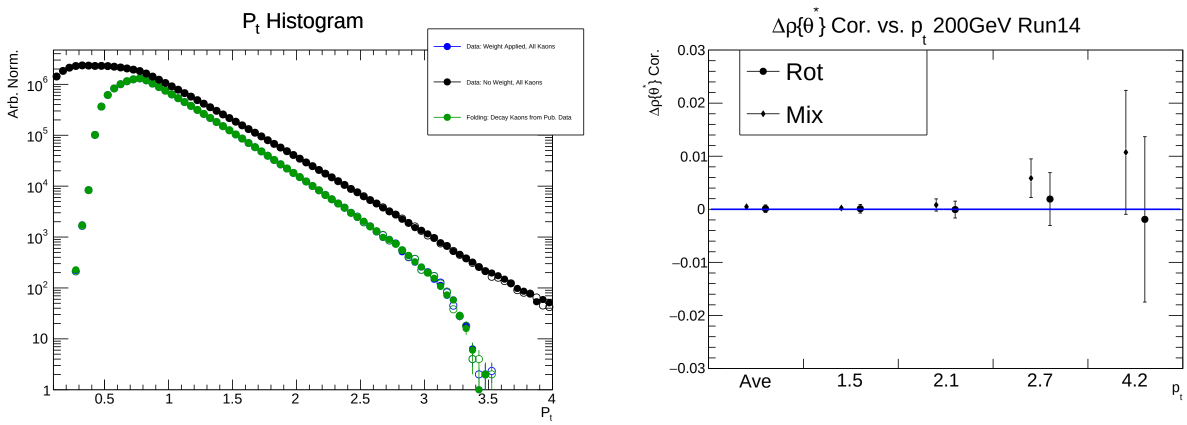

Figure 4.20. Check of kaon sample used for combinatorial pairs.(Left) $p_\perp$ histogram of all kaons (black), weighted kaons (blue), ϕ-meson decay kaons only (green); for K^+ (filled) and K^- (open). (Right) Difference in $\Delta\rho\{\theta^*\}$ of combinatorial pairs from pure ϕ-meson decay kaons and from weighed total kaons (decay and background kaons) in each ϕ-meson $p_\perp$ bin. Both cases of rotated and mixed-event combinatorial pair $\Delta\rho\{\theta^*\}$ are shown. Checks are done for 20-60% Centrality Au+Au collisions. In this plot, we also cut on the comb. ϕ-meson $p_{\perp,\text{pair}}$ to be in the same $p_{\perp,\text{pair}}$ range as the real ϕ-meson. This should have a negligible effect on the result, but is somewhat inconsistent with our Data Folding and Data Scaling procedure, which ideally would have no cut on the comb. $p_{\perp,\text{pair}}$.

To obtain our data-driven correction for $\Delta\rho\{\theta^*\}$ we run Data Folding (Sec. 4.2.1) with ϕ-meson input $\Delta\rho = 0$. Our correction method calculates the $\Delta\rho\{\theta^*\}$ of combinatorial pairs of "decay" kaons vs. invariant mass in Data Folding and Data Scaling. The correction should not depend on the ϕ-meson ρ_{00} physics signal. However, the ϕ-meson ρ_{00} affects somewhat the kinematics of the decay kaons, so we want to check the Data Folding and the obtained correction for $\Delta\rho\{\theta^*\}$ using different input ρ_{00} for ϕ-meson. Reminder: our correction is obtained from the difference between Data Folding and Data Scaling, where the Data Folding is simulation and Data Scaling is real data.

For this check we take the Run 14 200 GeV Au+Au Data Folding and run with various input ρ_{00} and the Data Scaling (from real data) is fixed for all input ρ_{00} values. The results of this check can be seen in Fig. 4.22 and indeed, *the correction is independent of the input* ρ_{00} *for* ϕ*-meson.*

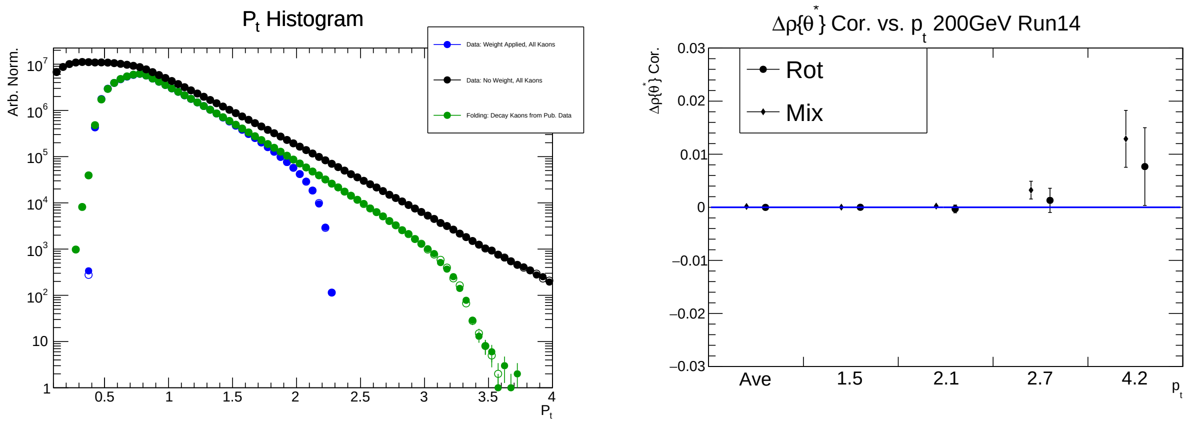

Figure 4.21. Kaon sample check by statistically identifying decay kaons. (Left) $p_\perp$ histogram of all kaons (black), weighted kaons where the weight histograms are derived as in data analysis (blue), ϕ-meson decay kaons only (green); for K^+ (filled) and K^- (open). Difference in $\Delta\rho\{\theta^*\}$ of combinatorial pairs from pure ϕ-meson decay kaons and from weighed total kaons (decay and background kaons) in each ϕ-meson $p_\perp$ bin. Both cases of rotated and mixed-event combinatorial pair $\Delta\rho\{\theta^*\}$ are shown. Checks are done for 20-60% Centrality Au+Au collisions. In this plot, we also cut on the comb. ϕ-meson $p_{\perp,\text{pair}}$ to be in the same $p_{\perp,\text{pair}}$ range as the real ϕ-meson. This should have a negligible effect on the result, but is somewhat inconsistent with our Data Folding and Data Scaling procedure, which ideally would have no cut on the comb. $p_{\perp,\text{pair}}$.

We repeat the same procedure to look at the detector/correction for a_2 vs input ϕ-meson ρ_{00} in Data Folding. The results of this check can be seen in Fig. 4.23 and in this case the $a_{2,\text{det}}$ linearly depends on the input ρ_{00}. This can be understood because a_2 is effectively a measure of the helicity-frame spin alignment, and the input global spin alignment $\Delta\rho$ is, in this case, projected onto the ϕ-meson momentum direction with the projection reduction factor of v_2, $a_2 \sim \Delta\rho\{\theta^*\} \times v_2$ [24]. In the case of $v_2 = 0$, there is no effect because the ϕ-meson momentum vector is random relative to the y direction; in the case of $v_2 = -1$, all ϕ-meson are in the same direction along y and $a_2 = \Delta\rho\{\theta^*\}$.

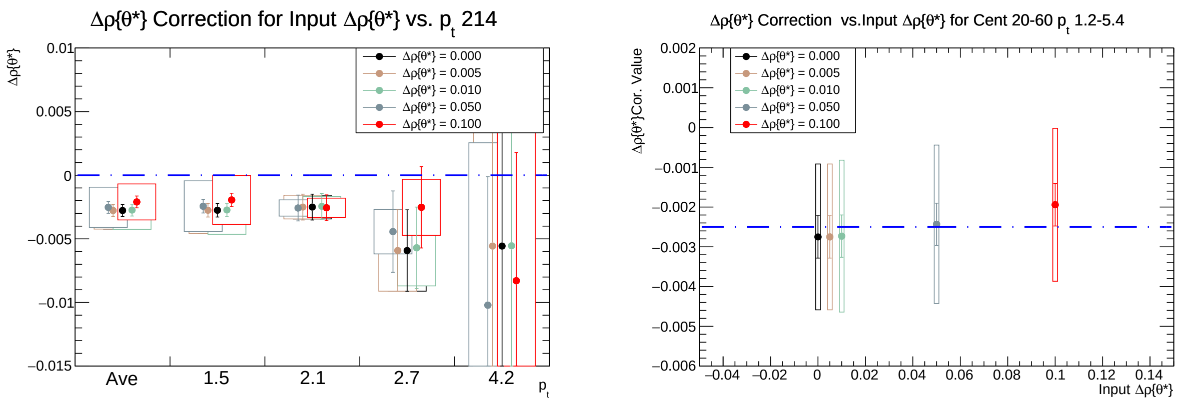

Figure 4.22. (Left) Correction for $\Delta\rho\{\theta^*\}$ as a function of $p_{\perp,\text{pair}}$ for various input ϕ-meson $\Delta\rho$ in Data Folding; Data Scaling is the same for all input ϕ-meson $\Delta\rho$ values. Barlow systematic uncertainties from v_2 parameterizations as described in Data Folding (Sec. 4.2.1). (Right) Average correction over $1.2 < p_{\perp,\text{pair}} < 5.4$ GeV/c vs. input ϕ-meson $\Delta\rho$, where the dashed line is to guide the eye. Data are 20-60% centrality Au+Au collisions at 200 GeV from Run 14. In this plot, we also cut on the comb. ϕ-meson $p_{\perp,\text{pair}}$ to be in the same $p_{\perp,\text{pair}}$ range as the real ϕ-meson. This should have a negligible effect on the result, but is somewhat inconsistent with our Data Folding and Data Scaling procedure, which ideally would have no cut on the comb. $p_{\perp,\text{pair}}$.

4.2.5 Toy Model MC Closure Test of the Data-Driven Correction Method

As previously discussed, the correction for ϕ-mesons in a given $p_\perp$ bin should be obtained using all Folding and Scaling kaon pairs with any $p_\perp$ (and any rapidity), rather than cutting on the Folding and Scaling pair $p_\perp$ to be the same as the ϕ-meson $p_\perp$ and cutting on $|y| < 1$. In general, these cuts cause a negligible difference in the results. As an example to get a correction for ϕ-meson with $1.2 < p_\perp < 5.4$ GeV/c we will generate ϕ-meson with that $p_\perp$ range in folding and decay into kaons, then form Rot. and Mix. pairs and include all pairs regardless of pair $p_\perp$. The only kinematic cut used to get the correction is the pair mass cut to be within the ϕ-meson mass peak range. This is so that each "combinatorial decay pair" (always taken to be an abbreviation for pairs of Rotated K^+K^- in the same event) looks like a ϕ-meson decay in its own pair rest frame. Similarly, in data scaling, we will apply weights to all single kaon tracks and keep all pairs in the ϕ-meson mass range regardless of the pair $p_\perp$.

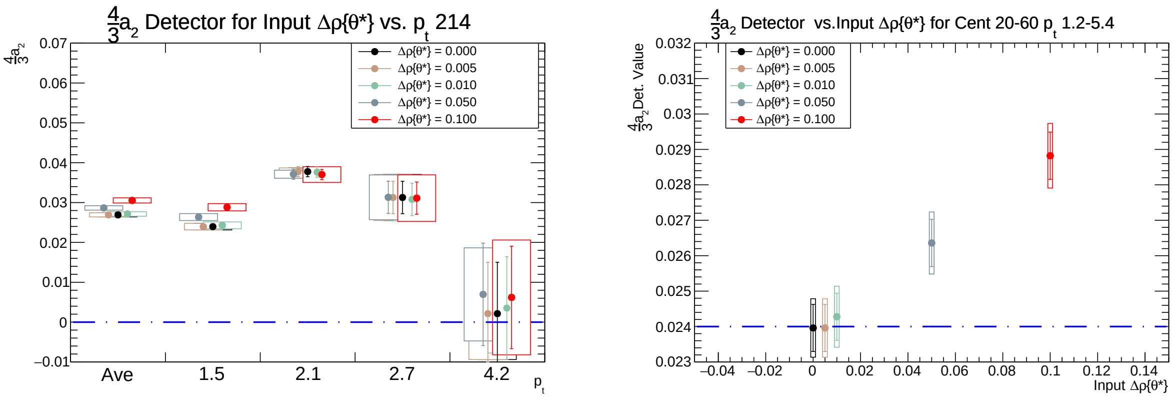

Figure 4.23. (Left) Correction for a_2 as a function of $p_{\perp,\text{pair}}$ for various input ϕ-meson $\Delta\rho$ in Data Folding; Data Scaling is the same for all input ϕ-meson $\Delta\rho$ values. Barlow systematic uncertainties from v_2 parameterizations as described in Data Folding (Sec. 4.2.1). (Right) Average correction over $1.2 < p_{\perp,\text{pair}} < 5.4$ GeV/c vs. input ϕ-meson $\Delta\rho$, where the dashed line is to guide the eye. Data are 20-60% centrality Au+Au collisions at 200 GeV from Run 14. In this plot, we also cut on the comb. ϕ-meson $p_{\perp,\text{pair}}$ to be in the same $p_{\perp,\text{pair}}$ range as the real ϕ-meson. This should have a negligible effect on the result, but is somewhat inconsistent with our Data Folding and Data Scaling procedure, which ideally would have no cut on the comb. $p_{\perp,\text{pair}}$. There is some additional uncertainty (not plotted) due to the poor MC closure for a_2 as seen in Fig. 4.28.

Generally, it is not straightforward to use the $\Delta\rho\{\phi^*\}$ and a_2 correction method. The main difficulty is that a_2 may not parameterize *all* detector effects in $\Delta\rho\{\phi^*\}$ or analogously $\Delta\rho\{\theta^*\}$. The a_2 parameter can be largely understood as one possible way to parameterize the efficiency effect on v_2 and $\Delta\rho\{\theta^*\}$ and some, maybe all, of the "interplay" between the two, in the case of $\Delta\rho\{\theta^*\}$. $\Delta\rho\{\phi^*\}$ is then best understood as a variable designed to be resilient to this interplay between ϕ-meson v_2 and $\Delta\rho\{\theta^*\}$. $\Delta\rho\{\phi^*\}$ can be corrected for this v_2 interplay with the efficiency correction by using Eq. 4.12a. However, a_2 could contain physics signal, e.g., helicity-frame spin alignment, and may have its own detector effects which could occur even if the ϕ-meson v_2 is zero. Therefore, a_2 has "meaning" outside of simply being used to correct $\Delta\rho\{\phi^*\}$ for a detector effect that is coupled to the ϕ-meson v_2. In general, there could be detector effects on $\Delta\rho\{\theta^*\}$ with ϕ-meson $v_2 = 0$. One easy example is the track $|\eta| < 1$ cut, which is independent of any v_2. Additionally, the $p_\perp$ efficiency can still cause a finite effect on a_2 and $\Delta\rho\{\theta^*\}$ when the ϕ-meson $v_2 = 0$ due to the loss of some kaon tracks and how this affects each kaon pair's boost to the pair rest frame in a non-trivial way.

This section describes several checks of the "data-driven" correction method with a MC toy model. The purpose is to check the key assumptions of the "data-driven" method: the detector effect on the real ϕ-meson is the same, or at least numerically close to, the detector effect on the combinatorial ϕ-meson. In addition, we also check how well the "Data Folding" and "Data Scaling" can reproduce the detector effect on the combinatorial ϕ-meson. The "Data Scaling" involves weighting kaons to have the same single particle 3-dimensional kinematics as those kaons coming from ϕ-meson decays and this weighting depends on bin size of the weighting histograms and essentially how well this weighting can really be done in 3D.

The purpose of the toy model is therefore to obtain three things: 1) the detector effect on Real ϕ-meson pairs, 2) the detector effect on the combinatorial ϕ-meson pairs (where one decay kaon is rotated by π in azimuth, and 3) the detector effect seen by Data Folding and Data Scaling, where background kaons are included and weighted to match decay kaons. In the ideal case, or in the assumption of the "data-driven" method these three are all equivalent or at least numerically similar. For clarity and reference these things are summarized below:

1) detector effect on the Real ϕ-meson,

2) detector effect on the Combinatorial ϕ-meson ("combinatorial ϕ-meson" is taken as an abbreviation for rotated K^+K^- pairs from ϕ-meson decays in the same event), and

3) detector effect seen by the data-driven method.

In the ideal case, all three of these things are identical.

For the current simulation, we generate ϕ-meson with $p_\perp$ spectra from 200 GeV published data in 40-50%, and use ϕ-meson $v_2 \sim 0.1 p_\perp$ with known EP angle, where $p_\perp$ is in unit of GeV/c. These ϕ-meson and their decay daughters are used to get 1), 2), and the Data Folding portion of 3). To get the Data Scaling portion of 3) we also need to generate background kaons from published data at 200 GeV in 40-50% using Boltzmann $p_\perp$ and a realistic v_2 of about $0.06p_\perp$. We then weight this kaons to have single particle kinematics identical to those in 1) and run a 2nd iteration applying this weight. For this weighting, we will statistically identify decay kaons from background kaons as described in Section 4.2.1, similar to real data analysis.

The detector effects included in this simulation are the single kaon $p_\perp$ efficiency for 40-50%[34]. Additionally, a kaon is cut if it has $p_\perp < 0.1$ GeV/c or $|\vec{p}| > 10$ GeV/c, to mimic the single kaon $p_\perp$ cut in data. For the acceptance, only decay kaons with $|\eta| < 1$ are kept. For background kaons used in 3), we only generate background kaons inside $|\eta| < 1$.

Here we collect some results from the simulation used to generate ϕ-meson with $1.2 < p_\perp < 5.4$ GeV/c with $\Delta\rho\{\theta^*\}= 0$, $a_2 = 0$, $v_2 = 0.1p_\perp$. For this simulation the EP resolution is considered to be perfect; we want to look at the detector effect seen by the Real ϕ-meson, combinatorial ϕ-meson, and Data Folding and Data Scaling without the EP resolution because the EP resolution correction can be done separately from detector effects and acceptance. Figure 4.24 shows the detector effect on Real ϕ-meson $\Delta\rho\{\theta^*\}$ and a_2 with $1.2 < p_\perp < 5.4$ GeV/c before and after detector effects; the $p_\perp$ averaged difference between the two corresponds to 1) the detector effect on the Real ϕ-meson. Figure 4.25 shows the input and reconstructed combinatorial ϕ-meson $\Delta\rho\{\theta^*\}$ and a_2 for 2), same-event decay daughters where one kaon is rotated by π, and 3) "Data-Folding" which is also made up of decay daughters and "Data-Scaling" which consists of weighted kaons that have suffered detector effects. Figure 4.26 is the detector effect for the combinatorial ϕ-meson 2) and the detector effect obtained from Data Folding minus Data Scaling 3). Here both methods agree quite well.

Figure 4.27 compares the detector effects for the Real ϕ-meson 1) with those obtained for the combinatorial ϕ-meson 2), and those obtained from the data-driven method 3). For the results of this check in Fig. 4.27, the decay kaon kinematics used to get the data-driven corrections for Rot/Mix pairs come from statistically identifying decay kaon kinematics as described in 4.2.1. As this is a simulation closure test, we can also weight by $\frac{\phi\ decay\ kaon}{all\ kaon}$ by tagging each track as being from a ϕ-meson decay or background, the results of which are shown in Fig. 4.28. The purpose of this is to gauge how well statistically identifying decay kaons works. Ideally, the "Data-Driven Rot." and "Data-Driven Mix." would agree

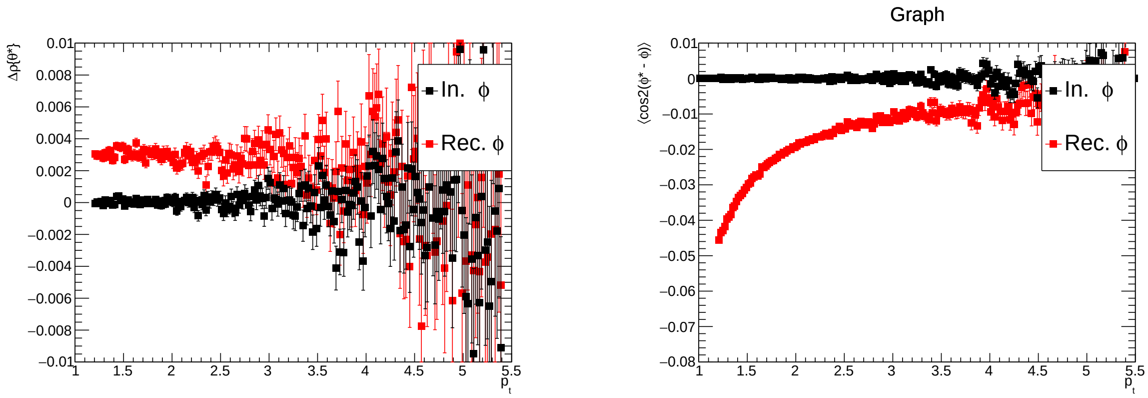

Figure 4.24. (Left) $\Delta\rho\{\theta^*\}$ vs. ϕ-meson $p_\perp$ for input (black) and reconstructed ϕ-mesons (red) where the reconstructed ϕ-mesons include only those decay kaons that survive the track η cut and $p_\perp$ efficiency. (Right) Same for a_2 vs. ϕ-meson $p_\perp$. These plots illustrate a realistic detector effect on a typical ϕ-meson $p_\perp$ bin used in an analysis.

with the "SE Rot ϕ" in Fig. 4.27; the statistical kinematic identification may be a source of the observed difference, as such an identification is not perfect.

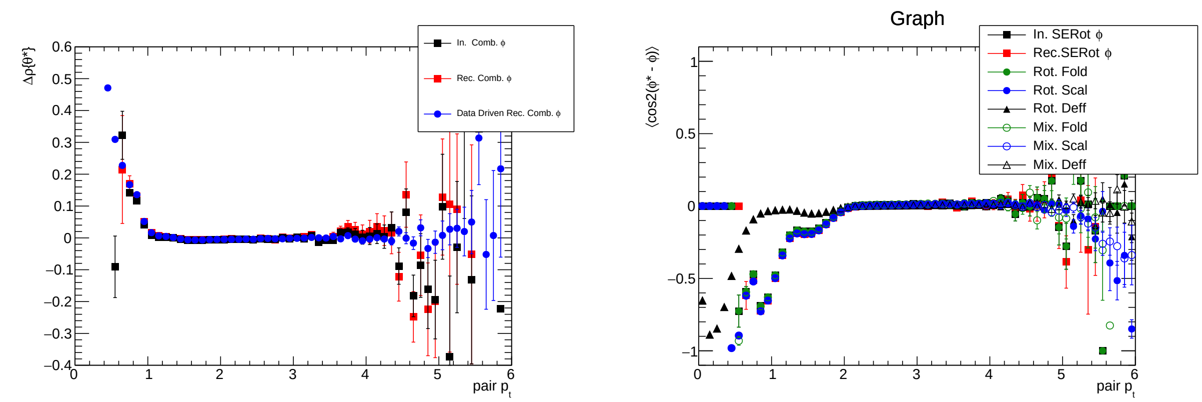

Figure 4.25. (Left) various combinatorial ϕ-meson $\Delta\rho\{\theta^*\}$ vs. pair $p_\perp$. (Right) various combinatorial a_2 vs. pair $p_\perp$. The series in each plot are as follows: black squares correspond to same-event, combinatorial, rotated decay daughters without detector effects; red squares are as same as black squares but with detector effects, the difference of which leads to 2); green circles correspond to Rot/Mix decay daughters without detector effects, and blue circles correspond to weighted kaons Rot/Mix with detector effects, the difference of which leads to 3); black triangles correspond to Rot/Mix background kaon pairs. All pairs in this plot are required to have pair mass within [1.015,1.025] to mimic real ϕ decays.

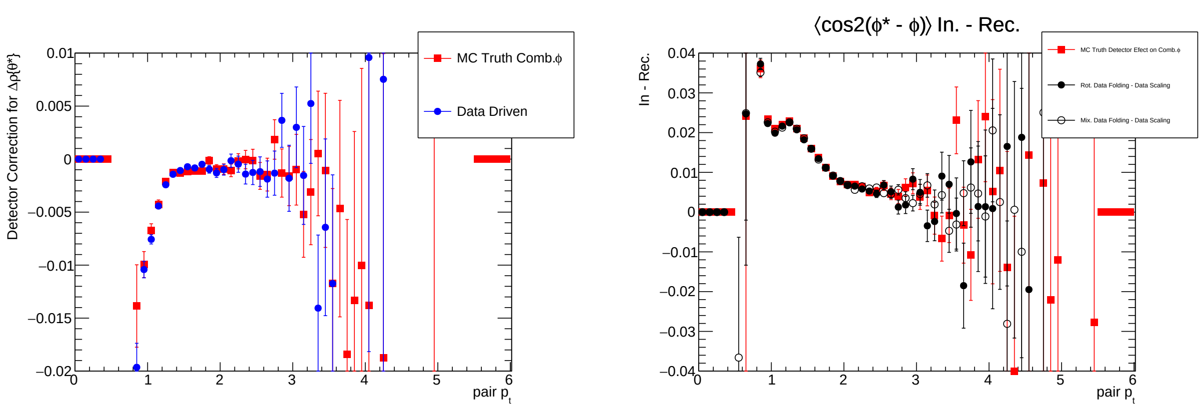

Figure 4.26. (Left) $\Delta\rho\{\theta^*\}$ Input - Reconstructed for combinatorial ϕ-meson in red squares, and for the data-driven method (Rot. filled, blue circles) vs. pair $p_\perp$. (Right) same for a_2, but (Rot. filled, black circles) and Mix (Open, black circles) . Here we can see that the Data-Driven correction approximates the detector effect on the combinatorial ϕ-meson quite well both in structure and $p_\perp$ average. Essentially, 2) and 3) agree reasonably well.

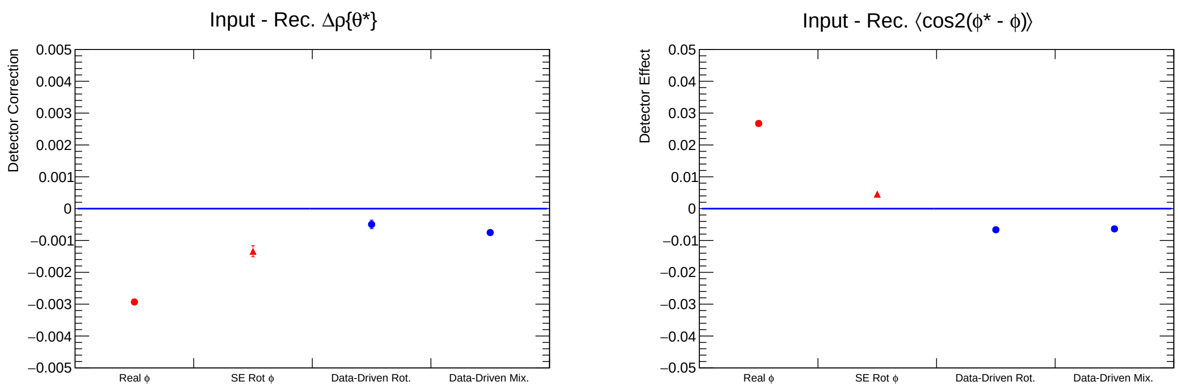

Figure 4.27. (Left) Input - Reconstructed for $\Delta\rho\{\theta^*\}$ for the Real ϕ-meson 1), Combinatorial Same Event (SE) Rot. ϕ-meson, and the Data Driven corrections from Rotated and Mixed events. (Right) same but for a_2. Here we can see that the detector effects for 1) differ from 2) and 3), although numerically the difference is reasonably small. In this plot, the "Data-Driven" points are obtained from statistically identifying decay kaon kinematics, rather than using MC tagging to identify decay kaon tracks.

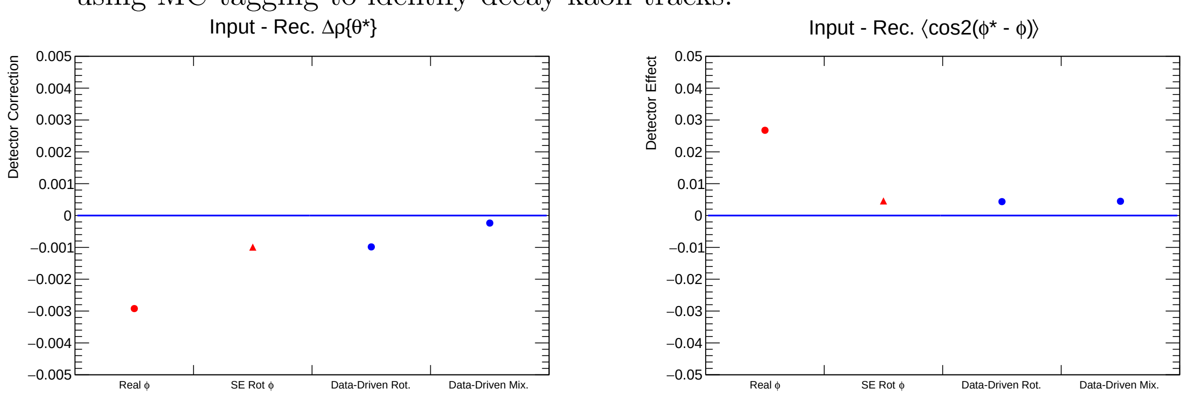

Figure 4.28. (Left) Input - Reconstructed for $\Delta\rho\{\theta^*\}$ for the Real ϕ-meson 1), Combinatorial Same Event (SE) Rot. ϕ-meson, and the Data Driven corrections from Rotated and Mixed events. (Right) Same but for a_2. Same as Fig. 4.27 except to get the two Data-Driven Corrections we weight by ϕ decay kaons over all kaons using tagged decay kaons in simulation. This result gives better agreement between "SE Rot ϕ" and "Data-Driven Rot." as they are now essentially the same.

4.3 Event Plane Resolution Correction

The reconstructed event plane has finite EP resolution. The EP resolution needs to be accounted for after all other detector effects are corrected. For θ^*, the EP resolution correction is given by [35]

$$\Delta\rho^{cor}\{\theta^*\} = \frac{4}{1+3R}\Delta\rho^{raw}\{\theta^*\}\,. \tag{4.14}$$

This correction is applied onto the measured raw spin alignment parameter, $\Delta\rho^{raw}\{\theta^*\}$, to obtain the corrected result $\Delta\rho^{cor}\{\theta^*\}$. In the case of ϕ^*, the resolution is given by [36]

$$\Delta\rho^{cor}\{\phi^*\} = \frac{1}{R}\Delta\rho^{raw}\{\phi^*\}\,. \tag{4.15}$$

In both Eq. 4.14 and Eq. 4.15, the “R” is the finite EP resolution defined in Ref. [37]. Experimentally, the 2nd-order EP resolution is determined using the sub-event method by

$$R^2 = \langle\cos 2\Delta\psi\rangle = \langle\cos 2(\psi - \psi')\rangle\,, \tag{4.16}$$

where ψ and ψ' are the East and West sub-event ψ_2.

In this thesis, the spin alignment corrected for finite EP resolution is labeled as the “Final” or “Fin” spin alignment number when compared with the raw (before any corrections), or “raw + cor” (raw, corrected for detector effects).

Detector effects, such as tracking resolutions, can also distort the shape of pair mass distributions and the observed raw spin alignment. This has been studied as part of my thesis work and documented in this preprint [38], submitted for publication. The effects are found to be small for the typical tracking resolutions in the STAR experiment.

4.4 Systematic Uncertainties

Systematic uncertainty typically refers to aspects of a measurement that we do not precisely know (precise knowledge of detector effects in the case of embedding) or somewhat "arbitrary" decisions in data analysis (fit ranges, analysis cuts).

One common prescription to asses systematic uncertainties is the Barlow Method [39] which defines a default case and variations to be compared with the default. For example, a default set of cuts may define particle identification in a given analysis, and these cuts are varied within acceptable ranges and the entire analysis is repeated. At the end the difference between a variation and a default is compared to the statistical uncertainty of the default, and if the difference is less than the statistical uncertainty of the default, then the Barlow procedure assigns zero systematic uncertainty from that source. If the difference is outside the statistical error of the default, then the square root of their quadratic difference is taken as an estimate of systematic uncertainty due to the variation. In the case of multiple variations of a given type, say multiple fit ranges or multiple polynomial background functions, typically the RMS of these variations is taken to be a 1σ estimate of the systematic uncertainty; 1σ is taken because the variations are within reasonable ranges corresponding to, say, 2/3 probability. In short, we estimate systematic uncertainties; we do not measure them, and the systematic uncertainty reflects some limitation in our understanding of the measurement beyond the standard statistical uncertainty.

The systematic uncertainties have been discussed throughout this thesis. Here, we give only an overall description of the systematic uncertainties in a single place. For details of the systematic uncertainty estimation the reader is referred to the relevant sections of this thesis.

For this thesis, we focus on systematic uncertainty from the raw $\Delta\rho\{\theta^*\}$, $\Delta\rho\{\phi^*\}$, v_2, a_2 extractions using the invariant mass method. We also considered systematic uncertainties in our detector correction method.

In a typical STAR analysis, we would vary the analysis track and event cuts, however this does require significant computing resources. So, we focus on systematics that are obtained by fitting a produced data set to numerically estimate a reasonable systematic uncertainty on the raw measurement, which are listed in Table 4.3.

In the case of our data-driven detector effect correction procedure, conceptually, the dominant systematic uncertainty is the ϕ-meson $v_2(p_\perp)$ in each centrality of Au+Au collisions at a given beam energy. In principle, this is also true for embedding. We assess this by using three common $v_2(p_\perp)$ parameterizations and obtaining the centrality dependence from the charged hadron v_2 data at a given energy. For this source we take the RMS of the two variations as 1σ.

As seen in Fig. 4.28, our data-driven correction does not necessarily reproduce the detector effect on real ϕ-meson and to cover this non-closure we add an additional global systematic uncertainty of 0.001. It is possible that this estimate could be improved in the future.

Table 4.3. Fitting Variations for Raw Signal from the Invariant Mass Method

Source	Default	Variations
Pair Mass Fit Range	[1.0,1.04]	[1.0,1.05], [1.0,1.06]
Pair Mass Bkg Function	Quadratic Poly2	Cubic Poly3
Pair Mass Mixed Event Subtraction	No	Yes

5. RESULTS

Figure 5.1 shows the global spin alignment for ϕ-meson as a function of beam energy from this study and compared with the published result by STAR in *Nature* [15]. Ignoring systematic uncertainties for the moment, we can see clear difference between this study and the publication at 200 GeV (our data are shifted for clarity). The 200 GeV Run 14 data, filled symbols, are all inconsistent with the publication and were a key factor in the decision for STAR to begin work on an erratum to the *Nature* publication. Generally, we see that our 200 GeV Run 11 data, open symbols, are consistent with the Run 14 200 GeV data, filled markers. We see consistent results for the raw signal and detector effect corrections between Run 11 and Run 14 (it is not required that the detector effects are the same between the two runs as the detector geometry changed, but it gives us confidence).

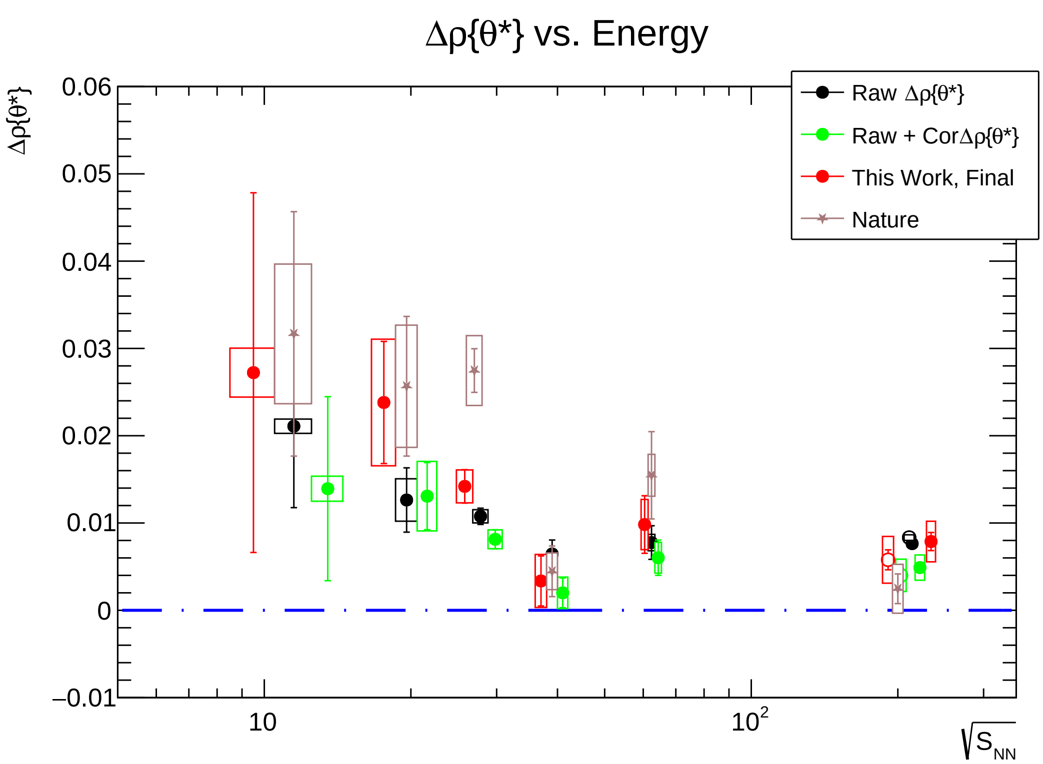

Figure 5.1. Measured raw $\Delta\rho\{\theta^*\}^{\mathrm{dir}}$ (black), detector effect "corrected" $\Delta\rho\{\theta^*\}$ by data-driven corrections (green), and the resolution corrected final $\Delta\rho\{\theta^*\}$ results (red) as functions of beam energy. 200 GeV Run 11 (open markers) and Run 14 are offset along the x axis for clarity; Run 11 left, Run 14 right. Shown in tan color are data published by STAR in *Nature* [15].

Furthermore in Fig. 5.1, we see a large difference around 27 GeV between our red final result and the published result in [15]. We do not exactly understand this difference as our data-driven correction method has its own limitations as discussed in 4.2.5. At the same time, the detector effect correction via embedding used in the publication is still under internal review by STAR. Note, the published data is the average of Run 11 and Run 18, but is largely dominated by Run 18, and our 27 GeV data point is from Run 18 only.

For the data points where this study is consistent with [15], we see that the embedding correction and data-driven corrections agree within their respective limitations.

Generally, we also point out that the publication and this analysis are analyzing the same data, therefore the error bars are correlated and this complicates some of the conclusions. However, we know for a fact that the 200 GeV raw Run 14 data cannot be reproduced by multiple groups in STAR, and it was concluded that the published 200 GeV data were wrong.

In terms of physics conclusions, our final results in Fig 5.1, filled red points, show a weaker beam energy dependence for ϕ-meson spin alignment when compared with [15], which may significantly affect the conclusion about the novel physics mechanism of color field fluctuations. Specifically, our raw, corrected, and final results at energies of 19.6 GeV and larger seem to indicate an energy independent spin alignment for ϕ-meson.

After internal comparison in STAR, prompted by this study, it was discovered, or made more obvious, that in the analysis of the *Nature* publication the raw data for 200 GeV from Run 14 and Run 11 were inconsistent. This can be seen in the comparison plot in the right panel of Fig. 5.2 from the Oct. 2024 STAR Collaboration Meeting, where our raw results clearly disagree with the published raw results from Run 14, but our results are generally consistent with the published results from Run 11.

This inconsistency is a problem as one would expect Au+Au collisions at the same beam energy done by the same experiment in different years to be consistent. These inconsistencies can be a sign of issues in the data analysis or raw data itself, and the precise reason for this discrepancy is not known.

Figure 5.3 shows the helicity-frame spin alignment $\Delta\rho_p\{\phi^*\}$ through the a_2 observable. The measured data a_2 (black points) is obtained by fitting a_2 (Eq. 4.13) vs. invariant mass analysis using signal-to-background ratio of ϕ-meson m_{inv} spectrum on top of a linear back-

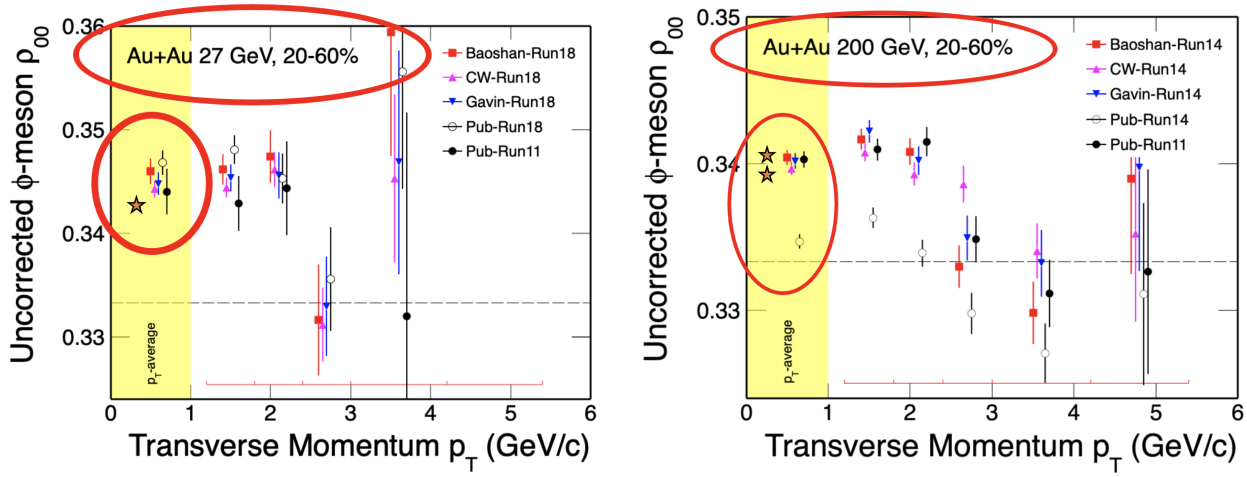

Figure 5.2. Comparisons of raw ϕ-meson global spin alignment results in STAR, prompted by this work, for 27 GeV Run 18 data (left panel) and 200 GeV Run 14 data (right panel). Note that no group can reproduce the open black points in the right panel which were used in the *Nature* publication [15]. The star symbols correspond to our raw invariant mass results, whereas the publication and other analyses involved in the comparison used the conventional yield method to extract the raw ρ_{00}.

ground, as described in Section 4.2.2. The detector effect $a_{2,\text{det}}$ (green points) is obtained by our data-driven method as described in Section 4.2.2. The difference (red points) is supposed to be the helicity-frame spin alignment $\Delta\rho_p\{\phi^*\} = -\frac{4}{3}(a_2 - a_{2,\text{det}})$. The $\Delta\rho_p\{\phi^*\}$ values are a few percent and are significant. As mentioned in Section 4.2.5 and Section 4.2.2, there are some complications due to the poor MC closure for a_2 from our data-driven detector correction method. However, these results show insight into possible helicity-frame spin alignment that may be improved in a further study.

Figure 5.4 shows the measured global spin alignment $\Delta\rho\{\phi^*\}$ (black points) and the "corrected" $\Delta\rho\{\phi^*\}$ (green points) by detector effect $-4a_{2,\text{det}}/3$ (from Fig. 5.3) via Eq. 4.12a as functions of beam energy. The results are further corrected by EP resolution of $1/R_{21}$. The Raw measurements are fairly energy independent, especially at energies higher than 27 GeV. This is also true for the final results and seems consistent with Fig. 5.1, even though the $\Delta\rho\{\phi^*\}$ correction is not perfect (does not cover all detector effects) as mentioned in

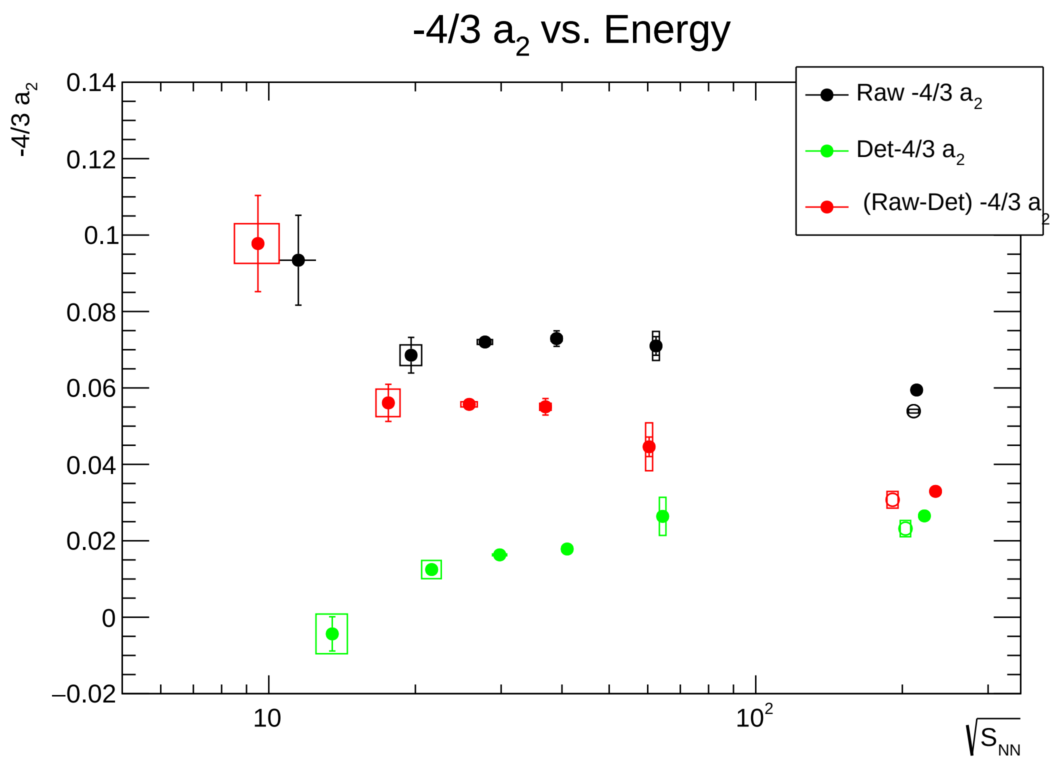

Figure 5.3. Raw a_2 (black), Detector $a_{2,\text{det}}$ (green), and (Raw − Detector) a_2 (red) vs. beam energy. All a_2 are scaled by $-4/3$. Data are 20-60% centrality Au+Au collisions, for $1.2 < p_{\perp,\text{pair}} < 5.4$ GeV/c. The open markers are from 200 GeV Run 14 data. While negligible in terms of the correction value, the data-driven correction use in this plot was obtained using comb. ϕ-meson with the same $p_{\perp,\text{pair}}$ cuts as the real ϕ-meson. Additionally, there are some complications from the poor MC Closure for the a_2 method.

Section 4.2.2. These results give a reasonable estimate for a more refined, future study correcting for all detector effects using either a data-driven method or embedding.

5.1 Additional Results

In this section we collect some additional results from this study, mainly the $p_{\perp,\text{pair}}$ dependent results for a_2 (Fig. 5.5), $\Delta\rho\{\phi^*\}$ (Fig. 5.7), and $\Delta\rho\{\theta^*\}$ (Fig. 5.6) using our data-driven correction method. These results are presented mainly as a sanity check of the energy dependent results, as we expect the a_2, $\Delta\rho\{\phi^*\}$, and $\Delta\rho\{\theta^*\}$ signal to all decrease with increasing $p_{\perp,\text{pair}}$, presumably because high $p_\perp$ particles are less coupled with the medium

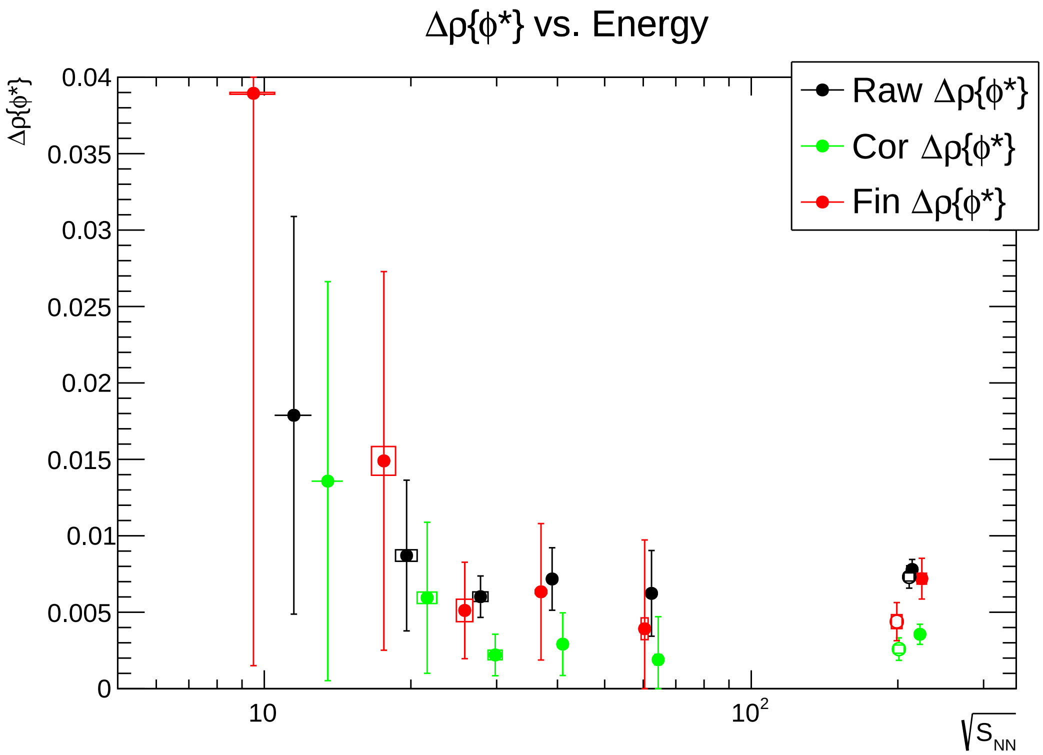

Figure 5.4. Measured raw $\Delta\rho\{\phi^*\}^{\mathrm{dir}}$ (black), detector effect "corrected" $\Delta\rho\{\phi^*\}$ (green, with $-\frac{4}{3}\ a_2v_2$ subtracted from the black points), and the resolution corrected final $\Delta\rho\{\phi^*\}$ results (red) as functions of beam energy. Run 11 (open markers) and Run 14 at 200 GeV are offset along the x axis for clarity. Note, in this plot the correction is using the raw data a_2v_2, which only approximates the detector effect on $\Delta\rho\{\phi^*\}$.

and therefore their spins are less aligned with the OAM or the vector meson momentum direction.

In general, these results provide guidance for more refined studies vs. $p_{\perp,\mathrm{pair}}$ as these results cut on combinatorial ϕ-meson $p_\perp$ to obtain a correction for the true ϕ-meson $p_\perp$, unlike the most correct results in Fig. 5.1. In principle, this technicality can be fixed, but requires significant re-running of the Data Scaling and Data Folding. From our experience, this detail is not likely to affect the results, but we point it out for clarity.

As a reminder, the idea is that the average of all the combinatorial ϕ-meson (kaon pairs in the same event where one kaon is rotated) obtained from ϕ-meson in a given $p_\perp$ range contains the detector effect on the real ϕ-meson. Essentially, the detector effect on the true ϕ-mesonis smeared out in the combinatorial ϕ-meson and by including all of them, we recover this true detector effect on the real ϕ-meson. For example to obtain the correction for Fig. 5.1, we obtain Data Scaling weights for kaon pairs with $1.2 < p_{\perp,\text{pair}} < 5.4$ GeV/c and Data Folding from ϕ-meson generated with $1.2 < p_{\perp,\text{pair}} < 5.4$ GeV/c. Then, we apply no $p_{\perp,\text{pair}}$ cut to the pairs with Data Scaling weights applied, and we apply no $p_{\perp,\text{pair}}$ cut on the decay kaon pairs from Data Folding. This means that for a $p_\perp$ dependent analysis we would need to re-run Data Folding and Data Scaling for each ϕ-meson $p_\perp$ bin at a given energy. This requires running STAR data two times for each ϕ-meson $p_\perp$ bin; once to obtain the weights and once to apply them for each $p_\perp$ bin. Additionally, the Data Folding has to be run for each ϕ-meson $p_\perp$ bin.

In these Fig 5.5, 5.6, 5.7, we did cut on the combinatorial ϕ-meson to be the same as the real ϕ-meson $p_{\perp,\text{pair}}$ which is not ideal, however we see essentially no difference in the detector effect with or without this cut. We just point out this detail for clarity and to say that these results explore the a_2, $\Delta\rho\{\phi^*\}$, $\Delta\rho\{\theta^*\}$ variables in a new way. Also as mentioned previously, in the case $\Delta\rho\{\phi^*\}$ we do not use the Data Scaling and Data Folding correction method, rather we use the a_2-v_2 method as described in Section 4.2.2 which may not cover all detector effects on the $\Delta\rho\{\phi^*\}$ variable. However, we would argue the remaining detector effects are small as the $\Delta\rho\{\theta^*\}$ and $\Delta\rho\{\phi^*\}$ results generally agree in Fig 5.1 and Fig. 5.4.

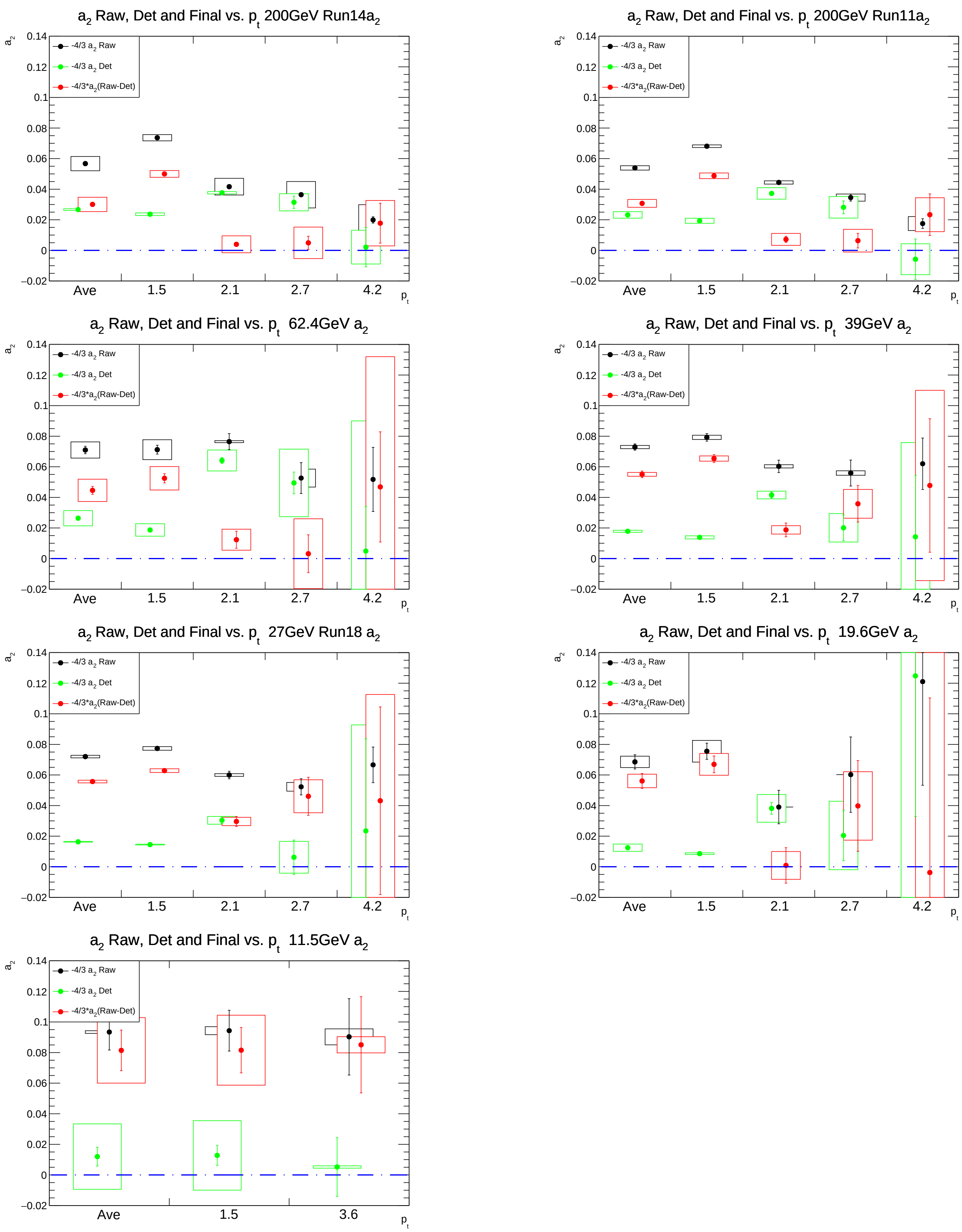

Figure 5.5. The a_2 results vs. $p_\perp$ for Raw, Det, and Raw − Det a_2 in Au+Au centrality 20-60% collisions for the various runs/energies.

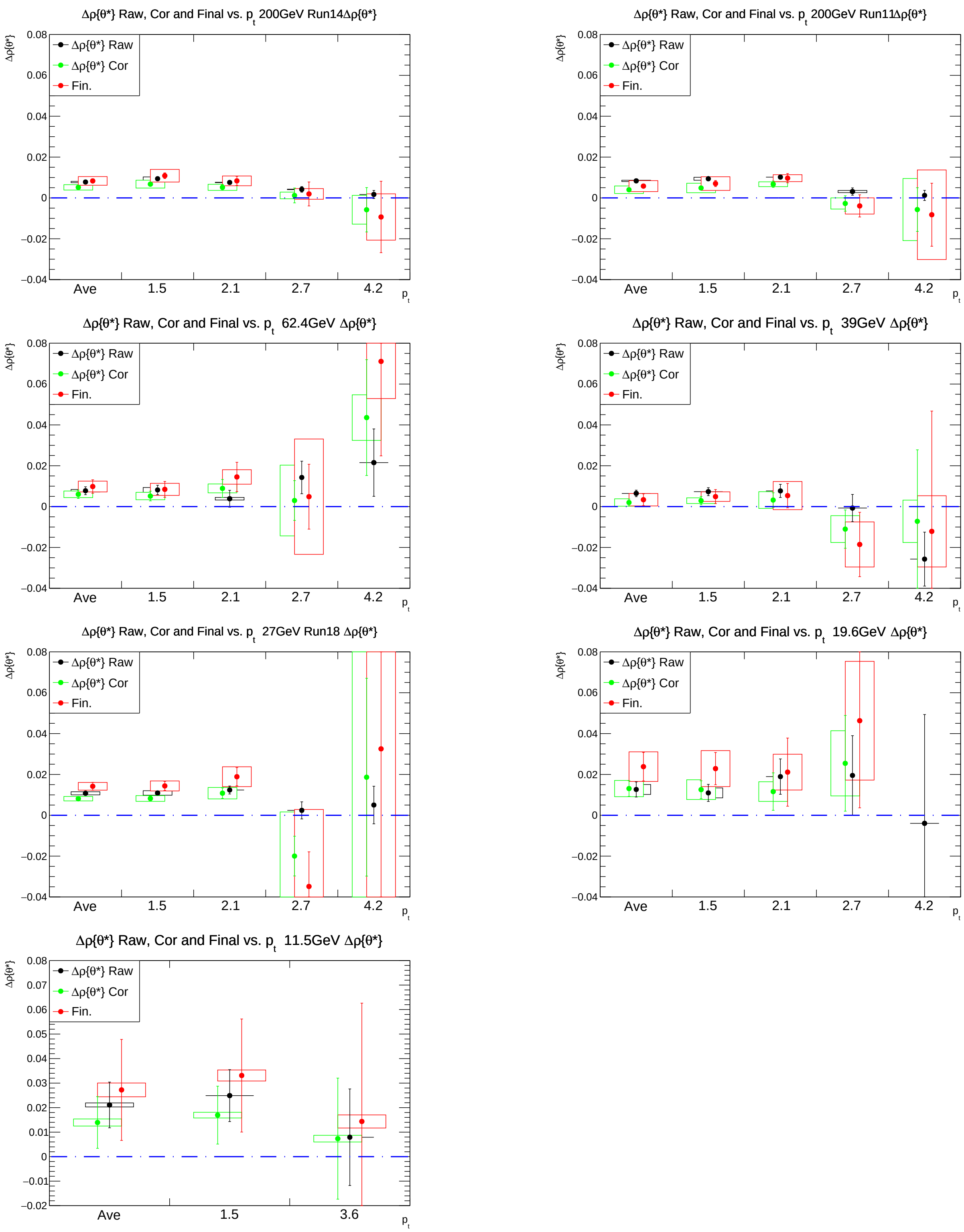

Figure 5.6. The $\Delta\rho\{\theta^*\}$ results vs. $p_\perp$ for Raw, Cor, and Fin (Raw + Cor) with EP Resolution correction in Au+Au centrality 20-60% collisions for the various runs/energies.

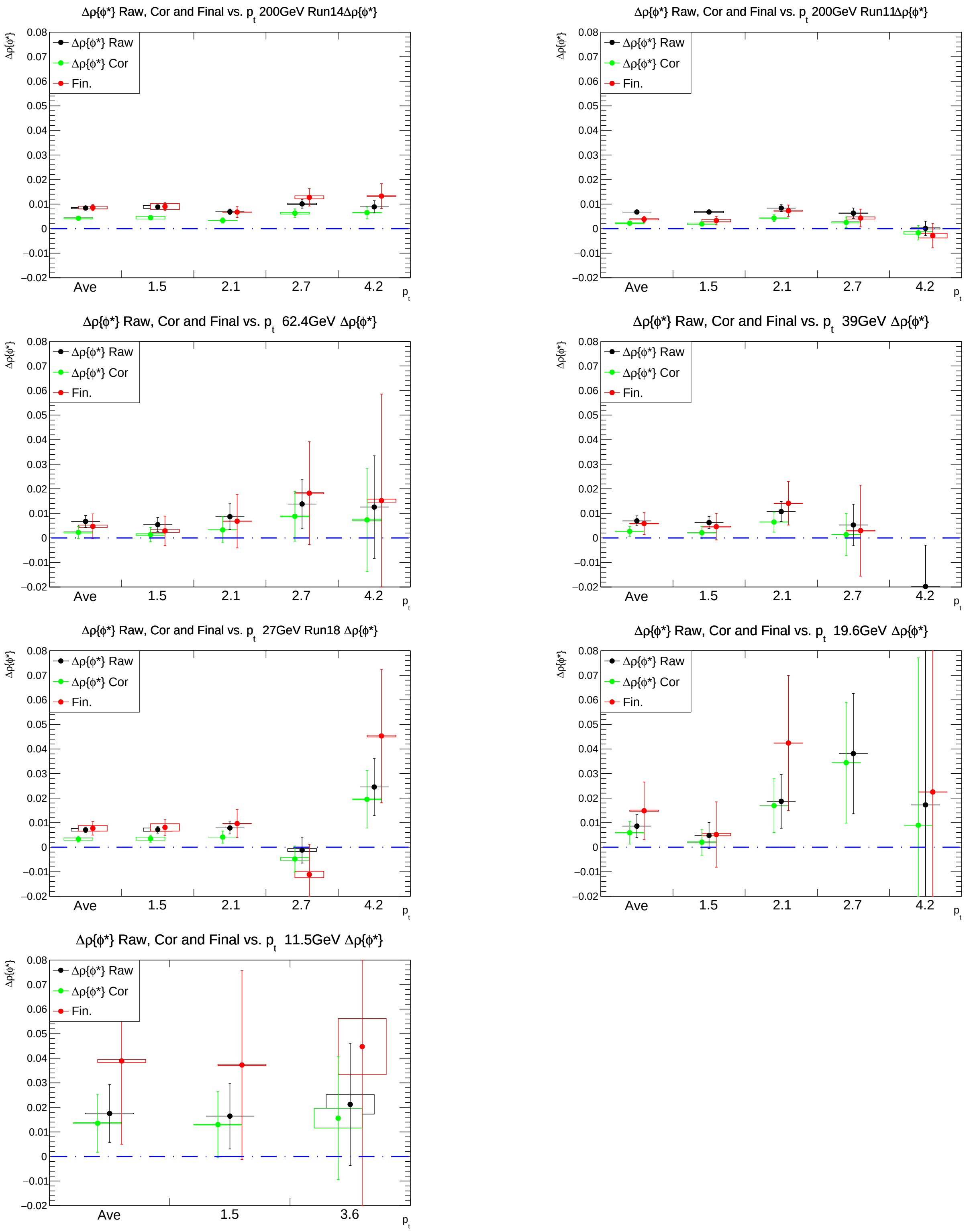

Figure 5.7. $\Delta\rho\{\phi^*\}$ results vs. $p_\perp$ for Raw, Cor, and Fin (Raw + Cor) with EP Resolution correction in Au+Au centrality 20-60% collisions for the various runs/energies.

6. SUMMARY

Global spin alignment of ϕ-meson is a hot topic in relativistic heavy-ion collisions and may provide unique insight into the QGP and hadronization. This study examined and attempted to reproduce a publication in *Nature* by STAR in January 2023 [15] reporting significant global spin alignment of ϕ-meson with significant beam-energy dependence, while exploring new methods for signal extraction and corrections for detector effects.

This analysis could not reproduce the published STAR result in Ref. [15] early on, and it became clear to us by the time of the Quark Matter (QM) Conference in Houston in September 2023 that the published data was not reproducible.

This thesis developed a new method to extract the raw signal of the ϕ-meson spin alignment parameter ρ_{00}, called the invariant mass method as discussed in Section 4.1.2, which looks at the $\Delta\rho\{\theta^*\}$ signal vs. kaon pair invariant mass (m_{inv}). We also investigated the ϕ^* method in Section 4.1.3 suggested by Dr. Sergei Voloshin to extract the ϕ-meson ρ_{00}, which is a different observable with different kinematic dependence than the conventional θ^* method. Lastly we explored the a_2 variable which quantifies detector effects for the ϕ^* method as discussed in Section 4.2.2 but may also be related to possible helicity frame spin alignment.

For the raw $\Delta\rho\{\theta^*\}$, $\Delta\rho\{\phi^*\}$, and a_2 variables we developed data-driven methods to correct for detector effects arising from finite acceptance and efficiencies. The motivation for this is three-folds: (i) standard corrections using MC to simulate detector effects may not be reliable because two-particle effects may not be faithfully simulated, (ii) the detector effects have to be parameterized in terms of not only particle kinematics but also the decay topology because the spin alignment signal is extracted from the angular distribution of the decay kaons in the rest frame of the ϕ meson, and (iii) small errors in the embedding efficiency and detector acceptance can cause large relative error in the spin alignment result when the raw signal is on the order of 1% (~ 0.008 at 200 GeV, for example).

Our data-driven detector correction method is based on the following idea: The detector effect on the real ϕ-meson should be approximately equal to the average detector effect seen by kaon pairs with similar kinematics and pair mass. Essentially, the detector should not see any difference between kaon pairs from ϕ-meson decays and pairs of two primordial kaons (or one primordial kaon and one decay daughter) if their kinematics are the same. We do require that these "combinatorial" kaon pairs have similar pair mass to that of the real ϕ-meson so that the "decay topology" of this combinatorial kaon pair looks similar in its own rest frame to the decay of a real ϕ-meson. We sometimes refer to these combinatorial kaon pairs within the ϕ-meson mass region as "combinatorial/pseudo ϕ mesons."

To get detector correction, we scale (i.e. weight) all measured kaons in real data to have the same single particle kinematic distributions ($p_\perp$,η, $\phi-\psi_2$) as those from ϕ-meson decays. The kinematic distributions of ϕ-decay kaons are reconstructed statistically from real data. From the scaled kaons we form combinatorial pairs (pairs of K^+ and K^- in the same event where K^- is rotated by π in azimuth to destroy real ϕ-meson signal, or by the mixed-event technique) as described in "Data Scaling", Section 4.2.1. When we form pairs of these scaled kaons and then cut on their pair mass to be within $m_{\rm inv} = [1.015, 1.025]$ GeV/c, these combinatorial/pseudo "ϕ mesons" should be as similar to the real ϕ-meson as possible for the purposes of seeing a detector effect. Since we perform this procedure using real data, whatever detector effects (such as finite detector acceptance and imperfect performance) in real data are captured by these scaled kaon pairs.

Next, we use a standalone toy model to generate ϕ mesons according to published $p_\perp$ spectra and $v_2(p_\perp)$ and decay these ϕ mesons into kaons. We then form combinatorial kaon pairs from these ϕ-meson decays (by rotating the K^- by π in azimuth or by the mixed-event technique) and cut on their $m_{\rm inv}$ to be in the same range [1.015,1.025] GeV/c. These combinatorial/pseudo "ϕ-meson" kaon pairs do not have any effect from detector performance and we do not apply any cuts on the decay kaons (no acceptance effect). The details of this method are described in "Data Folding" 4.2.1.

The difference between these two combinatorial/pseudo "ϕ-meson" kaon pair samples in Data Scaling and Data Folding is the detector effects. There is a minor complication in this correction method when we compare pairs of kaons from Data Scaling and Data Folding, we do not want to cut on any other quantity of these pairs, besides the pair mass, which is a bit counterintuitive. The idea is that the difference between the combinatorial pairs from Data Scaling and from Data Folding will reproduce the detector effects on the real ϕ mesons on average. And here "average" means including pairs of any $p_\perp$ and any y. Basically, the detector effects on a real ϕ-meson are smeared out in all the combinatorial pairs, and therefore all the pairs should be used in deriving the correction for detector effects. Our toy model MC closure test indicates that the Data Scaling "combinatorial ϕ mesons" do capture the detector effects suffered by the Data Folding "combinatorial ϕ mesons."

There is an additional wrinkle in the sense that the detector effects on the real ϕ-meson may be different from the average we obtain from Data Folding and Data Scaling. In other words, it is possible that the real ϕ-meson decays see different detector effects than a combinatorial/pseudo "ϕ meson," i.e. a pair of kaons with the same single-particle kinematic distributions and pair mass. This issue is explored in our toy model closure test in Section 4.2.5, and here we do seem to see a difference in the detector effects on $\Delta\rho(\theta^*)$ between the real ϕ-meson and combinatorial ϕ-meson, on the order of 0.002 for the studied ϕ-meson kinematic range of $1.2 < p_\perp < 5.4$ GeV/c. For the purposes of this thesis, we use the difference to estimate the systematic uncertainty on the detector correction method. However, this difference is not fully understood and may warrant further study.

The main result of this work is Fig. 5.1 which is the ϕ-meson spin alignment parameter $\Delta\rho(\theta^*) \equiv \rho_{00} - 1/3$ from this study vs. beam energy compared with the result from the *Nature* publication [15]. Here, the new results are from our newly developed invariant mass method for raw signal extraction and are using the detector corrections from our data-driven method. We see weaker energy dependence at 19.6 GeV and above, which may have significant impact on the physics conclusion about the strong field fluctuations. We also revise the 200 GeV data to be about $\sim$0.008 which contradicts the published result of nearly 0 in the *Nature* publication [15]. The 200 GeV data point is particularly important as it is one of the five data points used in the theoretical model fit in the *Nature* publication, and the measurement of $\sim$0.008 is more consistent with results from 27 GeV, 39 GeV, and 62.4 GeV, therefore weakening the energy dependence.

This study also provides guidance for future spin alignment studies including searches for spin alignment in the ϕ-meson helicity frame, spin alignment with different kinematic variables such as ϕ^*, and investigations in other ways to parameterize and account for detector effects in spin alignment studies.

REFERENCES

1. Wikipedia contributor. *Standard Model — Wikipedia, The Free Encyclopedia* [Online; accessed 20-October-2023]. 2023.

   .

2. Aad, G. *et al.* Observation of a new particle in the search for the Standard Model Higgs boson with the ATLAS detector at the LHC. *Phys. Lett. B* **716,** 1–29. arXiv: 1207.7214 [hep-ex] (2012).

3. Chatrchyan, S. *et al.* Observation of a New Boson at a Mass of 125 GeV with the CMS Experiment at the LHC. *Phys. Lett. B* **716,** 30–61. arXiv: 1207.7235 [hep-ex] (2012).

4. Gross, D. J. & Wilczek, F. Ultraviolet Behavior of Nonabelian Gauge Theories. *Phys. Rev. Lett.* **30** (ed Taylor, J. C.) 1343–1346 (1973).

5. Politzer, H. D. Reliable Perturbative Results for Strong Interactions? *Phys. Rev. Lett.* **30** (ed Taylor, J. C.) 1346–1349 (1973).

6. Adams, J. *et al.* Experimental and theoretical challenges in the search for the quark gluon plasma: The STAR Collaboration's critical assessment of the evidence from RHIC collisions. *Nucl.Phys.* **A757,** 102–183. arXiv: nucl-ex/0501009 [nucl-ex] (2005).

7. Adcox, K. *et al.* Formation of dense partonic matter in relativistic nucleus-nucleus collisions at RHIC: Experimental evaluation by the PHENIX collaboration. *Nucl.Phys.* **A757,** 184–283. arXiv: nucl-ex/0410003 [nucl-ex] (2005).

8. Muller, B., Schukraft, J. & Wyslouch, B. First Results from Pb+Pb collisions at the LHC. *Ann.Rev.Nucl.Part.Sci.* **62,** 361–386. arXiv: 1202.3233 [hep-ex] (2012).

9. Liang, Z.-T. & Wang, X.-N. Globally polarized quark-gluon plasma in non-central A+A collisions. *Phys. Rev. Lett.* **94.** [Erratum: Phys. Rev. Lett.96,039901(2006)], 102301. arXiv: nucl-th/0410079 [nucl-th] (2005).

10. Voloshin, S. A. Polarized secondary particles in unpolarized high energy hadron-hadron collisions? arXiv: nucl-th/0410089 (Oct. 2004).

11. Wu, H.-Z., Pang, L.-G., Huang, X.-G. & Wang, Q. Local spin polarization in high energy heavy ion collisions. *Phys. Rev. Research.* **1,** 033058. arXiv: 1906.09385 [nucl-th] (2019).

12. Becattini, F. & Lisa, M. A. Polarization and Vorticity in the Quark–Gluon Plasma. *Ann. Rev. Nucl. Part. Sci.* **70,** 395–423. arXiv: 2003.03640 [nucl-ex] (2020).

13. Sheng, X.-L., Oliva, L. & Wang, Q. What can we learn from the global spin alignment of ϕ mesons in heavy-ion collisions? *Phys. Rev. D* **101.** [Erratum: Phys.Rev.D 105, 099903 (2022)], 096005. arXiv: 1910.13684 [nucl-th] (2020).

14. Adamczyk, L. *et al.* Global Λ hyperon polarization in nuclear collisions: evidence for the most vortical fluid. *Nature* **548,** 62–65. arXiv: 1701.06657 [nucl-ex] (2017).

15. Abdallah, M. S. *et al.* Pattern of global spin alignment of ϕ and K^{*0} mesons in heavy-ion collisions. *Nature* **614,** 244–248. arXiv: 2204.02302 [hep-ph] (2023).

16. Sheng, X.-L., Oliva, L., Liang, Z.-T., Wang, Q. & Wang, X.-N. Spin Alignment of Vector Mesons in Heavy-Ion Collisions. *Phys. Rev. Lett.* **131,** 042304. arXiv: 2205.15689 [nucl-th] (2023).

17. Acharya, S. *et al.* Evidence of Spin-Orbital Angular Momentum Interactions in Relativistic Heavy-Ion Collisions. *Phys. Rev. Lett.* **125,** 012301. arXiv: 1910.14408 [nucl-ex] (2020).

18. Brookhaven National Lab Flickr. Aerial View of RHIC. [Online; accessed 25-March-2025]. https://www.flickr.com/photos/brookhavenlab/7979381212/in/album-72157613690851651 (2025).

19. Collaboration, S. STAR Detector. [Online; accessed 2-April-2025]. https://www.star.bnl.gov/central/experiment/ (2025).

20. Anderson, M. *et al.* The Star time projection chamber: A Unique tool for studying high multiplicity events at RHIC. *Nucl.Instrum.Meth.* **A499,** 659–678. arXiv: nucl-ex/0301015 [nucl-ex] (2003).

21. Llope, W., Geurts, F., Mitchell, J., Liu, Z., Adams, N., *et al.* The TOFp / pVPD time-of-flight system for STAR. *Nucl.Instrum.Meth.* **A522,** 252–273. arXiv: nucl-ex/0308022 [nucl-ex] (2004).

22. Poskanzer, A. M. & Voloshin, S. Methods for analyzing anisotropic flow in relativistic nuclear collisions. *Phys.Rev.* **C58,** 1671–1678. arXiv: nucl-ex/9805001 [nucl-ex] (1998).

23. Abelev, B. I. *et al.* Centrality dependence of charged hadron and strange hadron elliptic flow from s(NN)**(1/2) = 200-GeV Au + Au collisions. *Phys. Rev. C* **77,** 054901. arXiv: 0801.3466 [nucl-ex] (2008).

24. Voloshin, S. https://drupal.star.bnl.gov/STAR/system/files/202403-SpinAlgnAcceptance-6.pdf.

25. Abelev, B. I. *et al.* Partonic flow and phi-meson production in Au + Au collisions at s(NN)**(1/2) = 200-GeV. *Phys. Rev. Lett.* **99,** 112301. arXiv: nucl-ex/0703033 (2007).

26. Adamczyk, L. *et al.* Centrality and transverse momentum dependence of elliptic flow of multistrange hadrons and ϕ meson in Au+Au collisions at $\sqrt{s_{NN}}$ = 200 GeV. *Phys. Rev. Lett.* **116,** 062301. arXiv: 1507.05247 [nucl-ex] (2016).

27. Abelev, B. I. *et al.* Measurements of phi meson production in relativistic heavy-ion collisions at RHIC. *Phys. Rev. C* **79,** 064903. arXiv: 0809.4737 [nucl-ex] (2009).

28. Adams, J. *et al.* Azimuthal anisotropy in Au+Au collisions at s(NN)**(1/2) = 200-GeV. *Phys. Rev. C* **72,** 014904. arXiv: nucl-ex/0409033 (2005).

29. Adamczyk, L. *et al.* Probing parton dynamics of QCD matter with Ω and ϕ production. *Phys. Rev. C* **93,** 021903. arXiv: 1506.07605 [nucl-ex] (2016).

30. Adamczyk, L. *et al.* Elliptic flow of identified hadrons in Au+Au collisions at $\sqrt{s_{NN}}$ = 7.7-62.4 GeV. *Phys. Rev. C* **88,** 014902. arXiv: 1301.2348 [nucl-ex] (2013).

31. Hayrapetyan, A. *et al.* Elliptic anisotropy measurement of the $f_0(980)$ hadron in proton-lead collisions and evidence for its quark-antiquark composition. arXiv: 2312.17092 [nucl-ex] (Dec. 2023).

32. Dong, X., Esumi, S., Sorensen, P., Xu, N. & Xu, Z. Resonance decay effects on anisotropy parameters. *Phys. Lett. B* **597,** 328–332. arXiv: nucl-th/0403030 (2004).

33. Wang, F. & Zhao, J. Challenges in flow background removal in search for the chiral magnetic effect. *Phys. Rev. C* **95,** 051901. arXiv: 1608.06610 [nucl-th] (2017).

34. Abelev, B. I. *et al.* Systematic Measurements of Identified Particle Spectra in pp, d^+ Au and Au+Au Collisions from STAR. *Phys. Rev. C* **79,** 034909. arXiv: 0808.2041 [nucl-ex] (2009).

35. Tang, A. H., Tu, B. & Zhou, C. S. Practical considerations for measuring global spin alignment of vector mesons in relativistic heavy ion collisions. *Physical Review C* **98.** ISSN: 2469-9993. http://dx.doi.org/10.1103/PhysRevC.98.044907 (Oct. 2018).

36. Niida, T. & Voloshin, S. A. Polarization phenomenon in heavy-ion collisions. *International Journal of Modern Physics E* **33.** ISSN: 1793-6608. http://dx.doi.org/10.1142/S0218301324300108 (Aug. 2024).

37. Poskanzer, A. M. & Voloshin, S. A. Methods for analyzing anisotropic flow in relativistic nuclear collisions. *Phys. Rev. C* **58,** 1671–1678. https://link.aps.org/doi/10.1103/PhysRevC.58.1671 (3 Sept. 1998).

38. Robertson, C. W., Feng, Y. & Wang, F. *Impact of Tracking Resolutions on ϕ-Meson Spin Alignment Measurement* 2025. arXiv: 2502.06576 [physics.data-an]. https://arxiv.org/abs/2502.06576.

39. Barlow, R. *Systematic errors: Facts and fictions* in *Conference on Advanced Statistical Techniques in Particle Physics* (July 2002), 134–144. arXiv: hep-ex/0207026.

A. SYSTEMATIC PLOTS

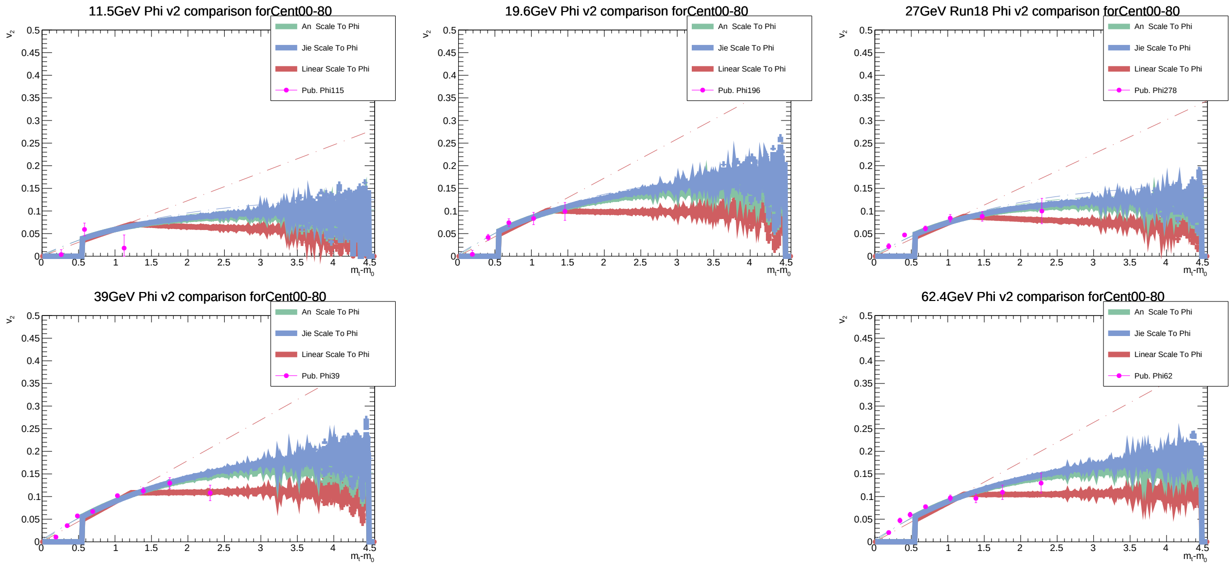

Figure A.1. The v_2 parameterizations for published ϕ data in pink for energies below 200 GeV. Thick lines are generated v_2 with statistical error bars, according to the three parameterizations Eqs. 4.8, 4.9, and 4.10.

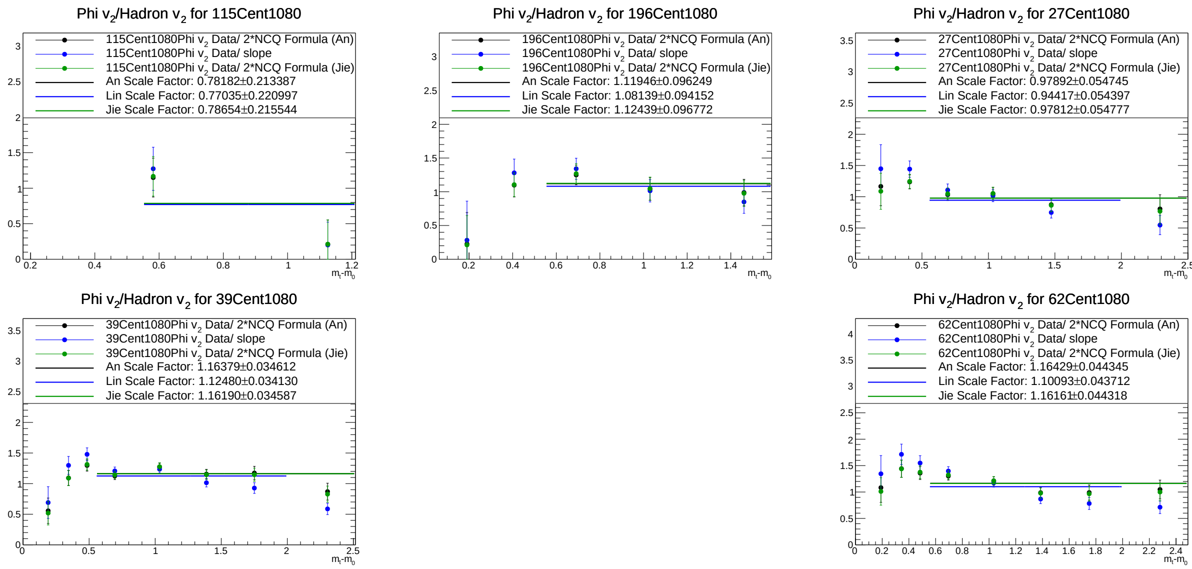

Figure A.2. Ratio of published ϕ-meson v_2 over charged hadron v_2 parameterizations for energies/runs below 200 GeV. These scaling factors make the average charged hadron v_2 equal to the ϕ-meson v_2 and allow us to use the charged hadron v_2 centrality dependence for the ϕ-meson v_2, since we do not have centrality differential measurements for ϕ.

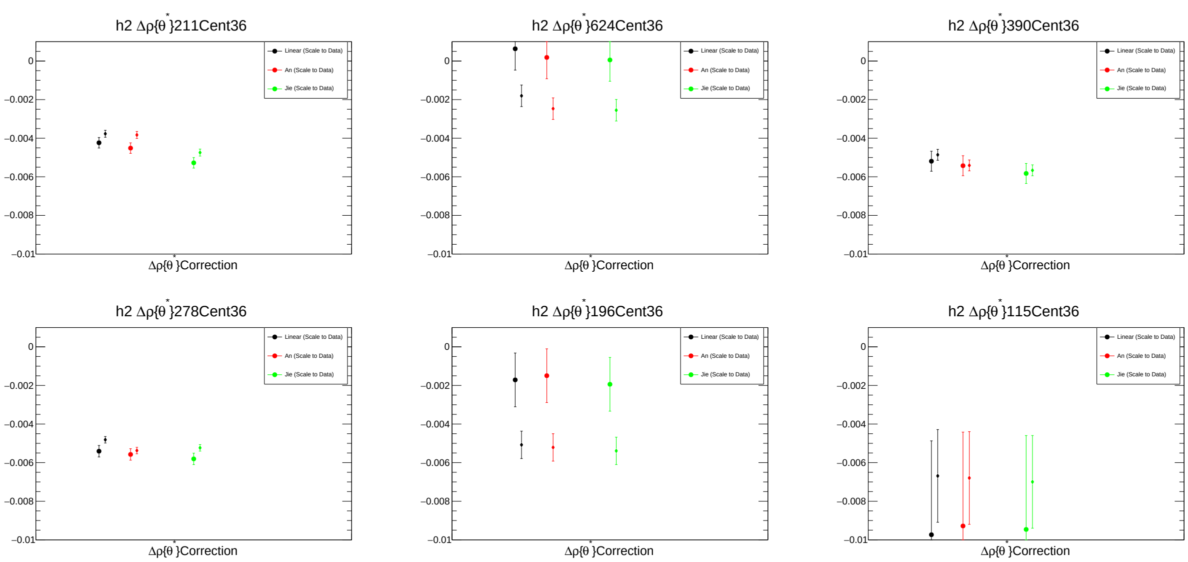

Figure A.3. Systematics of the data-driven $\Delta\rho\{\theta^*\}$ correction for the Rotated (circle) and Mixed (diamonds) pair correction methods for different v_2 parameterizations. These are in Au+Au 20-60% centrality for all energies for ϕ-meson $1.2 < p_\perp < 5.4$ GeV/c.

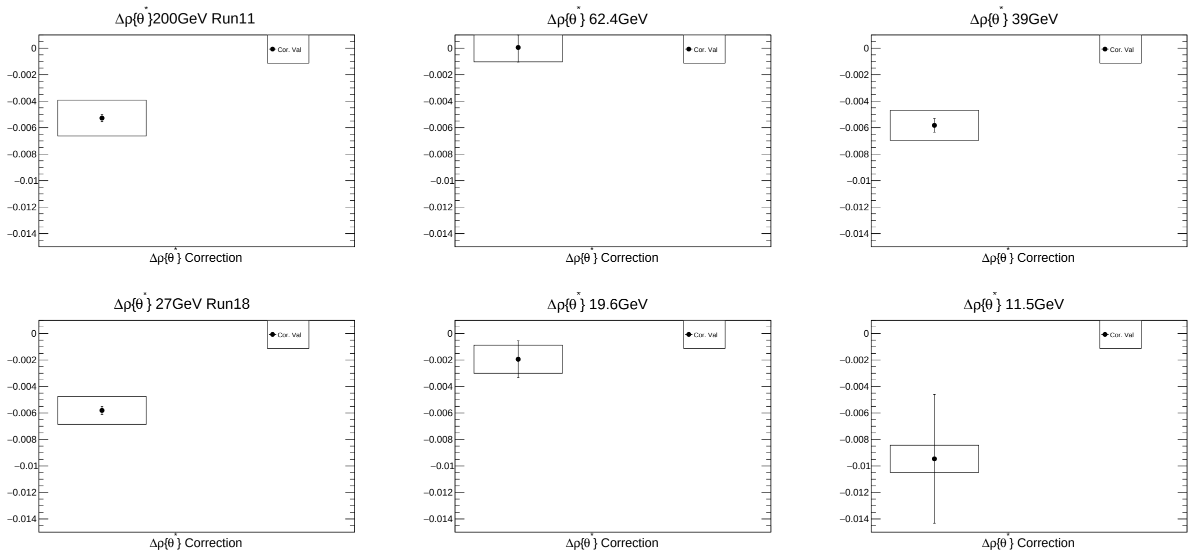

Figure A.4. Barlow Systematic uncertainties from the variations in Fig. 4.14 using "Jie" "Rotated" as the default. Two main sources of systematics: ϕ-meson v_2 uncertainty and rotated pairs vs. mixed event pairs. We use the RMS of the two v_2 parameterizations for the systematic uncertainty from the former, and add an additional overall 0.001 from the MC-nonclosure. The total systematic uncertainty is the quadratic sum of the two sources. These are in Au+Au 20-60% centrality for ϕ-meson $1.2 < p_{\perp} < 5.4$ GeV/c.

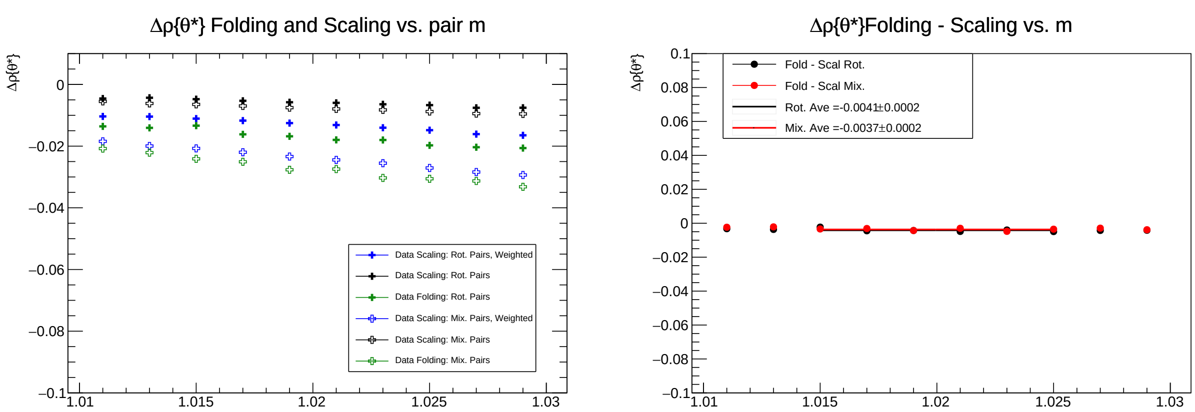

Figure A.5. Corrections from Folding minus Scaling in the ϕ-meson mass window for 200 GeV Run 11

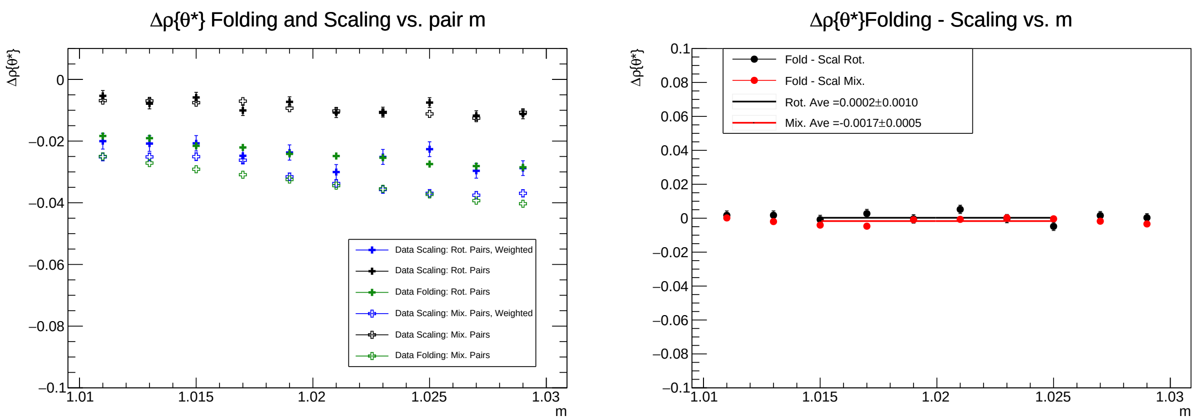

Figure A.6. Corrections from Folding minus Scaling in the ϕ-meson mass window for 62.4 GeV

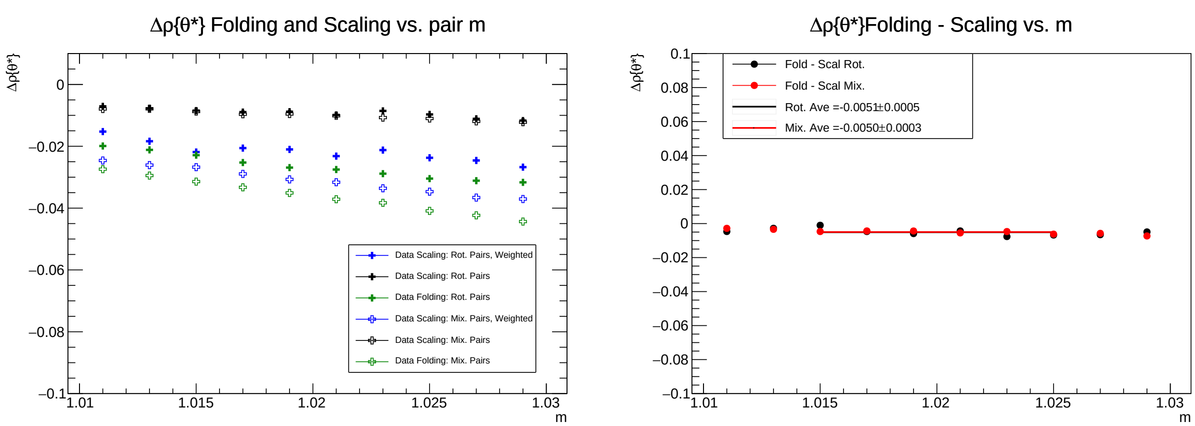

Figure A.7. Corrections from Folding minus Scaling in the ϕ-meson mass window for 39 GeV

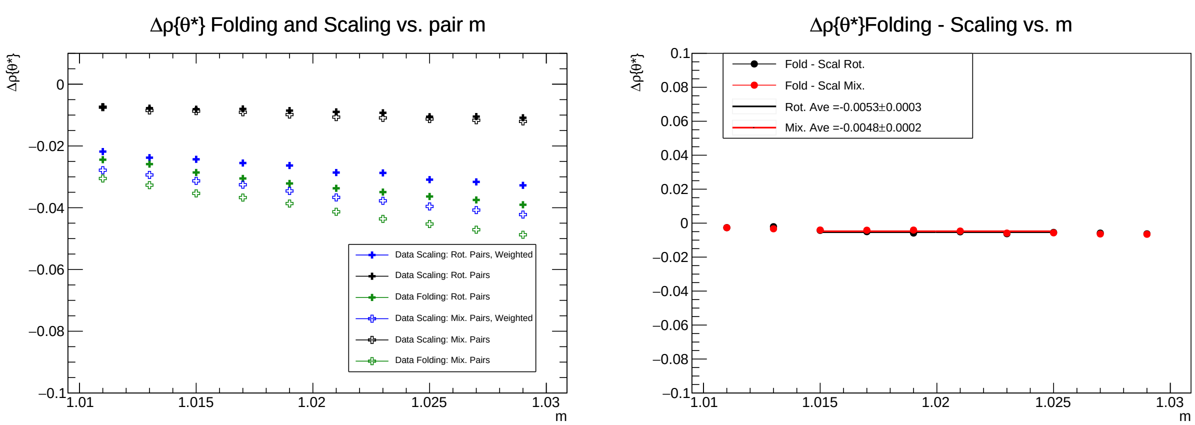

Figure A.8. Corrections from Folding minus Scaling in the ϕ-meson mass window for 27 GeV

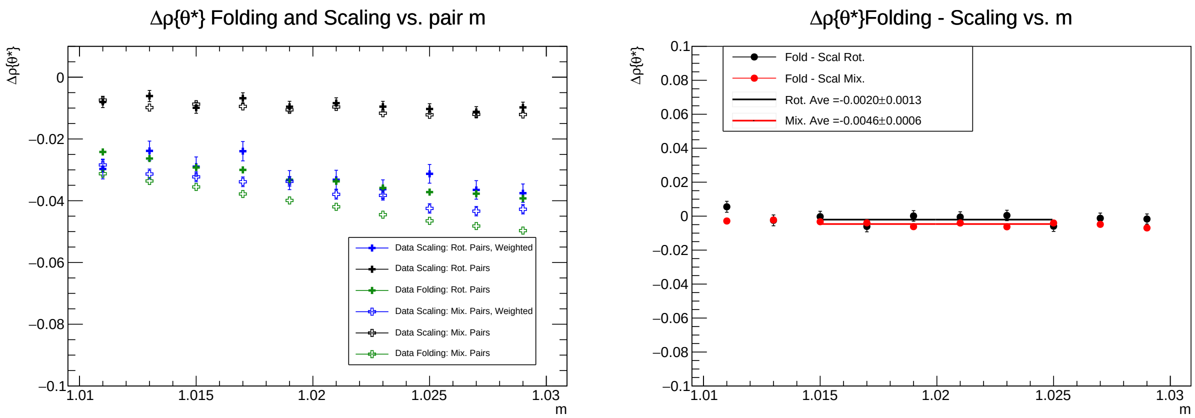

Figure A.9. Corrections from Folding minus Scaling in the ϕ-meson mass window for 19.6 GeV

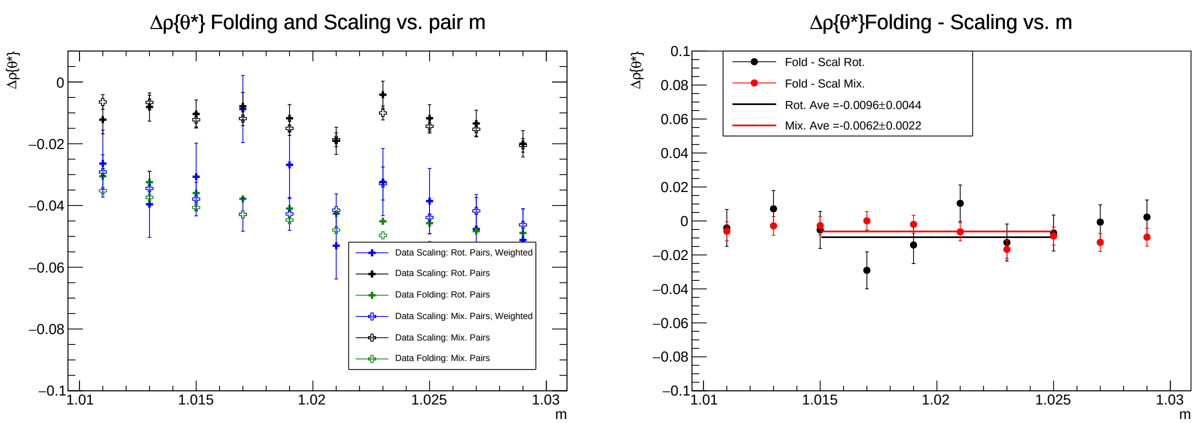

Figure A.10. Corrections from Folding minus Scaling in the ϕ-meson mass window for 11.5 GeV

B. DATA PARAMETERIZATIONS

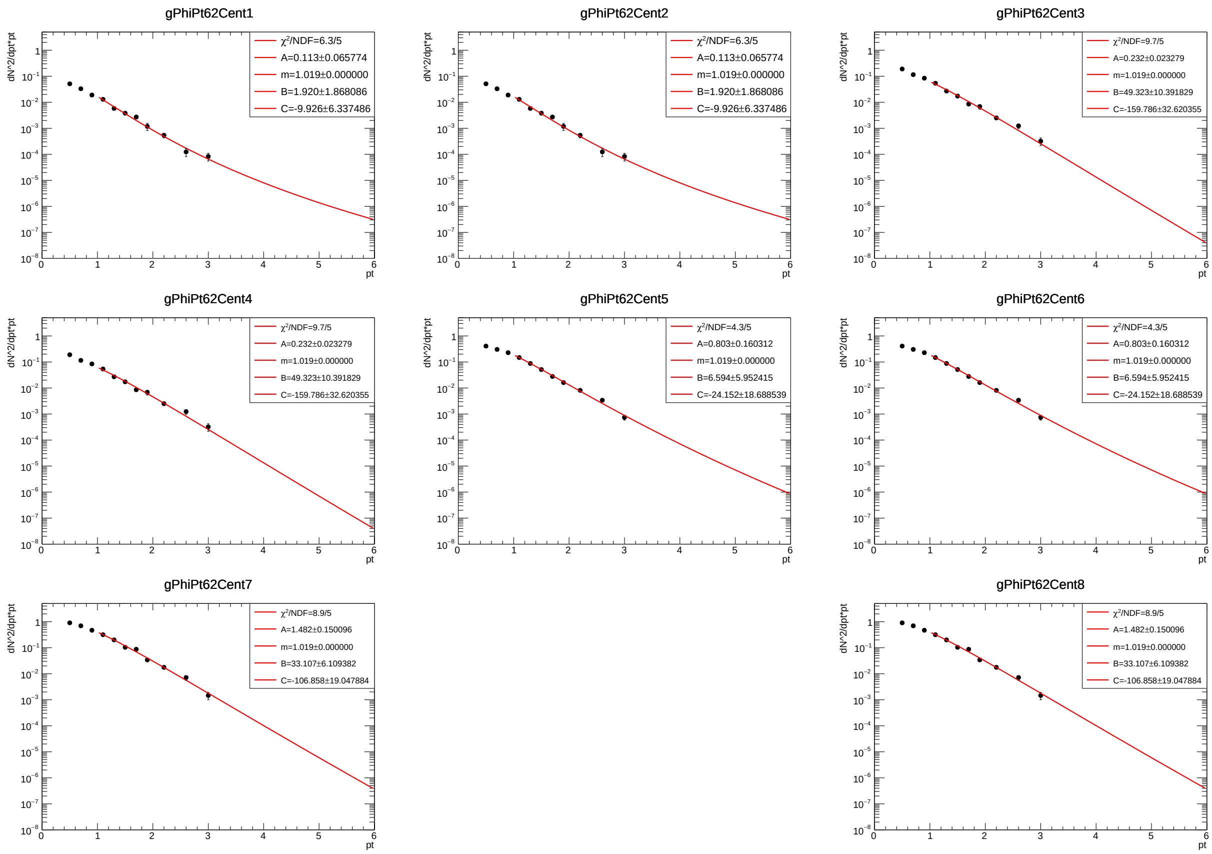

Figure B.1. Fits of published ϕ-meson $p_\perp$ spectra using Eq. 4.7 in each centrality of Au+Au collisions at 62 GeV.

Table B.1. The ϕ-meson multiplicity in each centrality in 200 GeV Au+Au collisions used in Data Folding in Sect. 4.2.1.

Centrality	0-5%	0-10%	10-20%	20-30%	30-40%	40-50%	50-60%	60-70%	70-80%
dN/dy	7.95	7.42	5.37	3.47	2.29	1.44	0.82	0.45	0.20

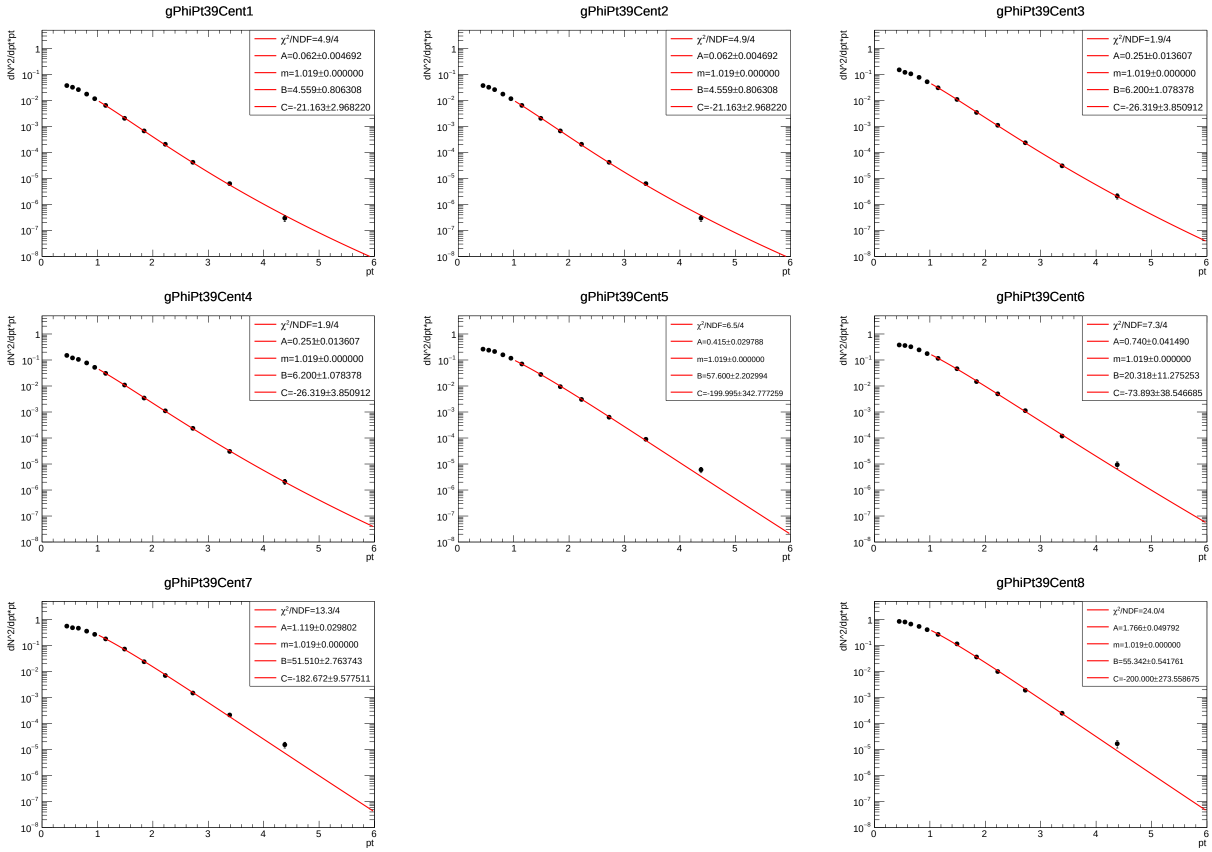

Figure B.2. Fits of published ϕ-meson $p_{\perp}$ spectra using Eq. 4.7 in each centrality of Au+Au collisions at 39 GeV.

Table B.2. The ϕ-meson $p_{\perp}$ spectra fit parameters by Eq. 4.7 in 200 GeV Au+Au collisions.

Centrality	70-80	60-70	50-60	40-50	30-40	20-30	10-20	05-10
a	0.066	0.172	0.245	0.461	0.670	1.109	1.673	2.174
c	5.011	4.365	5.972	8.717	67.105	9.920	45.236	39.220
d	−17.742	−15.484	−18.704	−26.908	−179.463	−28.802	−124.652	−109.559

Table B.3. The ϕ-meson $p_{\perp}$ spectra fit parameters by Eq. 4.7 in 62.4 GeV Au+Au collisions.

Centrality	70-80	60-70	50-60	40-50	30-40	20-30	10-20	05-10
a	0.113	0.113	0.232	0.232	0.803	0.803	1.482	1.482
c	1.920	1.920	49.323	49.323	6.594	6.594	33.107	33.107
d	−9.926	−9.926	−159.786	−159.786	−24.152	−24.152	−106.858	−106.858

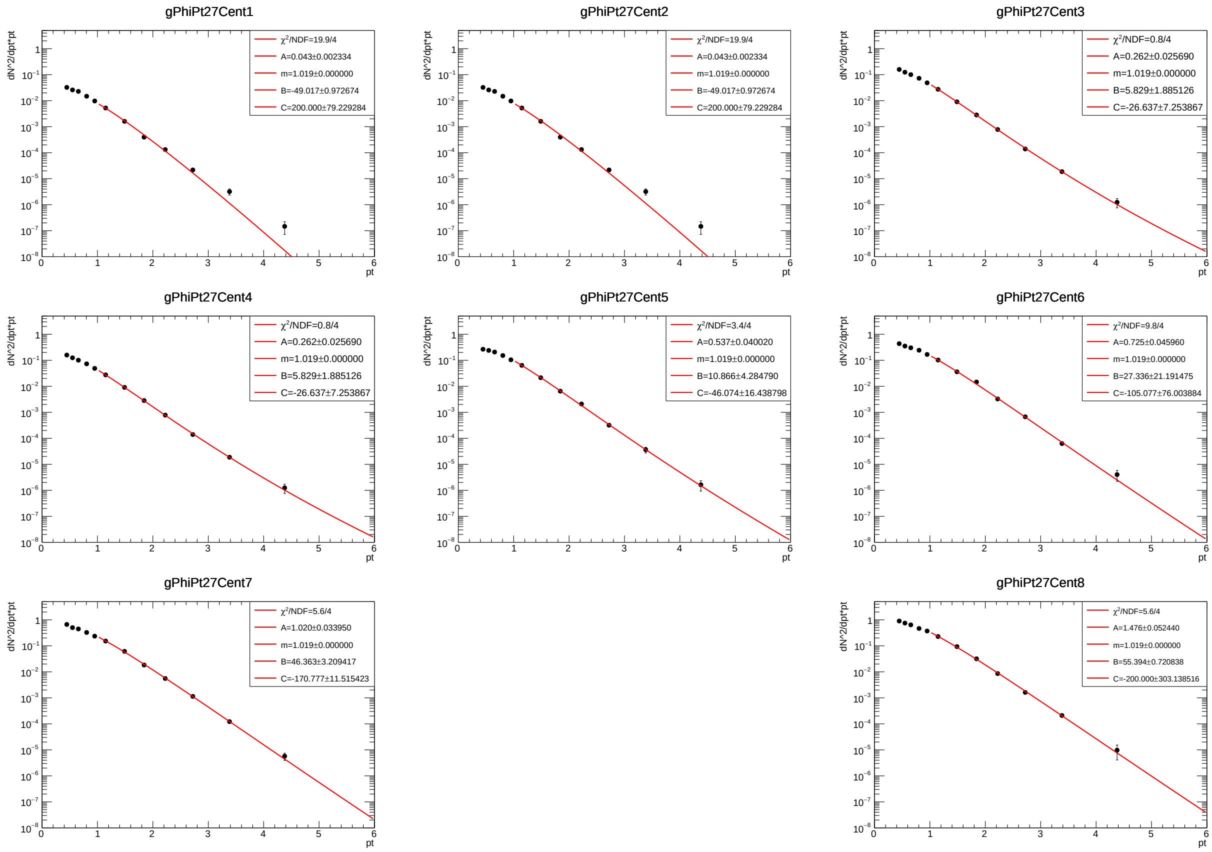

Figure B.3. Fits of published ϕ-meson $p_\perp$ spectra using Eq. 4.7 in each centrality of Au+Au collisions at 27 GeV.

Table B.4. The ϕ-meson $p_\perp$ spectra fit parameters by Eq. 4.7 in 39 GeV Au+Au collisions.

Centrality	70-80	60-70	50-60	40-50	30-40	20-30	10-20	05-10
a	0.062	0.062	0.251	0.251	0.415	0.740	1.119	1.766
c	4.559	4.559	6.200	6.200	57.600	20.318	51.510	55.342
d	−21.163	−21.163	−26.319	−26.319	−199.995	−73.893	−182.672	−200.000

Table B.5. The ϕ-meson $p_\perp$ spectra fit parameters by Eq. 4.7 in 27 GeV Au+Au collisions.

Centrality	70-80	60-70	50-60	40-50	30-40	20-30	10-20	05-10
a	0.043	0.043	0.262	0.262	0.537	0.725	1.020	1.476
c	−49.017	−49.017	5.829	5.829	10.866	27.336	46.363	55.394
d	200.000	200.000	−26.637	−26.637	−46.074	−105.077	−170.777	−200.000

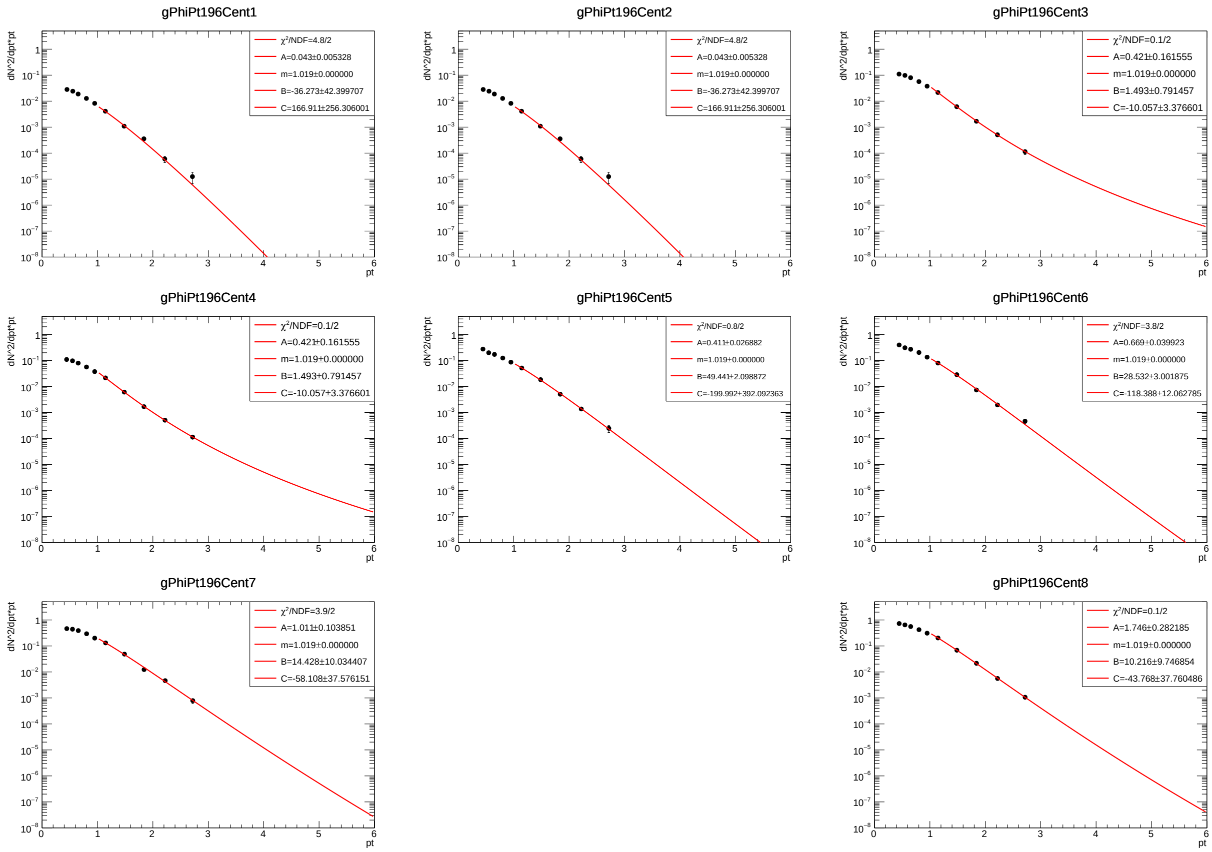

Figure B.4. Fits of published ϕ-meson $p_\perp$ spectra using Eq. 4.7 in each centrality of Au+Au collisions at 19.6 GeV.

Table B.6. The ϕ-meson $p_\perp$ spectra fit parameters by Eq. 4.7 in 19.6 GeV Au+Au collisions.

Centrality	70-80	60-70	50-60	40-50	30-40	20-30	10-20	05-10
a	0.043	0.043	0.421	0.421	0.411	0.669	1.011	1.746
c	-36.273	-36.273	1.493	1.493	49.441	28.532	14.428	10.216
d	166.911	166.911	-10.057	-10.057	-199.992	-118.388	-58.108	-43.768

Table B.7. The ϕ-meson $p_\perp$ spectra fit parameters by Eq. 4.7 in 11.5 GeV Au+Au collisions.

Centrality	70-80	60-70	50-60	40-50	30-40	20-30	10-20	05-10
a	0.043	0.043	0.421	0.421	0.411	0.669	1.011	1.746
c	-36.273	-36.273	1.493	1.493	49.441	28.532	14.428	10.216
d	166.911	166.911	-10.057	-10.057	-199.992	-118.388	-58.108	-43.768

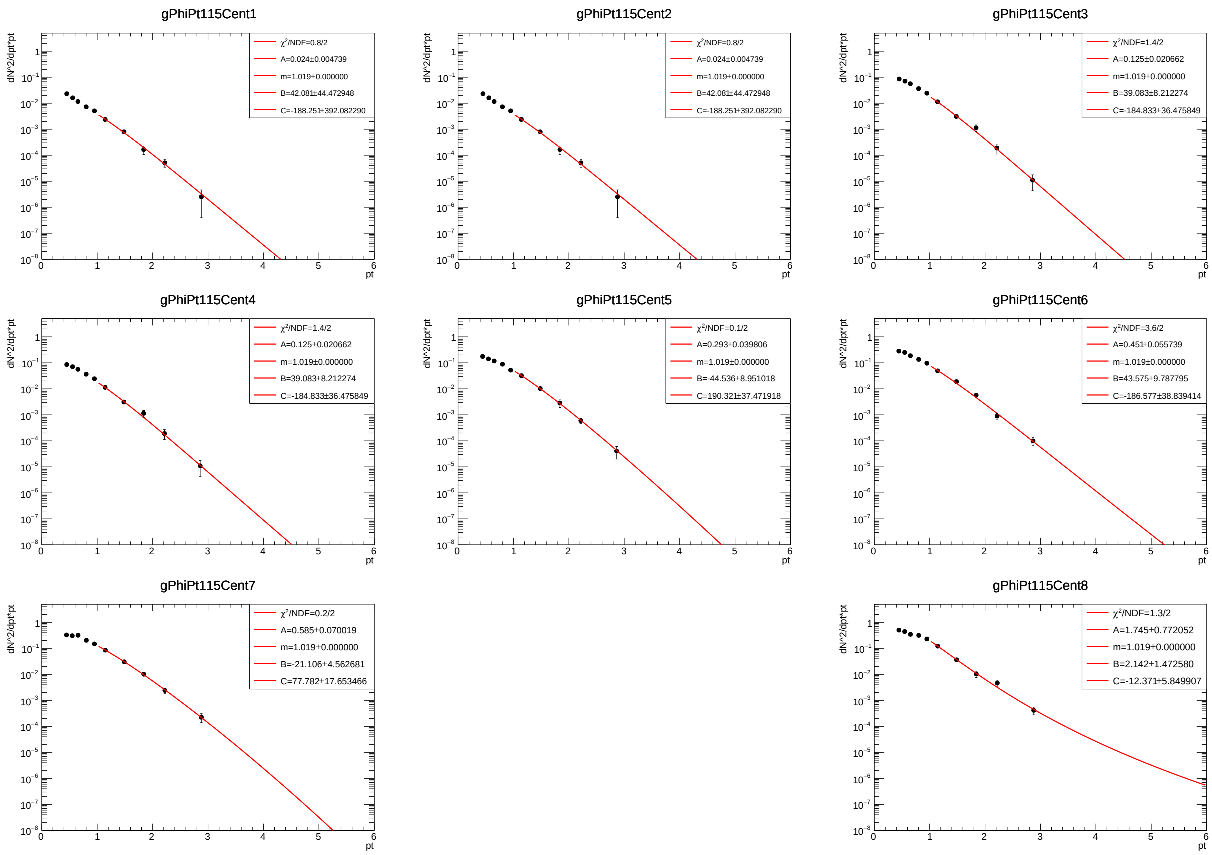

Figure B.5. Fits of published ϕ-meson $p_\perp$ spectra using Eq. 4.7 in each centrality of Au+Au collisions at 11.5 GeV.

Table B.8. Details of ϕ-meson $p_\perp$ spectra measurements and how the ϕ-meson $v_2(p_\perp)$ are parameterized in Au+Au collisions at 62.4 GeV, used in our Data Folding procedure. Here, "scaled Hadron" always means Hadron $v_2(\text{cent}, p_\perp)$ at 200 GeV scaled to that of ϕ-meson at a given energy.

StRefMultCorr Centrality in DATA	ϕ-meson $p_\perp$ spectra in data folding	ϕ-meson v_2 in data folding
00-05%	empty %	scaled Hadron 00-05 % to Pub. 00-80% ϕ
05-10%	00-20 %	scaled Hadron 05-10 % to Pub. 00-80% ϕ
10-20%	00-20 %	scaled Hadron 10-20 % to Pub. 00-80% ϕ
20-30%	20-40 %	scaled Hadron 20-30 % to Pub. 00-80% ϕ
30-40%	20-40 %	scaled Hadron 30-40 % to Pub. 00-80% ϕ
40-50%	40-60 %	scaled Hadron 40-50 % to Pub. 00-80% ϕ
50-60%	40-60 %	scaled Hadron 50-60 % to Pub. 00-80% ϕ
60-70%	60-80 %	scaled Hadron 60-70 % to Pub. 00-80% ϕ
70-80%	60-80 %	scaled Hadron 70-80 % to Pub. 00-80% ϕ

Table B.9. Details of ϕ-meson $p_\perp$ spectra measurements and how the ϕ-meson $v_2(p_\perp)$ are parameterized in Au+Au collisions at 39, 19.6, and 11.5 GeV, used in our Data Folding procedure. Here, "scaled Hadron" always means Hadron $v_2(\text{cent}, p_\perp)$ at 200 GeV scaled to that of ϕ-meson at a given energy.

StRefMultCorr Centrality in DATA	ϕ-meson $p_\perp$ spectra in data folding	ϕ-meson v_2 in data folding
00-05%	empty %	scaled Hadron 00-05 % to Pub. 00-80% ϕ
05-10%	0-10 %	scaled Hadron 05-10 % to Pub. 00-80% ϕ
10-20%	same %	scaled Hadron 10-20 % to Pub. 00-80% ϕ
20-30%	same %	scaled Hadron 20-30 % to Pub. 00-80% ϕ
30-40%	same %	scaled Hadron 30-40 % to Pub. 00-80% ϕ
40-50%	40-60 %	scaled Hadron 40-50 % to Pub. 00-80% ϕ
50-60%	40-60 %	scaled Hadron 50-60 % to Pub. 00-80% ϕ
60-70%	60-80 %	scaled Hadron 60-70 % to Pub. 00-80% ϕ
70-80%	60-80 %	scaled Hadron 70-80 % to Pub. 00-80% ϕ

C. DETAILED ANALYSIS PLOTS

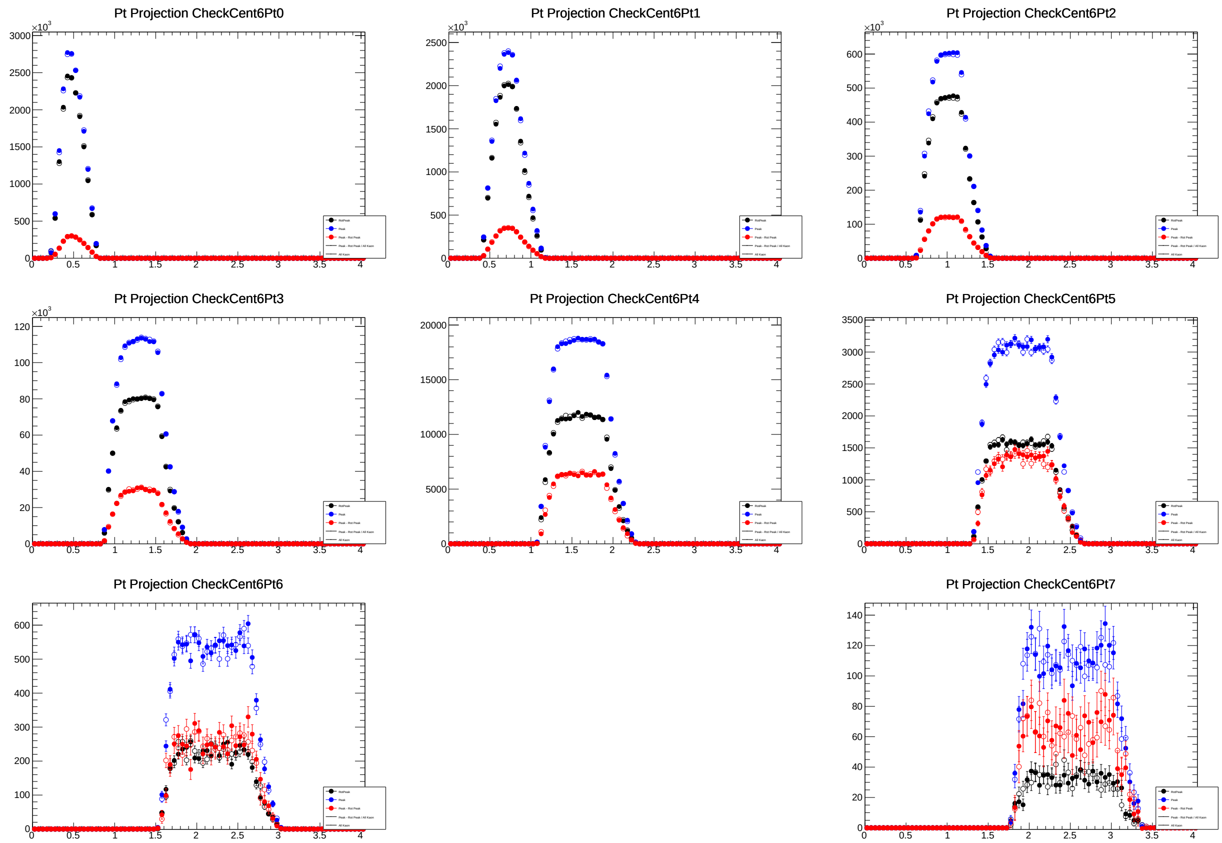

Figure C.1. The $p_\perp$ projections of single Kaon 3D histograms for Peak (blue), Rot. Peak (black) and Peak − Rot. Peak (red) in centrality 20-30% Au+Au collisions (Run-14) in each pair $p_{\perp,\mathrm{pair}}$ bin. Overall y-axis scale is not meaningful, as this is not used to do an efficiency style correction of the ϕ-meson yields, but a correction number to be added to the raw spin alignment signal.

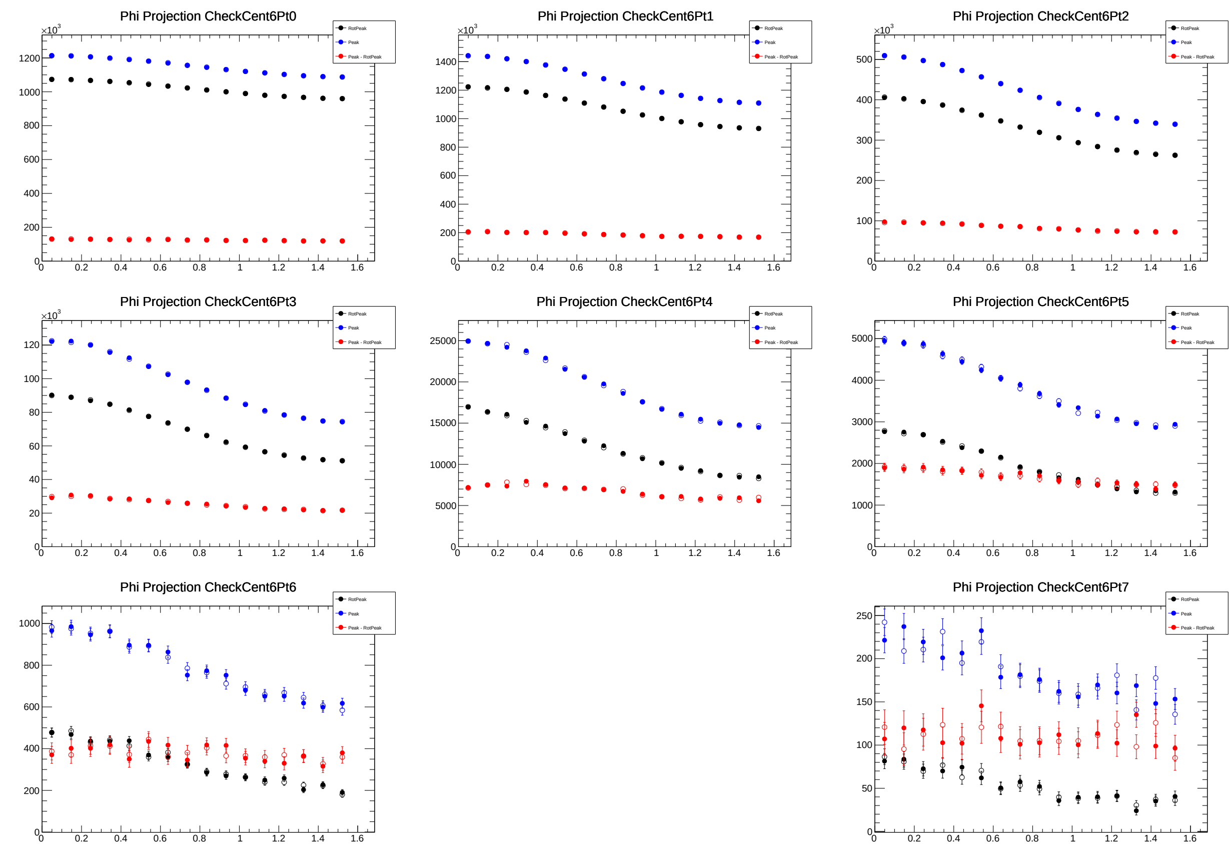

Figure C.2. The $\phi - \psi_2$ projections of single Kaon 3D histograms for Peak (blue), Rot. Peak (black) and Peak − Rot. Peak (red) in centrality 20-30% Au+Au collisions (Run-14) in each pair $p_{\perp,\mathrm{pair}}$ bin. Overall y-axis scale is not meaningful, as this is not used to do an efficiency style correction of the ϕ-meson yields, but a correction number to be added to the raw spin alignment signal.

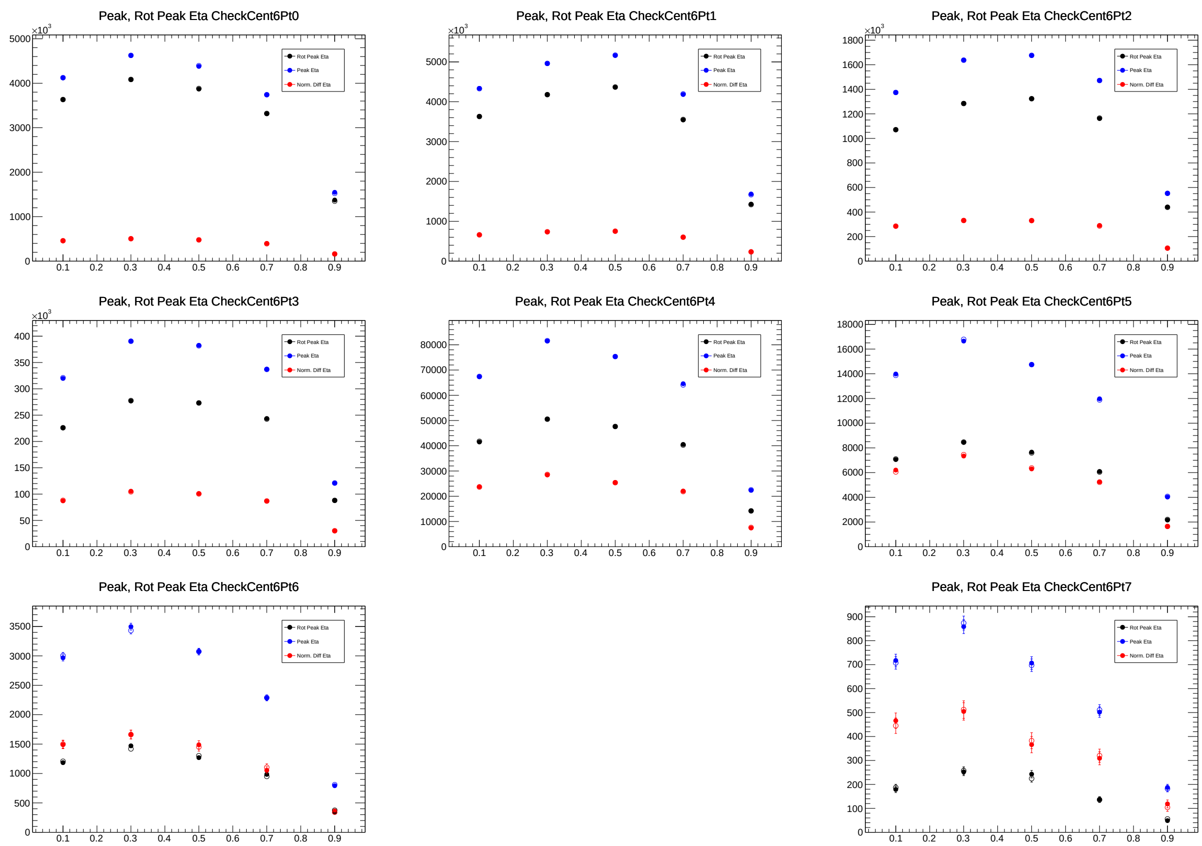

Figure C.3. The $|\eta|$ projections of Single Kaon 3D histograms for Peak (blue), Rot. Peak (black) and Peak $-$ Rot. Peak (red) in centrality 20-30% Au+Au collisions (Run-14) in each pair $p_{\perp,\text{pair}}$ bin. Overall y-axis scale is not meaningful, as this is not used to do an efficiency style correction of the ϕ-meson yields, but a correction number to be added to the raw spin alignment signal.

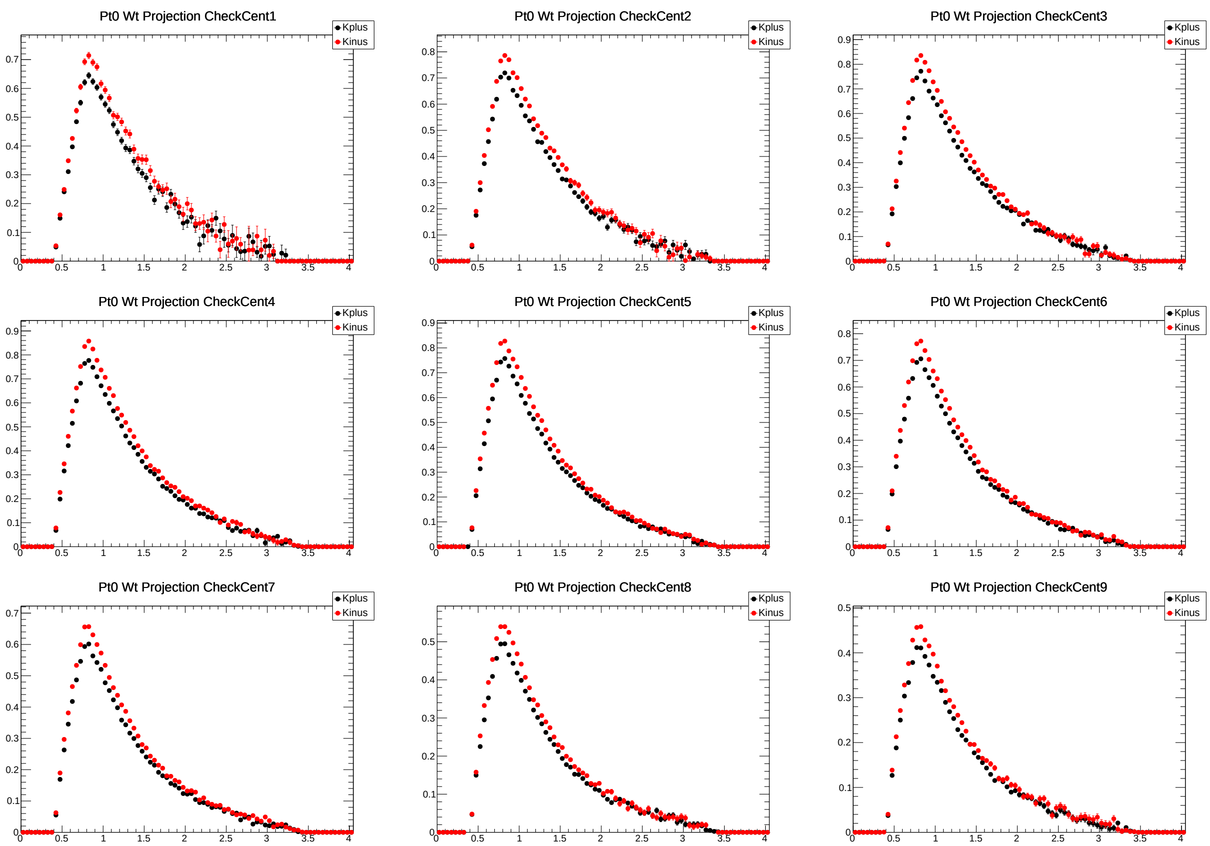

Figure C.4. Example of $p_\perp$ projection of 3D histograms of $\sum_{p_{\perp,\text{pair}}\text{bins}}$ (Peak − Rot. Peak) divided by all Kaons in each centrality bin.These histograms are the $p_\perp$ projections of the weight histograms. Overall y-axis scale is not meaningful, as this is not used to do an efficiency style correction of the ϕ-meson yields, but a correction number to be added to the raw spin alignment signal.

VITA

BASIC INFORMATION

Name: C.W. Robertson

Email: rober558@purdue.edu

EDUCATION

Purdue University *June 2019 - Present*

Location: 610 Purdue Mall, West Lafayette, IN, 47907, United States

Department: Department of Physics and Astronomy

Degree: PhD degree in Physics, **estimated in May 2025**

University of Kansas August 2015 - May 2019

Location: 1450 Jayhawk Blvd, Lawrence, KS 66045

Department: Physics Department

Degree: Bachelor of Science in Physics, May 2019

Degree: Bachelor of Science in Astronomy, May 2019

EXPERIENCE

Purdue University *June 2019 - Fall 2021*

Position Title: Teaching Assistant

Purdue University *Fall 2021 - Present*

Position Title: Research Assistant

Supervisor: Prof. Fuqiang Wang

STAR Collaboration Fall 2021, May 2023, March 2025

Location: Brookhaven National Laboratory

Position Title: STAR Detector Operator

Description: STAR Detector Operator shifts

IceCube Collaboration Summer 2018

Location: University of Wisconsin-Madison

Position Title: Undergraduate Research Assistant

Description: Detector effect unfolding

RESEARCH INTEREST

High Energy Particle/Nuclear Physics

I am interested in the high energy nuclear physics, and working on the data analysis for STAR (Soleniodal Tracker At Relativistic Heavy Ion Collider), the Large Hadron Collider (LHC), or neutrino experiments such as the Deep Underground Neutrino Experiment (DUNE).

My interests include ϕ-meson spin alignment, quantum tomography and other times of quantum information science at particle colliders, searches for beyond the standard model physics.

AWARD

Ross Graduate Teaching Assistant Fellowship *June 2019*

From: Department of Physics and Astronomy, Purdue University